

DISSERTATION

DEVELOPMENT OF MOBILE OPEN-PATH CAVITY RING-DOWN SPECTROMETER
FOR MEASUREMENT OF TRACE ATMOSPHERIC METHANE GAS

Submitted by

Laura McHale

Department of Mechanical Engineering

In partial fulfilment of the requirements

For the Degree of Doctor of Philosophy

Colorado State University

Fort Collins, Colorado

Spring 2018

Doctoral Committee:

Advisor: Azer P. Yalin

Anthony Marchese

Daniel Olsen

Jeffrey Pierce

Copyright by Laura McHale 2018

All Rights Reserved

ABSTRACT

DEVELOPMENT OF MOBILE OPEN-PATH CAVITY RING-DOWN SPECTROMETER FOR MEASUREMENT OF TRACE ATMOSPHERIC METHANE GAS

Use in recent decades of methane as a ‘clean’ alternative to coal and gasoline has seen a rapid increase in natural gas extraction in the United States. Although combustion of methane produces less CO₂ than traditional fuels, it is a powerful greenhouse gas with a 20 year Global Warming Potential (GWP20) that is 84x that reported for CO₂ in the latest IPCC report; therefore, the promise of natural gas as a clean fuel can only be realized if emissions of uncombusted gas are sufficiently low. To address this problem, there is a need for both regional (basin wide) measurements of methane emissions to determine global levels, as well as localized measurements to allow identification and reduction of emissions (“leaks”) from specific equipment. The goal of this research is to develop a mobile open-path cavity ring-down spectroscopy (CRDS) sensor for localized measurements of atmospheric methane. While designed with the oil and gas industry in mind, the technology also has application to study emissions from agricultural operations and those from other sectors.

This thesis presents development from proof-of-concept open-path sensor through two mobile iterations. CRDS can provide fast, non-intrusive, sensitive measurements; but in contrast to available instruments, the focus is on open-path operation (no flow-cell and pump) to provide opportunities for significant weight, size and power reductions to increase the mobility of the technique (<4 kg, <25 W). Challenges of open-path operation, such as fitting broadened spectral peaks, preserving mirror cleanliness and techniques for removing signal noise due to aerosol particles are addressed. The sensor is based on widely available and mature engineering near-

infrared (NIR) opto-electronic components that have been developed for the telecom industry. Sensor validation with known methane concentrations show that the open-path sensor is capable of measuring atmospheric concentrations in the range of ~1.8-20+ ppmv at a rate of 1-3 Hz. Sensitivity studies using Allan variance techniques show sensitivity of < 20 ppbv in 1 – adequate for practical leak detection of small plumes <1 ppmv. Comparisons against a commercially available closed path sensor in mobile deployments are presented, along with mobile measurements from natural gas facilities in Platteville, CO and Washington County, PA. Finally, integration of the sensor onto a UAS platform for airborne measurements of methane and ammonia from agricultural applications is discussed.

ACKNOWLEDGMENTS

I first want to say thank you to Dr. Azer Yalin for accepting me into his research group at Colorado State University. I first met Dr. Yalin in 2007 when he accepted my invitation to join my Masters committee while a student of the Atmospheric Science Department. At the time, I was planning on using a CRDS sensor someone else built for analysis of data from a biomass burning study and Dr. Yalin was the obvious choice. When I decided to return to graduate school for my PhD, I thought that the best way to understand the measurements I was using for environmental research was to develop the sensors myself and I decided to switch departments to Mechanical Engineering where Dr. Yalin welcomed me. While a part of his group I obtained the skills and knowledge I was looking for, working on interesting and innovative projects for which I am very grateful.

I would like to say thank you to my committee members, Dr. Anthony Marchese, Dr. Daniel Olsen and Dr. Jeffrey Pierce who have supported me during my doctoral degree and helped provide feedback from a different point of view. I also appreciate the help and assistance I have had from all of my professors here at CSU during my entire graduate career. Although I switched departments between my masters and doctoral programs, I would not be the person I am without my experience in the Atmospheric Science department with my former advisor Dr. Sonia Kreidenweis.

I would not have been able to complete my work without an incredible amount of support from both within the lab and from outside, professional help. A significant part of this work related to the miniaturization of the sensor for mobile use and this would not have been possible without professional help in the mechanical, electronic and software design. Charles Rose, although a student member of our group at the time, provided what I consider to be professional

design and construction for Phase-II. Czero was incredibly professional to work with, but were also friendly, welcoming and helpful to me as a student on this project. Tom Miller, TCB Engineers, worked with us from late stages of Phase-I continuing to this day. Tom also not only provided the technical aspect of the electronics and software that were necessary to advance the sensors but was also always willing to take the time with me as a student to listen to my concerns, questions and own ideas on how the electronics or software could improve. Through this project he has not only become someone I would come to for technical advice but has also become a friend. I also want to say thank you to the UAS team, Charles Rose, Meghan Reimann, Collin VanTilburg, Jared Ham and Dr. Frederick Smith for their hard work over the past year on the UAS system and their continued patience and support as we work towards whole system integration. I am grateful for the assistance from my colleagues in the Atmospheric Science department at CSU, Arsineh Hecobian, Kira Shonkwiler and Landon Macdonald for not only loaning me the Picarro sensor but also assisting in with some of our preliminary methane release studies. Finally, I would like to say thank you to Xiaochi Zhou, from John Albertson's group at Cornell University, for his analysis of leak rate quantification for METEC and for letting me participate in the study in Washington County PA.

Graduate school would not have been possible without the technical and personal support of my colleagues over the years in the Center for Laser Sensing and Diagnostics: Soran Shadman, Adam Friss, Ciprian Dumitrache, Charles Rose, Betsy Farris, Ben Martinez, Simon Gassner, Sean Walsh, Jordan Rath. They provided invaluable help in the lab when I was just learning my way around the lab, supported me during the middle tough bits and helped make finishing possible.

I want to thank my family for their support over 20+ years of education, including a stubborn return to school to get my PhD slightly later in life. Finally, I want to say a huge thank you to my husband, Graeme, who from the moment I met him thought I should complete my quest for a PhD. He has helped me learn that I am capable of accomplishing far more than I thought I could with patience, hard work and determination.

TABLE OF CONTENTS

ABSTRACT	ii
ACKNOWLEDGMENTS	iv
LIST OF FIGURES	x
CHAPTER 1: Introduction	1
1.1 Objective	1
1.1.1 Fugitive Emissions from Oil and Gas	2
1.2 Literature Review	3
1.2.2 Methane CRDS sensors	3
1.2.3 Oil and Gas Monitoring	5
1.3 Dissertation Outline	7
CHAPTER 2: Spectroscopy	9
2.1 Introduction	9
2.2 Absorption	10
2.3 Methane Absorption	13
2.4 Measurement Techniques	14
CHAPTER 3: Cavity Ring-down Spectroscopy	17
3.1 Theory	17
3.2 Open-path CRDS	20
3.3 Development of an open-path Methane CRDS sensor	22

CHAPTER 4: Development and Design of Open-Path Sensor	27
4.1 Optics	28
4.2 Data Acquisition and Analysis.....	32
4.3 Electronics.....	35
4.4 Hardware.....	37
CHAPTER 5: Laboratory Results.....	40
5.1 Mirror Purge.....	40
5.2 Aerosol Noise in Signal	41
5.3 Numerical filters to remove aerosol signals.....	42
5.4 Sensor Accuracy	45
5.5 Sensitivity	46
5.6 Indoor Picarro comparison.....	49
CHAPTER 6: Mobile Measurements	51
6.1 Platteville, CO.....	51
6.2 METEC.....	55
6.3 Marcellus Basin, PA	67
6.4 UAS integration and flight.....	75
CHAPTER 7: Conclusions	78
7.1 Summary.....	78
7.2 Future Work	83

7.2.1 Methane Field Studies.....	83
7.2.2 Environmental Studies.....	84
7.2.3 Sensor Improvements.....	85
BIBLIOGRAPHY.....	87

LIST OF FIGURES

1.1:	Location of oil and gas wells in Colorado (Colorado Oil and Gas Commission, 2016).....	2
2.1:	The Electromagnetic spectrum.....	10
2.2:	Simulated Normalized Doppler, Collisional broadening and Voigt convolution for methane absorption at 1651 nm for P=0.1 atm and T=296 K.....	13
2.3:	Simulated methane absorption for typical atmospheric conditions, T=296 K P=0.84 atm and [CH ₄]=1.8 ppmv	14
3.1:	Simulated absorption in the NIR for typical atmospheric conditions, T=296K, P=0.84atm, [CH ₄]=1.8ppmv. H ₂ O=0.013 and [CO ₂]=460 ppmv.....	22
3.2	Simulation of region measured by open-path sensor at 1.7 um for typical atmospheric conditions, T=296 K, P=0.84 atm, [CH ₄]=1.8 ppmv, [H ₂ O]=50% RH, [HCl]=0.5 ppbv. Left: Zoomed in look at region scanned by laser and 4 methane peaks included in synthetic spectrum and the region scanned by the laser.....	23
3.3	Simulation of region measured by open-path sensor at 1.651 um for typical atmospheric conditions, T=296 K, P=0.84 atm, [CH ₄]=1.8 ppmv, [H ₂ O]=50% RH, [CO ₂]=380 ppbv. Dashed lines show the four methane peaks used in the synthetic spectrum and the region scanned by the laser.....	25
4.1:	Optical layout of the sensor, Phase-I using a 1742 nm laser.....	27
4.2:	Optical layout of the sensor, Phase-II using a 1651 nm laser with changes to the location of the isolator, HRM and Data Acquisition system and some reduction in the overall footprint.....	28
4.3:	Optical layout of sensor Phase-III where the optical isolator and AOM have been moved in line with the fiber optic and the overall footprint has decreased.	28

4.4:	Optical isolator comprised of a polarizer and quarter wave-plate.....	30
4.5:	Diffraction of beam in AOM occurs when incoming beam, I , enters the crystal at the Bragg angle, θ_B . The diffracted beam, I_I , will exit the crystal at the same angle, θ_B . I_I is aligned through the optical cavity, when no RF signal is supplied the beam I_0 leaving the AOM will not enter the optical cavity.....	31
4.6:	Graphical representation of signal inputs (green – detector) and outputs (blue – laser scan signal, red – ATOM TTL) of the sensor. Figure 4.6(a) shows multiple cavity resonances while the laser is being scanned while Figure 4.6(b) is zoomed in on an individual ring down event.	33
4.7:	Sensor Phase-I mounted in bed of pickup truck for preliminary mobile tests.	37
4.8:	Left: Model of Phase-II optical head, dimensions 39” x 7”x4.7” and weight 5.3 kg. Right: Model of sensor electronics with steel base.	38
4.9:	Left: Model of Phase-III sensor head, dimensions and weight 2 kg. Right: Electronics enclosure, dimensions and weight.....	39
5.1:	Histogram of CRDS absorption measurements for closed-cell measurement of zero air with no particles and open-path measurement of ambient laboratory air. Arrow indicates range of points within 50%, $\pm 0.7 \times 10^{-8} \text{ cm}^{-1}$ filter.	41
5.2:	Methane absorption spectrum of ambient laboratory air measured by the open-path 1742nm CRDS. Raw data shown with red points, data preserved by filter shown with black points, final spectral fit shown with cyan curve. Inset in Figure 5.2(a) is more zoomed out to show larger fluctuations. Application of frequency bin filter shown in Figure 5.2(a), global iterative filter in Figure 5.2(b). The first iterative fit is shown with the dashed cyan curve. Intermediate fits not shown.....	44

5.3:	Methane concentrations recorded in closed-path configuration.....	46
5.4:	Allan variance of absorption values for closed-path (zero- air), open-path ambient air, and open-path ambient air with software filter.	47
5.5:	Allan variance for 1651 nm Phase-II sensor for simulated concentration, zero air, closed path cylinder air, closed path room and and open path room air data.....	48
5.6:	Allan Variance study for Phase-III sensor in CSU laboratory, deviation of 9.6 ppbv found for 1 s average.	49
5.7:	Experiment setup for methane comparison (a) between open-path instrument and commercial closed-path instrument (Picarro, G2203). Results of comparison measurements shown in (b), averaged to 5-seconds.	50
6.1:	Map showing oil & gas well density for northern Colorado,.....	51
6.2:	1651 nm open-path CRDS sensor (Phase-II) mounted to roof of Ford Expedition in Platteville, CO January 2017. Figure 6.2(a): Open-path sensor placement on roof of vehicle. Figure 6.2(b): Multiport inlet for Picarro along cavity of open-path CRDS sensor.	52
6.3:	Open-path CRDS data from 1/10/17 driving from Fort Collins to Platteville, CO. Figure 6.3(a): Timeline of open-path (black) and Picarro (red) data. Figure 6.3(b): Parameters used to filter open-path data, Top: Ingestion Rate ($>175 \tau/s$), Bottom: R^2 of spectral fit (>0.9).....	53
6.4:	1-1 comparison of open-path and Picarro data after open-path data was filtered, giving slope = 0.89, $R^2 = 0.95$ and SSE = 3.4.	53

6.5: 1-1 Comparison of open-path and Picarro data for Platteville, CO on 1/12/17. Colder temperatures and higher concentrations led to worse comparison (slope = 0.8, $R^2 = 0.85$, SSE = 23.46)..... 54

6.6: Open-path CRDS data measured on 1/10/17 (blue) and 1/12/17 (purple) of the same facility in Platteville, CO, maximum concentration $[CH_4]=6.2$ ppmv..... 55

6.7: Aerial view of the METEC site with an x indicating the location of the leak release during sensor tests. The site is controlled through a trailer located on the east side of the site (bottom of the photo)..... 56

6.8: Top: Time series of 1 Hz methane concentration measured for a leak rate of 78.76 scfh. Bottom: Composite graph of all loops showing the elevated concentration (both color and height indicate methane concentration. Star in the bottom right indicates the location of the leak and the green arrow indicates the direction and magnitude of local wind..... 58

6.9: Top: Time series of 3Hz methane concentration measured for a leak rate of 78.76 scfh. Bottom: Composite graph of all loops showing the elevated concentration (both color and height indicate methane concentration. Star in the bottom right indicates the location of the leak and the green arrow indicates the average direction and magnitude of local wind. 59

6.10: Integrated plume measurements for 8/30/17 at METEC for 6 flow rates, comparing 1 Hz and 3 HZ analysis. 60

6.11: Integrated plume measurements for 8/30/17 separated out by flow rate and loop around leak site..... 60

6.12: Concentration vs distance traveled for 1 Hz (top) and 3 Hz (bottom) for one pass at 96.25 scfh flow rate. 61

6.13: Spectra from 1 Hz data for maximum concentration in Figure 6.12. Black points indicate those kept by the aerosol filter, red are rejected points. The cyan curve indicates the fit to the data. 62

6.14: Top: Time series of 3 Hz and Picarro methane concentration measured for a leak rate of 30 scfh. Bottom: Composite graph of all loops showing the elevated concentration (both color and height indicate methane concentration. Star in the bottom right indicates the location of the leak and the green arrow indicates the average direction and magnitude of local wind. 3 Hz open-path data is shown on the left, Picarro on the right..... 64

6.15: Top: Time series of 3 Hz and Picarro methane concentration measured for a leak rate of 65 scfh. Bottom: Composite graph of all loops showing the elevated concentration (both color and height indicate methane concentration. Star in the bottom right indicates the location of the leak and the green arrow indicates the average direction and magnitude of local wind. 3 Hz open-path data is shown on the left, Picarro on the right..... 64

6.16: 1-1 Comparison of Picarro and Open-path for testing at METEC on 9/25/17 with slope = 0.88 and $R^2 = 0.73$ 65

6.17: Integrated plume measurements for 9/25/17 at METEC for 2 flow rates, comparing open-path 1 Hz and 3 HZ analysis. 66

6.18: Integrated plume measurements for 9/25/17 at METEC for 2 flow rates, comparing open-path and Picarro data. 66

6.19: Concentration traces for the large pass of the 65 scfh leak release for 1 and 3 Hz open-path data and Picarro. 67

6.20: Map showing location of oil and gas wells in Pennsylvania, Washington County is located in the south-west corner of the state. 68

6.21: Phase-III sensor mounted on vehicle for study in Marcellus County, PA, October 2017. 70

6.22: Traces of methane (CH₄) gas and VOC (PI) emissions detected using a PID on 10/27/17 in Marcellus County, PA. This work was presented in a poster at AGU in New Orleans, LA 2017 by Dr. Xiaochi Zho..... 70

6.23: Leak rate analysis for data collected on 10/27/17 in Marcellus County, PA. This work was presented in a poster at AGU in New Orleans, LA 2017 by Dr. Xiaochi Zho..... 71

6.24: (Top) Methane data imposed on Google Earth image, collected on 10/30/17 near Arden Landfill. (Bottom) Time series of methane concentration. 72

6.25: (Top) Methane data imposed on Google Earth image, collected on 10/30/17 near an oil and gas site next to what appear to be a dairy. Image was rotated slightly to better visualize the plume. (Bottom) Time series of methane concentration. 73

6.26: (Top) Methane data imposed on Google Earth image, collected on 10/30/17. (Bottom) Time series of methane concentration..... 74

6.27: (Left): Pipe where potential leak was measured (< 3 ppmv) on 10/29/17. (Right): Valve box or pipes where potential leak (<12 ppmv) was measured on 10/31/17..... 75

6.28: (Left) Methane sensor mounted onto 12 ft Telemaster. (Right) Sensor electronics mounted in body of plane..... 77

CHAPTER 1:

Introduction

1.1 Objective

Methane is an important tropospheric gas and has many sources in the lower atmosphere, natural (freshwater, animals, wildfires, geologic, permafrost) and anthropogenic (animals, landfills and waste, biomass burning, fossil fuels). Methane has a relatively long tropospheric lifetime ~10 years¹, dominated by reactions with the hydroxyl radical OH, leading to relatively stable background concentrations. Methane concentrations have increased by ~150% since pre-industrial times to 1803.2 ppbv² primarily due to changes in anthropogenic sources which are estimated to contribute 50-65%³ of the total methane released. After several years of stable concentration since the 1990's, methane concentration has also shown an increase since ~2007. Additionally, as global temperatures rise, it is expected that an increase in methane will be seen from thawing permafrost.

Methane is important to study because of its effects in the troposphere. Methane is championed by many in its role as a 'clean' fuel, producing less CO₂ than coal or gasoline during combustion, but it is a significant greenhouse gas in its own right. The latest IPCC report² lists its 20 year Global Warming Potential (GWP₂₀) as 84x that CO₂. Methane is a precursor to ozone formation, along with VOC's, reducing the oxidizing abilities of the atmosphere through reactions with OH radical. As ozone is also a greenhouse gas, this shows how methane can have indirect effects as well as direct effects.

1.1.1 Fugitive Emissions from Oil and Gas

Natural gas has seen a recent rise in use and extraction, contributing to the increase in anthropogenic methane. The Colorado Oil and Gas conservation Commission (COGCC) estimates that there are currently 24,000 wells in Colorado, with 10,000 new wells since 2005 (Figure 1.1). Natural gas extraction constitutes a number of components from extraction, processing, transmission, storage and distribution and the EPA inventories estimate that about 1% of methane is lost to the atmosphere⁴. Recent work has also shown that a large percentage of methane released into the atmosphere is through so called ‘super emitters’⁵, leading to an underestimation of atmospheric methane. Previous attempts to reconcile estimates of atmospheric methane from top-down studies (i.e., from aircraft or models⁶⁻⁸) with bottom-up studies (i.e. from inventories or field sensors^{4,9,10}) have shown that more work is needed to properly account for methane leaks.

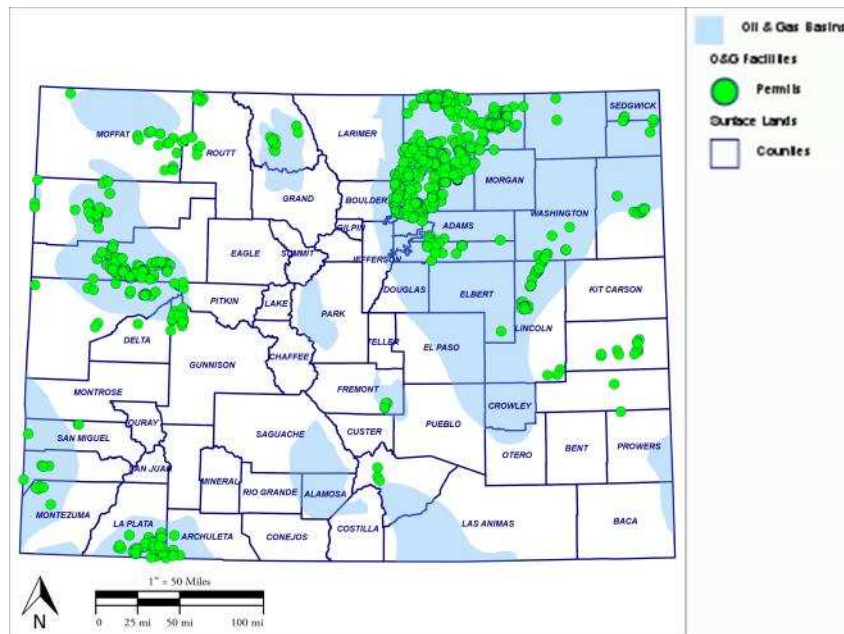


Figure 1.1: Location of oil and gas wells in Colorado (Colorado Oil and Gas Commission, 2016)

As discussed, many studies have been performed using road-based mobile sensors for quantification of methane emissions. Ground-based systems are useful, because power and weight are not a problem, relatively speaking. On the other hand, they can be expensive to setup, require human operators and are limited to where roads make measurements possible (and line of site due to lack of interference from trees/hills etc.). Aircraft based measurements so far have been limited to small manned planes that are capable of carrying a significant weight but are limited in measurement height above the ground, giving a more global average methane measurements rather than direct leak detection or emission rate quantification.

Un-manned aerial systems (UAS's) are a new area of interest for such measurements due to their ability to fly over difficult-to-reach terrain as well as an ability to measure vertically and horizontally. A difficulty with UAS's is the amount of available weight, and by proxy the power, available for any sensors that would be mounted. Some work has been done with camera systems mounted to UAS's¹¹ where the systems are flown over pipelines, looking for leaks. These systems can identify leak location but are unable to quantify emissions and have to be flown over an entire system to find them. If sensors capable of sensitive gas detection could be mounted to UAS's, the system could be flown upwind and downwind of facilities, used for leak quantification.

1.2 Literature Review

1.2.2 Methane CRDS sensors

The most well-known comparison sensors to ours are those constructed by Picarro which utilize a patented temperature and pressure controlled, closed-path 3 mirror optical cavity, measuring methane gas at 1651 nm^{12,13}. The Picarro sensors have been widely used in field studies of leak detection from oil and gas facilities^{8,14,15}. Sensors report 5ppbv in 30 seconds for

methane isotope sensors (in precision mode, G2132-i, G2201-i), or 0.5 ppbv in 5 seconds (G2301, G2401).

Stability and Allan variance results were shown for a closed path CRDS sensor¹⁶⁻¹⁸ which utilizes two continuous lasers, one tuned to the methane peak (1652nm) and one tuned off, to differentially determine concentration. When the system was isolated from mechanical vibrations a sensitivity of 0.19 pptv at 1 atm was found for an optimum averaging time of 13 min.

Fawcett¹⁹ demonstrated the use of a continuous wave laser near 1.65 μm for closed-path measurement of tropospheric methane using CRDS where the laser was locked to the cavity using a piezo-electric transducer. The lab based sensor had a detection limit of 33 ppbv at 0.1 torr for 100s average and the authors estimated that increased signal to noise in atmospheric pressure would yield a detection limit of 52 ppbv.

He^{20,21} used a fiber coupled swept cavity CRDS to deliver laser signals over fibers and through use of an optical switch, receive signals from the optical cavity in the same data processing center. Through use of such a system, several remote sensors could be deployed in a fiber optical network and be controlled by the same central unit. The unit operated at 1635.4 nm and reported a minimum detection limit of 65 ppbv. In this technique, the laser is modulated at a frequency faster than the resonance of the cavity, and the buildup of light from the cavity is measured when the laser scanned off of resonance.

Measuring methane isotopes rather than just methane concentration can help understand what the sources (agriculture, oil and gas) of the gas were. Recent work in India has been done monitoring the ratio of $^{12}\text{CH}_4$ and $^{13}\text{CH}_4$ in the air using a QCL at 7.5 μm in a continuous wave CRDS sensor. The closed-path lab-based sensor additionally modulated the cavity length to

achieve resonance between the laser and the cavity and extrapolated their absorption sensitivity measurements to atmospheric pressure to give 396 pptv and 287 pptv for each isotope at 0.13 atm.

1.2.3 Oil and Gas Monitoring

Extensive field studies have been performed to quantify emissions of methane from oil and gas facilities. Ground-based measurements typically fall in three categories: a.) Direct onsite measurement, b.) Tracer methods whereby a tracer gas is leaked at a known rate at the facility, both the tracer and methane gas are measured downwind and estimates of methane leaks are performed, and c.) Inverse methods which estimate leaks based on downwind concentration measurements and good knowledge of wind flow. Onsite measurements are typically larger than can be measured using CRDS and FLIR cameras or simple direct absorption measurements. Downwind measurements require very sensitive measurements of methane as plumes can be only a few ppbv to ppmv above background (1.8 ppmv).

While oil and gas is one area of study for determining methane emissions, methane is also emitted from waste treatment facilities (waste water treatment, landfills). Using the tracer method, methane emissions from a waste water treatment facility were performed in Valence, France²². Acetylene (C₂H₂) was released onsite while methane and acetylene were measured on a mobile platform downwind of the facility. Acetylene is used as a tracer as it is relatively chemically stable in the lower atmosphere and the ratio of the area of the two plumes is proportional to the emission rate.

Methane emissions were estimated from 130 gathering and processing facilities across the top 10 gas producing states and basins (Green River Basin, Uinta Basin, San Juan Basin, Anadarko Basin, etc.) and were targeting diversity in measurement sites in age, inlet gas

composition, regulatory environment and operations²³. At each facility, N₂O and C₂H₄ were released at known flow rates onsite. A mobile laboratory then measured both tracer gases and methane upwind as well as downwind of the facility to identify any background contamination. Downwind measurements were taken (both stationary and mobile) for ~1-5 hours at each facility. Depending on the measurements, the two tracers were correlated to the methane emissions through either dual correlation with both tracers, single correlation method²⁴ or a linear combination of the two tracers.

A study was performed in the Barnett Shale region in Texas in 2013 as part of the Barnett Shale Coordinated Campaign to develop top-down and bottom-up estimates of methane emissions in the region²⁵. One of the conclusions of the study was that bottom-up estimates of oil and gas estimates were ~1.5 larger than expected, largely due to inclusion of more compressor stations. As part of this study, Picarro used their ground-based mobile flux plane (MFP) measurement system to quantify emissions from nearly 200 well pads, finding that 50% of the emissions they measured were due to the highest 6.6% pads. In their technique, a vehicle with a closed-path methane analyzer, GPS and anemometer (corrected for motion of vehicle) are driven downwind of a well pad. The sampling inlet for the sensor has a vertical series of inlet ports, this 2-d map of the concentration measurements along with wind can be used to determine the emission rate.

Field studies in Texas Colorado and Wyoming were performed between 2010-2013 to test another wind-based system to determine emission rates. The approach, Other Test Method (OTM 33A)²⁶ uses a methane sensor (Picarro) and anemometer mounted to a vehicle, with a secondary met station (including wind) located onsite. After a plume was located, the vehicle

was parked in the plume for 15-20 minutes and emission rates were determined using a point source Gaussian approach.

1.3 Dissertation Outline

The objective of this work was to design, build, and test a small, mobile open-path cavity ring-down spectrometer for the measurement of atmospheric methane gas from oil and gas operations. By adapting the sensor for open-path configuration, the size and power of the sensor can be dramatically reduced so the mobile package could be small enough for UAV deployment.

Chapter 2 discusses the concepts of spectroscopy and how this can be utilized to measure trace atmospheric gasses. A brief discussion of methods that utilized laser-based spectroscopy is presented along with some of their benefits and drawbacks. Chapter 3 discusses the technical details of the technique used in this study, Cavity ring-down spectroscopy (CRDS). Our sensor differs from typical CRDS sensors by use of an open-path cavity and the advantages and drawbacks of such a setup are debated. The spectral regions studied by the sensor in this work are discussed as well as the spectral fitting performed due to open-path configuration of the sensor. Chapter 4 discusses the optical, mechanical and electronic setups for the sensor. The open-path sensor was developed in three phases (Phase-I, Phase-II, & Phase-III), from the first modifications to an open-path sensor through two iterations of a mobile, outdoor versions. The details of how each optical component is part of the sensor is discussed, details on the electronics used in the sensor and how the sensor control and analysis are also discussed. Changes and improvements to the optics, electronics and physical setup are described.

Chapter 5 discusses results of laboratory testing of the sensitivity and precision of the sensor. Sensitivity studies were determined for each phase of the sensor through studies of Allan variance of ring-down and concentration measurements. Precision studies were performed

through closed-path measurements of cylinder gas as well as comparison with a commercially available methane sensor (Picarro). Mobile measurements are discussed in Chapter 6 beginning with comparison of the Phase-II sensor and Picarro in oil and gas fields in Platteville, CO, demonstrating the ability of the sensor to make measurements in the desired application location with dirt roads, and varying distances away from oil and gas facilities. Phase-III results are shown for controlled leaks at the METEC facility in Fort Collins. Leaks were detected for a range of release rates and preliminary analysis has been performed by John Alberton's group from Cornell University to determine leak rates based on concentration and wind measurements. Integrated plume measurements were calculated to investigate different scan rates of the open-path sensor. Measurements of controlled leaks were compared for the open-path and Picarro sensor. Results from a field study in Marcellus County, PA are presented where the methane sensor was used to identify methane leaks for real-time and speciated VOC measurements. Finally, description and preliminary results are shown of the sensor integration into a UAV system for measurement of methane and ammonia downwind of a dairy. Techniques and results, although taken for agricultural reasons are applicable for measurements of any site (agriculture, oil and gas, waste treatment) where methane emissions are desired. Final conclusions and recommendations for further sensor improvement are discussed in Chapter 7.

CHAPTER 2:

Spectroscopy

2.1 Introduction

Spectroscopy is the study of the interaction between electromagnetic (EM) radiation and matter. The energy, E , of a photon is related to its wavelength, λ , or frequency ν , through the Planck-Einstein relationship

$$E = h \frac{c}{\lambda} = h\nu \quad (2.1)$$

where c is the speed of light and h is the Planck constant. The electromagnetic spectrum (Figure 2.1) ranges from very high energy gamma rays (10^{-12} m) to lower energy radio waves (10^3 m), while only a small range, called the visible spectrum (10^{-8} m) is visible to the human eye. The interaction between light and matter varies depending on the energy of light. High energy, short wavelength light (Gamma ray, X-ray) typically causes ionization of atoms, whereby an atom loses an electron and becomes positively charged. Ultraviolet and visible light typically interact with atoms to excite electrons from one energy level to another and was one of the first areas where spectroscopy applications were developed. Infrared radiation can excite molecule to rotate or vibrate along its axis, and can have complex interactions depending on the configuration of the molecule. Lower energy light, in the microwave and radio regions, can cause excitation of the nuclear spin state of atoms and can be investigated using Nuclear Magnetic Resonance (NMR). Because the interaction between light and matter depends on properties of each atom or molecule, it produces a unique signature and can be exploited for scientific measurement and study.

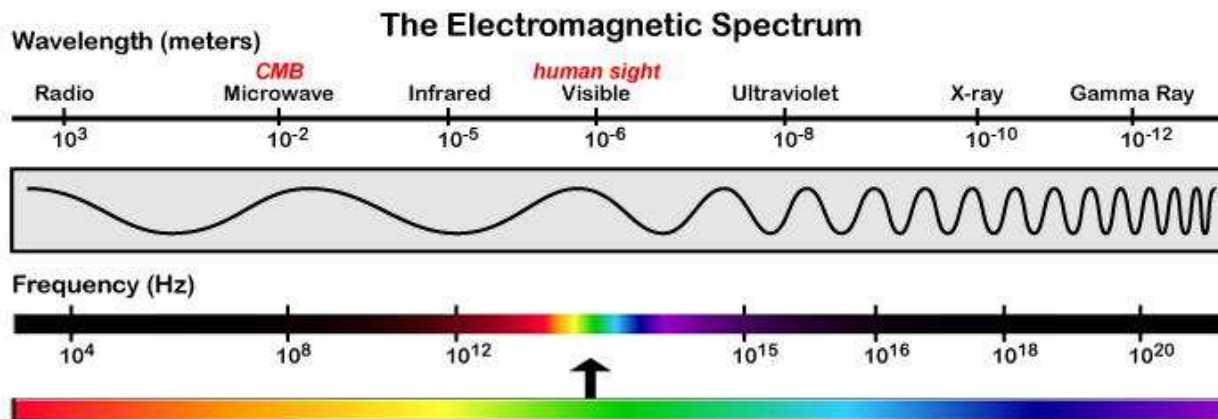


Figure 2.1: The Electromagnetic spectrum

The nature of the interaction between light and matter can also vary. Emission occurs when matter (spontaneously or not) emits radiative energy. Absorption occurs when incoming energy is absorbed and can occur across the electromagnetic spectrum. Scattering describes how incoming radiation can be reflected by matter. During elastic scattering, the incoming light is identically reflected while in-elastic scattering involves an exchange in energy between the incoming light and the matter, and the reflected light is shifted. This work focuses on the absorption of energy by the molecule, methane (CH_4).

2.2 Absorption

The absorption, or attenuation, of light through a material (gas, liquid or solid) can be measured by observing the decrease in energy through the material, and is described by the Beer-Lambert Law

$$I = I_0 \exp(-\alpha(\nu)L) = I_0 \exp(-k(\nu)L) \quad (2.2)$$

where I_0 is the intensity of the incident light, I is the intensity of the light exiting the material, α is the absorbance of the material and is dependent on the frequency, ν , of the light. Absorbance

can also be described by the absorption coefficient k , the absorbance per unit length, L , of the material. The absorption coefficient is given by

$$k(\nu) = S\phi(\nu)P_i = S\phi(\nu)Px \quad (2.3)$$

where S is the line strength of the transition, P_i is the partial pressure of the absorbing species and $\phi(\nu)$ is the line shape. Absorption coefficient can be written in terms of species concentration, x , by substituting in the relationship between partial pressure and concentration.

Although the Planck-Einstein relationship (Eqn (2.1)) suggests that there is a discrete relationship between wavelength and molecular absorption, absorption features are broadened due to interactions with other molecules and temperature affects and frequency dependent line shapes describe these interactions.

The thermal motion of molecules causes a distribution of (relative) velocities between the light beam and the molecules, which leads to frequency shifts of the absorbed light. Doppler broadening describes the change in absorption energy due to the velocity of molecules and is dependent on temperature. As this broadening depends on the speed of the molecules relative to the light, it is what is referred to as inhomogeneous broadening and is described by a Gaussian line shape

$$\phi_D(\nu) = \frac{1}{\Delta\nu_D\sqrt{\pi}} e^{-\left(\frac{(\nu-\nu_0)^2}{(\Delta\nu_D)^2}\right)} \quad (2.4)$$

where the width, $\Delta\nu_D$, is given by the full width half maximum (FWHM) and is determined by

$$\Delta v_D = \sqrt{\frac{8kT \ln 2}{mc^2}} v_0 \quad (2.5)$$

where k is the Boltzman constant, T is temperature, m is the mass is the molecule and c is the speed of light.

Energy may also be transferred between molecules and states through collisions. Collisions decrease the lifetime that a molecule is in a specific state, increasing the uncertainty and giving a broader line shape. This effect applies equally to all molecules, so it is what is described as a homogenous effect and is described by a Lorentzian function.

$$\phi_L(\nu) = \frac{1}{2\pi} \frac{\Delta\nu_L}{(\nu - \nu_0)^2 + \left(\frac{\Delta\nu_L}{2}\right)^2} \quad (2.6)$$

where $\Delta\nu_L$ is the full width half maximum (FWHM) of the Lorentz. This width describes the net uncertainty due to collisions between any molecules present and can be modeled by

$$\Delta\nu_L = P \sum X_A 2\gamma_{B-A} \quad (2.7)$$

where P is the pressure, X is the concentration of the species A which is colliding with the species being studied, B , and γ is the broadening coefficient describing that collision.

Doppler broadening is dominated by temperature while Collisional broadening is largely determined by pressure. The Gaussian (Doppler) line shapes have peaks which are ~50% taller than Lorentzian (Collisional) while the Lorentzian wings persist much longer (Figure 2.2). When contributions from both line shapes are significant (typical for trace gas spectroscopy detection), a combination of the two line shapes is necessary. The convolution of these two broadening mechanisms is described by the Voigt profile

$$V(\nu, \Delta\nu_D, \Delta\nu_L) = \int_{-\infty}^{\infty} G(\nu, \Delta\nu_D)L(\nu, \Delta\nu_L)d\nu \quad (2.8)$$

where $G(\nu, \Delta\nu_D)$ and $L(\nu, \Delta\nu_L)$ represent the Gaussian and Lorentzian line shapes. A number of empirical solutions, and reference tables exist for the Voigt profile^{27,28} if it is necessary to use.

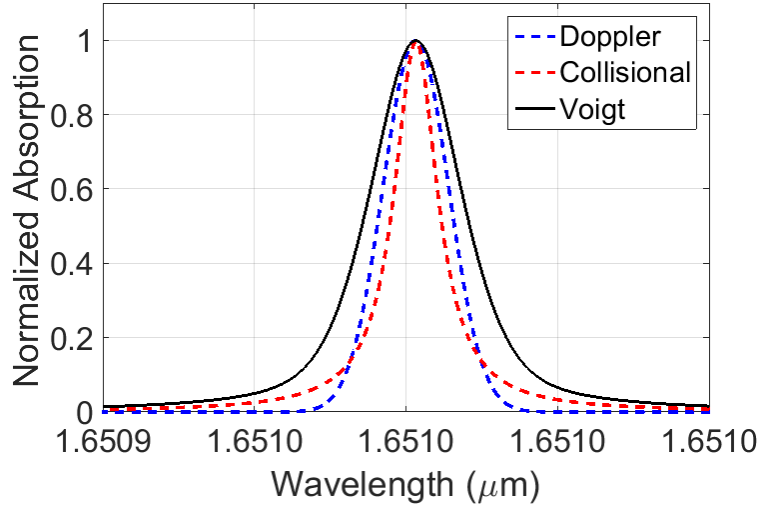


Figure 2.2: Simulated Normalized Doppler, Collisional broadening and Voigt convolution for methane absorption at 1651nm for P=0.1 atm and T=296 K.

Line strength, S , and broadening coefficients, ϕ , have been determined experimentally and can be found for most commonly studied molecular lines in Hitran (**high-resolution transmission molecular absorption database**)²⁹.

2.3 Methane Absorption

Methane absorption (Figure 2.3) is dominated by absorption in the mid-infrared (MIR) at 3.6 μm with weaker absorption in the far infrared (FIR), 7.5 μm and near infrared (NIR), 1.6 μm .

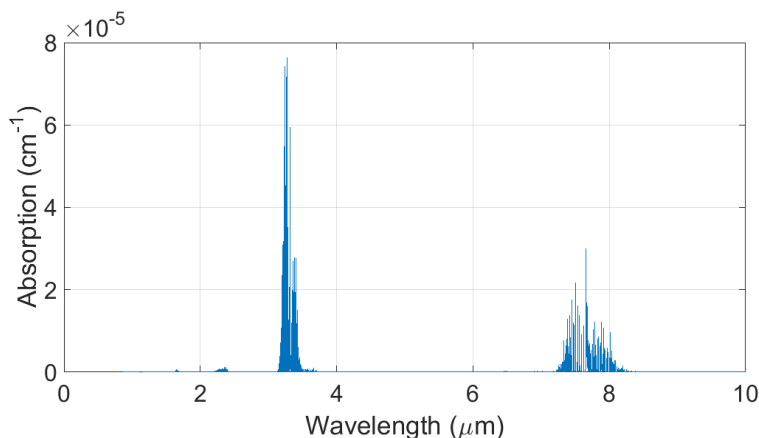


Figure 2.3: Simulated methane absorption for typical atmospheric conditions, $T=296\text{ K}$ $P=0.84\text{ atm}$ and $[\text{CH}_4]=1.8\text{ ppmv}$.

Methane is a symmetric, tetrahedral, molecule (a spherical top molecule) and as such has equal moments of inertia along each of its axes and a net dipole moment of zero. Because of this, the fundamental absorption lines at $3.3\text{ }\mu\text{m}$ and $7.5\text{ }\mu\text{m}$ are caused by vibration-stretching of the molecule and there are no pure rotational bands; although very weak forbidden rotational bands exist. The bands at $3.3\text{ }\mu\text{m}$ are caused by stretching vibrations, while those at $7.5\text{ }\mu\text{m}$ are due to bending vibrations. Weaker absorption at $1.6\text{ }\mu\text{m}$ is due to an overtone of the fundamental rotational-vibration bands. Atmospheric methane spectroscopy has typically been performed in the NIR ($1.6\text{ }\mu\text{m}$) region due to the cost and availability of lasers and optical equipment in this region, although recent advances in Quantum Cascade Lasers (QCL's) and Intraband Cascade Lasers (ICL's) are making the MIR region more exciting^{30,31}.

2.4 Measurement Techniques

When concentrations of methane are high enough (such as direct leak measurements), direct absorption measurements can be made where a laser is directed through the sample with a detector on the other side. Concentration can be determined either by measuring the drop in laser power at a single frequency tuned to the peak or by tuning the laser across the peak, where

the spectra can be measured and fit to determine concentration. Typical ambient concentrations of methane are quite small (background 1.8 ppmv) and as such, more sensitive measurement techniques are necessary. The easiest way to increase sensitivity is to change is the path length over which the sample is detected.

DOAS (Differential Optical Absorption Spectroscopy) uses either the sun (or moon) as a passive light source, or uses an active light source to measure the decrease in light along a long path. For this method, it is assumed that the concentration is constant along the entire beam path, and a reference signal of the initial light source must be known. If a passive source (sun/moon) is used, two atmospheric paths must be used to determine the initial light source. DOAS is used for ground based sensors, but is also a useful satellite technique³² to obtain large scale estimates of methane concentration, with sensitivities down to 0.6 ppmv³³ for the lower atmosphere.

Several other techniques utilize long-path ideas in a small physical package using optics. Herriott Cells³⁴ are multi-pass absorption cells that improve sensitivity by folding a long-path length into a small cell through alignment of mirrors to control a beam into and out of the cell. The Curiosity rover which landed on Mars in 2012 contained a methane sensor which utilized a Herriott Cell^{35,36} (concurrent with Wavelength Modulation Spectroscopy WMS) and had a sensitivity of 0.1 ppbv. WMS is often used in combination with Herriott cells for improved sensitivity where by signal processing is performed on a doubly modulated signal to determine concentration.

Finally, some techniques improve sensitivity by coupling the laser beam into an optical cavity to increase the optical path length by using high reflectivity mirrors, as well as enhancing the laser signal in the cavity. Integrated cavity output Spectroscopy (ICOS)³⁷, sometimes referred to as cavity-enhanced absorption spectroscopy (CAES) couples a laser into a high-

finesse cavity while monitoring the integrated output behind one of the mirrors. In this technique the laser is scanned faster than the ring down time of the cavity, while the laser wavelength and cavity length are modulated, to produce a flat integrated signal at the output. This technique is starting to be more frequently used in atmospheric measurements^{38,39} but is more sensitive to laser noise and drift. The work presented here uses Cavity Ring-Down Spectroscopy, which uses a high-finesse cavity to couple and enhance the laser signal while also increasing the optical cavity length to increase the sensitivity. This technique is popular for measurements of atmospheric trace gasses⁴⁰⁻⁴³ due to its high sensitivity and small optical path length and as compared to ICOS, it is purely time based and insensitive to laser fluctuations or drift. In the following chapter, I will discuss this technique in more detail and how we modified it for open-path configuration.

CHAPTER 3:

Cavity Ring-down Spectroscopy

3.1 Theory

Cavity ring-down spectroscopy (CRDS) is a direct absorption measurement technique formalized by O'Keefe and Deacon in 1988⁴⁴ for the measurement of weak molecular absorption through the decay of light in a high-finesse cavity. Concentration is determined by measuring the decrease of light through a sample, following Beers law (Eqn (2.2)). Laser light is introduced into a high-finesse optical cavity comprised of two or more high-reflectivity mirrors (typically $R > 0.999$), which increase the effective optical path length from < 1 m to > 1 km, increasing the sensitivity of the sensor. When the laser is at resonance with the optical cavity, intensity builds due to constructive interference. When the laser is turned off, the rate at which the light decays is proportional to the extinction per unit length, $k(\nu)$, in the cavity

$$I = I_0 \exp(k(\nu)L) = I_0 \exp\left(\frac{-t}{\tau(\nu)}\right) \quad (3.1)$$

where I is the measured light upon exit, I_0 is the light entering the cavity, L is the physical cavity length, t is time and τ is the characteristic decay, known as ring-down time. For an empty cavity, this decay depends only on physical characteristics of the cavity, cavity length, L and mirror reflectivity R

$$\tau(\nu) = \frac{L}{ck(\nu)} = \frac{L}{c \ln R} \quad (3.2)$$

For typical values of $R > 0.999$, τ can be approximated as

$$\tau = \frac{L}{c(1 - R)} \quad (3.3)$$

When a sample is present in the cavity, the lifetime of the light will decrease

$$\tau = \frac{L}{c(1 - R) + k_g L + k_a L} \quad (3.4)$$

due to scattering and absorption of gases and aerosols, where k is the total light extinction due to each.

To achieve resonance, the laser beam is ‘mode-matched’ to the optical cavity where by the fundamental TEM_{0,0} mode of the laser is matched to the optical cavity. The properties of a Gaussian beam can be fully determined by knowing the radius of curvature, R , and waist, ω of a beam at a specific location, z

$$\omega(z) = \omega_0 \sqrt{1 + \left(\frac{z}{Z_R}\right)^2} \quad (3.5)$$

$$R(z) = z \left[1 + \left(\frac{Z_R}{z}\right)^2\right] \quad (3.6)$$

where ω_0 is the beam waist, and Z_R is the Rayleigh range, the distance over which the beam remains within $\sqrt{2}$ of the beam waist, of the beam.

$$Z_R = \frac{\pi \omega_0^2}{\lambda} \quad (3.7)$$

Mode matching of the laser beam occurs when the Gaussian characteristics of the beam are matched to that of the optical cavity. This is typically done using lenses to shape the exterior laser beam so that it is identical to the cavity when it goes through the mirror. By precisely overlapping the beam to the cavity, the beam will couple into the cavity and resonance will occur when the laser wavelength is $\frac{1}{2}$ integer of the cavity free spectral range (FSR)

$$FSR = \frac{1}{2nL} \quad (3.8)$$

where n is the refractive index of the material in the cavity, assumed to be $n=1$ for air, and L is the physical distance between the mirrors.

Some CRDS sensors use a technique where by the laser is locked to the cavity⁴⁰ and wavelength is scanned by piezoelectrically modulating the cavity. We use a non-locked method whereby cavity length is fixed and the laser is scanned over wavelength. A continuous-wave (CW) laser is scanned over a narrow wavelength range (< 1 nm) to observe a series of cavity resonance⁴⁵. When a cavity resonance is observed by the detector at the output of the cavity, a signal is sent to an acoustic optical modulator (AOM) which acts as an optical switch to divert the laser signal from the optical cavity. The resonance in the cavity is allowed to decay and τ is measured. A signal is sent to the AOM to divert the laser back through the optical cavity and the next resonance is anticipated. By measuring τ across a series of resonances (wavelengths), a spectrum may be measured and concentration determined.

CRDS is advantageous over other spectroscopic techniques for several reasons. Due to the long optical path lengths, it is sensitive to very small changes in laser signal and thus small gas concentrations, down to ppbv, or pptv^{46,47}. As only the time it takes for the light to decay is measured, pulse to pulse variations in laser power do not affect this technique. Additionally, τ is an absolute measurement and concentration is determined through known spectral characteristics, therefore the sensor does not require calibration.

Disadvantages to CRDS include the need for high-reflectivity mirrors which are customized for specific wavelengths and as such can be expensive, have narrow wavelength range applicability and difficult to obtain for some regions (MIR). Due to the small tuning

capabilities and wavelength specific mirror coatings, a CRDS is typically limited to the specific spectral region it was designed for. Finally, CRDS sensors can be fairly heavy with too much power draw for useable deployment in remote environments.

3.2 Open-path CRDS

Most CRDS sensors used in atmospheric science^{43,46,48} use a closed-path flow cell configuration where a vacuum pump pulls the sample through a flow cell located between HR mirrors. The closed-path flow cell architecture is primarily used to lower the sample pressure, typically to ~0.1 atm, to narrow the spectral lines as well as fix pressure and temperature which are necessary to determine gas concentration. Secondly a flow cell is used to maintain the high mirror reflectivity of the mirrors by using a weak purge flow of zero-air (or an inert gas) near the HR surfaces to provide a buffer against potentially contaminating sample constituents. For some ‘sticky’ or reactive species (HCl, NH₃), the gas being sampled can interact with the flow system and special materials and heating systems are needed to reduce sample absorption in the inlet. Finally, and less frequently discussed, is that the closed-cell configuration allows use of particulate filters or virtual impactors to prevent ambient aerosol particles from entering the optical cavity, reducing signal fluctuations due to particle optical extinction. While CRDS sensors have been designed specifically to measure optical extinction of aerosol particles⁴⁹⁻⁵¹, this produces a noise in the signal when measuring gases. Effects of particle extinction in gas-phase CRDS have been noted by several researchers^{40,52,53}. Romanini *et al.* noted a baseline difference in measurements between open air and evacuated cell, due to the scattering by submicron dust particles, which contributed a spectrally flat absorption. Morville *et al.* noted reductions in ring-down times, often over several consecutive ring-down acquisitions, due to

large aerosol particles crossing the beam path. The total light extinction of aerosols, σ_{ext} , is due to both absorption and scattering of particles and can be calculated from the size distribution as:

$$\alpha_{ext} = \int N(D_p)\sigma_{ext}(D_p)dD_p \quad (3.9)$$

where N is the number of particles per unit volume with mean diameter D_p and σ_{ext} is the corresponding extinction cross section. (3.9 assumes a single species of aerosol composition; if different species are present then the contributions from each should be separately found and added.

Open-path configurations can provide several important advantages for practical sensor operation. Removing the pump and flow cell can dramatically reduce the size, mass, and power draw of CRDS instruments, for example from ~27 kg and ~250 W for typical commercial instruments⁵⁴ to ~4 kg and ~30 W, based on the opto-electronic components of the sensor design. Smaller and less power hungry sensors have potential for more remote deployment, for example where only solar-cell power is available or on small unmanned aerial systems (UAS). Removing the flow inlet also increases the accuracy and time-response for measurements of “sticky gases” such as NH₃ or HCl for which inlet adsorption and memory effects can be problematic⁵⁵. Finally, the temporal response of open-path instruments can more faithfully reflect the ambient conditions, rather than being limited by lag and cell transit times of the flow system.

Only limited work is available in the literature on the use of open-path CRDS instruments for ambient air. He et al.⁵⁶ described development of an open-path system for measurements of NH₃, but did not provide detailed sensitivity characterizations or extensive discussion of aerosol effects. Wada⁴² and Bitter⁵⁷ employed open-path CRDS for measurement of sticky marine

gases, but either assume aerosol influence is below noise level or assume aerosols provide a linear offset which can be subtracted. Recently an open-path CRDS sensor was developed for measurements of aerosol extinction⁵⁸, using the open-path cell configuration to measure humid particles. Other past work with open-path CRDS, for example for combustion flames^{59,60} or atmospheric plasmas⁶¹, employed less sensitive pulsed laser setups where effects of particle extinction or mirror degradation are much diminished.

3.3 Development of an open-path Methane CRDS sensor

This work focuses on absorption in the NIR (Figure 3.1) although the techniques described could be applied to the stronger absorption in the MIR. Simulations shown were done using parameters from Hitran 2012⁶², assuming typical atmospheric conditions for Fort Collins, Colorado.

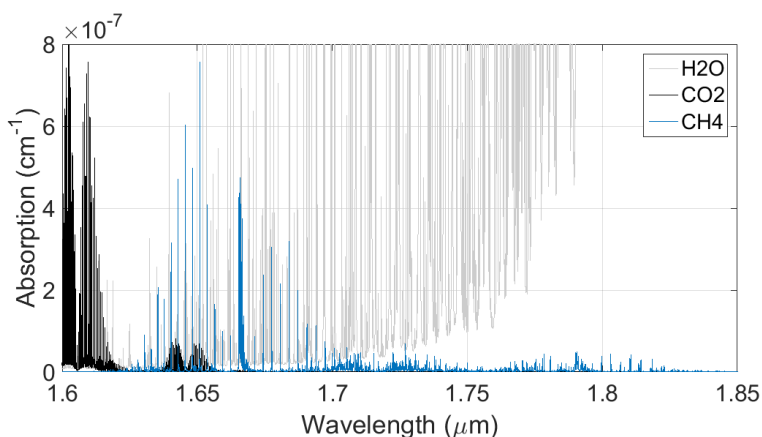


Figure 3.1: Simulated absorption in the NIR for typical atmospheric conditions, $T=296$ K, $P=0.84$ atm, $[CH_4]=1.8$ ppmv, $H_2O=0.013$ and $[CO_2]=460$ ppmv.

The open-path CRDS methane sensor was developed over three phases (Phase-1 through Phase III). The initial Phase-1 sensor was developed by modifying a previously constructed closed path HCl sensor centered near 1742 nm⁴⁶. From Figure 3.1 it can be seen that this region is dominated by absorption from H_2O . Figure 3.2 shows spectral simulation of the measurement

region of the sensor in open-path configuration ($P=0.84$ atm) which targets a pair of methane absorption lines at 1742.2 nm and 1742.25 nm (~ 5739.69 cm^{-1} and ~ 5739.85 cm^{-1}). Owing to the relatively high pressure, the absorption peaks have become considerably broadened and overlap with one another (compared to closed-cell operation where the peaks would be ~ 4 times narrower).

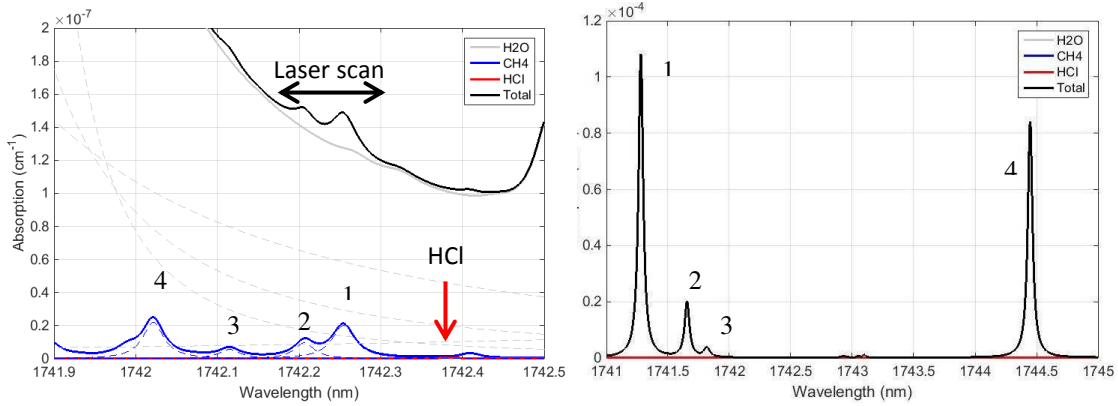


Figure 3.2 Simulation of region measured by open-path sensor at 1.7 μm for typical atmospheric conditions, $T=296$ K, $P=0.84$ atm, $[\text{CH}_4]=1.8$ ppmv, $[\text{H}_2\text{O}]=50\%$ RH, $[\text{HCl}]=0.5$ ppbv. Left: Zoomed in look at region scanned by laser and 4 methane peaks included in synthetic spectrum and the region scanned by the laser.

Typically, a Voigt approximation would be used to fit the methane peak and determine concentration. After simulating this spectral region using the Whiting approximation²⁸ for a Voigt profile, the difference between Voigt and Lorentzian lineshapes were found to be negligible, indicating only a small influence from Doppler broadening and a simpler Lorentzian line shape (Eqn (2.6) was used for all simulations and fits.

When HCl was measured in this region under low pressure, peaks were sufficiently narrowed so that the nearby water did not interfere. Under higher pressure conditions, nearby H_2O and CH_4 peaks were investigated to determine which ones might have a non-zero tail in the region of the peaks of interest. It was determined that two additional CH_4 lines and four H_2O

lines also needed to be considered in the fit of the data: CH₄ peaks located at 5740.15, and 5740.46 cm⁻¹, and H₂O peaks located at 5732.47, 5741.13, 5741.66, and 5742.90 cm⁻¹.

Concentration is found by recording ring-down, $\tau(\nu)$, versus laser frequency, and converting to absorption $k(\nu)$. The measured absorption spectrum is fit with a synthetic spectrum consisting of a sum of Lorentzians for each peak being considered.

$$k(\nu) = b + \sum_{i=1}^8 \phi_L(\nu, \nu_{0i}, \Delta\nu_i) P S_i n_i \quad (3.10)$$

where b is the cavity baseline absorption (units of cm⁻¹), i is an index to sum over the 8 lines used, ϕ_L are frequency-normalized Lorentzian lineshapes with center frequency ν_{0i} and width $\Delta\nu_i$ (units of cm⁻¹), P is the pressure (units of atm), S_i the line strength (expressed in units of cm⁻²atm⁻¹), and n_i the species concentration (in units of cm⁻³); $\Delta\nu_i$ and S_i are determined from HITRAN. The fit has 4 free parameters: the baseline loss (nominally the loss from just the cavity itself, but it also accounts for additional baseline shifts due to changes in mirror reflectivity, or broad spectrum absorption from interferents), a peak frequency offset (as the experiment uses relative frequency and to account for possible laser wavelength drift), CH₄ concentration, and H₂O concentration. The suitability of the synthetic spectrum was confirmed by fitting a full simulated spectrum (all spectral lines from all species at typical ambient conditions) with the synthetic spectrum, and recovering the starting concentration. Determination of concentration also requires accurate knowledge of temperature and pressure owing to the temperature dependence of S_i and $\Delta\nu_i$, on pressure, and dependence of total gas density on both. During Phase-I and Phase-II, average values obtained from local weather stations were used while Phase-III included real time temperature and pressure measurements.

Going forward to Phase-II, the wavelength was shifted to the peak of the NIR absorption, 1651 nm. This spectral region is ~37x stronger than at 1742 nm with less interference from other peaks (CH₄, H₂O, CO₂). At atmospheric pressure, the region is dominated by a large methane feature, composed of several overlapping peaks with a small CO₂ peak and a small H₂O peak on each side (Figure 3.3). Simulations showed that in atmospheric pressure, Doppler broadening could again be ignored and this feature could be simulated as a Lorentzian.

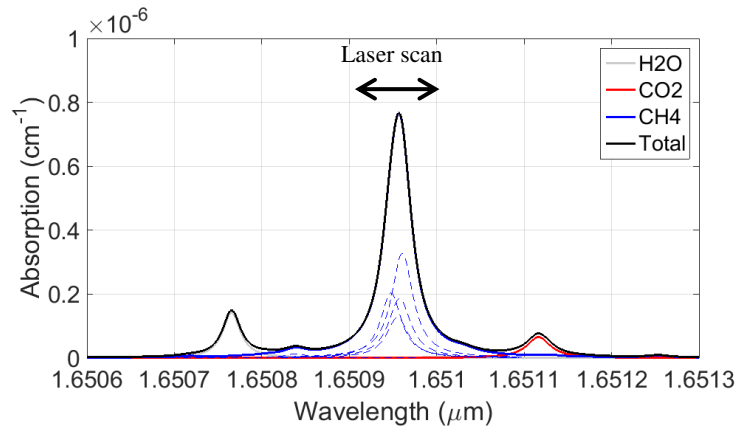


Figure 3.3 Simulation of region measured by open-path sensor at 1.651 μm for typical atmospheric conditions, T=296 K, P=0.84 atm, [CH₄]=1.8 ppmv, [H₂O]=50% RH, [CO₂]=380 ppbv. Dashed lines show the four methane peaks used in the synthetic spectrum and the region scanned by the laser.

Although there are CO₂ and H₂O peaks nearby, only four methane peaks were included in the synthetic spectrum: 6057.08, 6057.13, 6057.09, and 6057.10 cm⁻¹; based on the laser scan region chosen, the CO₂ and H₂O peaks were determined to be far enough away not to be included. The measured absorption spectrum was fit with a synthetic spectrum based on the aforementioned lines:

$$k(\nu) = b + \sum_{i=1}^4 \phi_L(\nu, \nu_{0i}, \Delta\nu_i) P S_i n_i \quad (3.11)$$

where b is the cavity baseline loss (units of cm⁻¹), i is an index to sum over the 4 lines used, ϕ_L are frequency-normalized Lorentzian lineshapes with center frequency ν_{0i} and width $\Delta\nu_i$

determined from HITRAN parameters (units of cm^{-1}), P is the pressure (units of atm), S_i the line strength (expressed in units of $\text{cm}^{-2}\text{atm}^{-1}$), and n_i the species concentration (in units of cm^{-3}). The fit has 3 free parameters: the baseline loss, frequency offset and methane concentration. For this region, the laser was scanned over the region 1650.89 – 1651.03 nm ($6056.84 - 6057.34 \text{ cm}^{-1}$).

CHAPTER 4:

Development and Design of Open-Path Sensor

The development of the open-path CRDS sensor was described by three different iterations. Phase-I was a laboratory based sensor using large lab-grade electronics, based on a previous closed-path HCl sensor⁴⁶, and mounted on a cart. The primary purpose of Phase-I was to examine the capabilities of an open-path sensor, with some beginning mobile tests. Phase-II was a more compact prototype mobile sensor, moving towards more custom electronics to shrink the overall foot print of the sensor and optimizing the optical measurement by moving to a stronger wavelength region. Phase-II was exposed to more mobile testing to examine where the design could be further improved, assuming the capabilities of an open-path sensor. Phase-III expanded on the concepts of Phase-II, further reducing both the size and weight of the sensor as well as improving its ruggedness for year-round outdoor use. All three versions of the sensor used the same non cavity-locked, frequency-scanned CRDS as described in the previous chapter, although the physical layout changed slightly between iterations

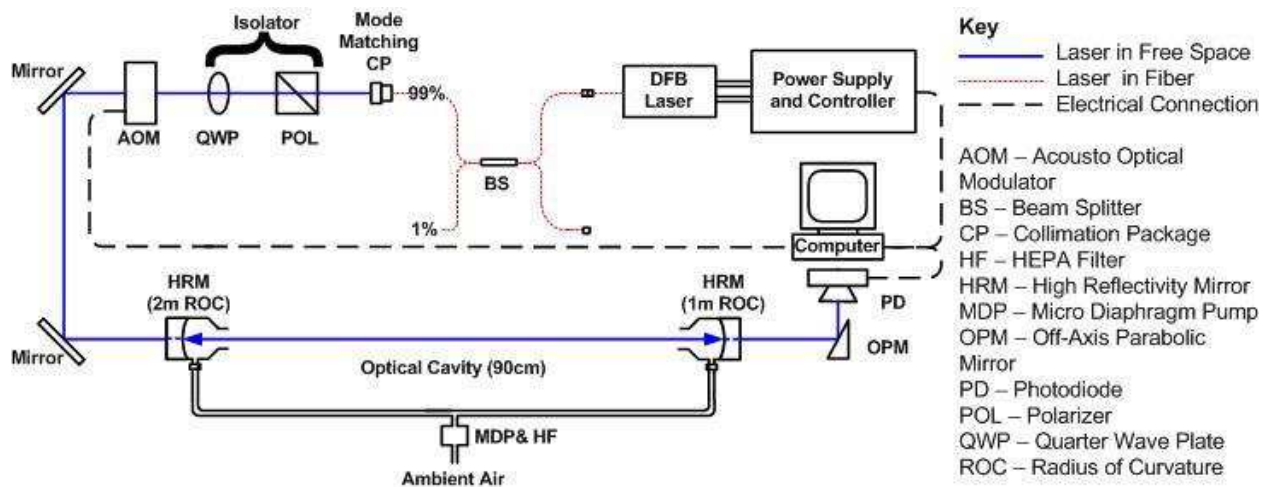


Figure 4.1: Optical layout of the sensor, Phase-I using a 1742 nm laser.

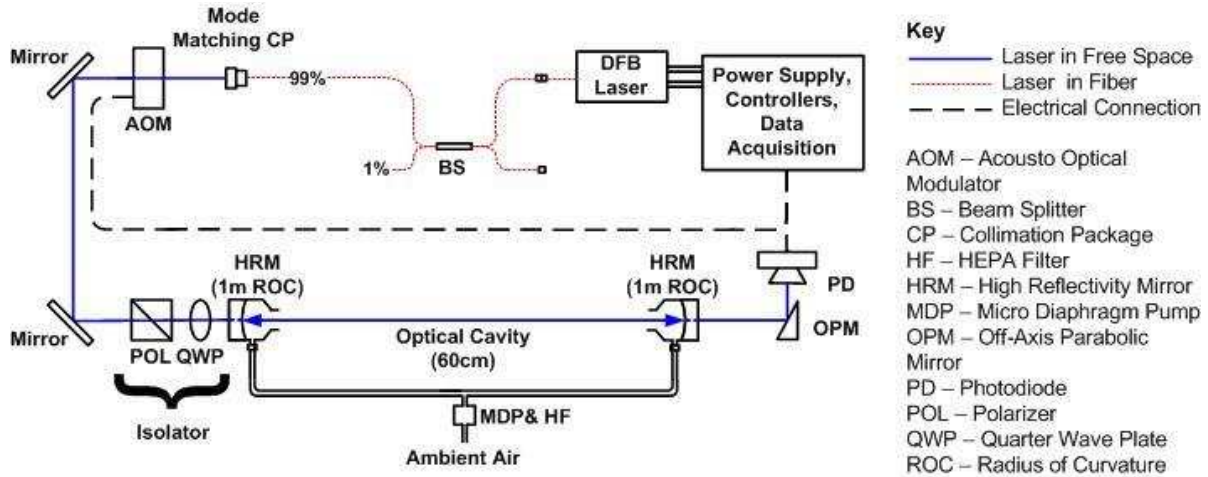


Figure 4.2: Optical layout of the sensor, Phase-II using a 1651 nm laser with changes to the location of the isolator, HRM and Data Acquisition system and some reduction in the overall footprint.

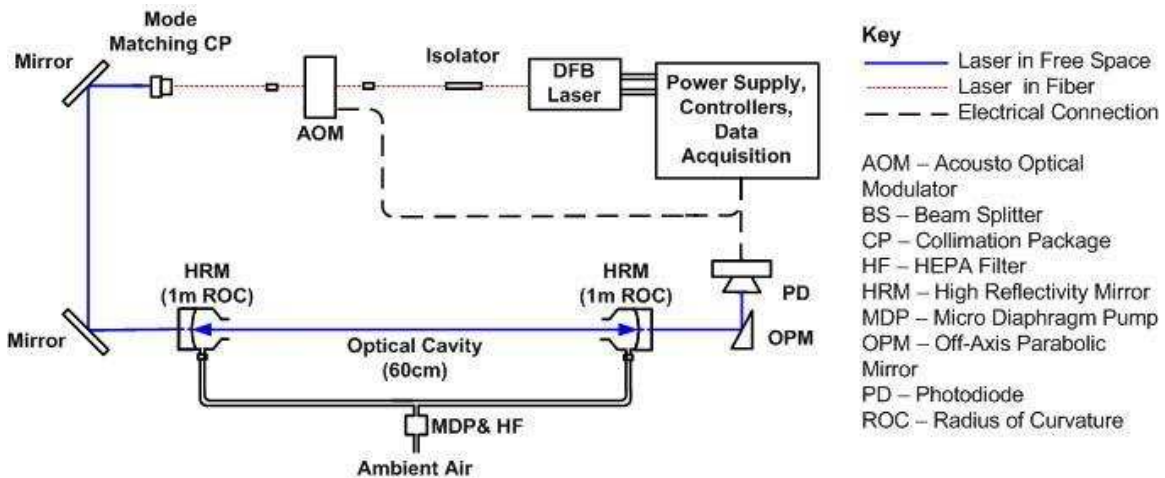


Figure 4.3: Optical layout of sensor Phase-III where the optical isolator and AOM have been moved in line with the fiber optic and the overall footprint has decreased.

4.1 Optics

A continuous wave distributed feedback (DFB) diode laser in a 14-pin butterfly package is used in this sensor. Power output was ~13 mW for all three sensors, output through a single mode fiber coupled to the package. These lasers are relatively inexpensive and available due to their use in the telecom industry and integration into small systems is easy through their small package size. Laser wavelength (and power) can be adjusted by changing the TEC temperature

or current sent through the diode. The first optic in the sensor is an adjustable focus aspheric FC collimator, designed to collimate light exiting a fiber. As discussed in section 3.1, this lens is adjusted to match the laser to the optical cavity and obtain resonance. The focal length of the collimation lens was changed from Phase-II to Phase-III (Thorlabs CFC-11X-C to CFC-8X-C) to reduce the distance from the lens to the first cavity mirror from 33cm to 18cm, reducing the overall sensor footprint.

High reflectivity mirrors define the optical cavity of the sensor. All three versions of the sensor utilized fused silica mirrors that use a dielectric coating for maximum reflectivity at 1742nm (ATF Films), giving $R \sim 0.999982$ for Phase-I, but $R \sim 0.999943$ for Phase-II and Phase-III when the laser wavelength was moved to 1651 nm. These same mirrors were kept when the laser was switched to 1651 nm because although the reflectivity dropped off, it was still sufficient for measurement and they were preferable for data acquisition speed considerations, to be discussed later. The mirrors employ a very small (0.5°) wedge to prevent laser inference (etalon effect) in the mirror. Mirror diameter was decreased from 1" to $\frac{1}{2}$ " for Phase-III, as the mirror mounts used were significantly smaller and lighter and this reduced the overall size and weight of the sensor. The length of the optical cavity was decreased from 90 cm to 60 cm after Phase-I to reduce the overall footprint of the sensor; this was possible by changing the radius of curvature of the mirrors from $R_1=1$ m and $R_2=2$ m to $R_1=R_2=1$ m.

When the laser passes through the high reflectivity cavity mirrors, only a small fraction of the light ($T \sim 1-R$) passes through the mirror and the rest is reflected back along the incoming path. This reflected light will trace its original path, back into the laser which could cause feedback or potential etalon interference. To remove the back reflection, an optical isolator is placed between the laser and the optical cavity. In Phase-I and Phase-II, the optical isolator was

comprised of a linear polarizer (Thorlabs, LPNIR050-MP) and quarter wave-plate (Thorlabs, AQCWP05M-1600) as shown in Figure 4.4. The light passes through the polarizer, limiting the light to that parallel to the orientation of polarization. The light is converted from linearly polarized to circular after passing through the quarter wave-plate. The returning beam passes back through the quarter wave-plate, going from circular to linear, but it is now converted 90 degrees compared to the incoming beam and is thus blocked by the polarizer on the return journey.

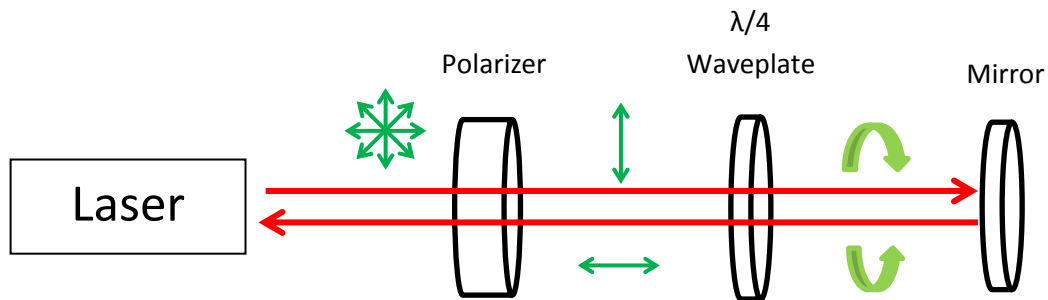


Figure 4.4: Optical isolator comprised of a polarizer and quarter wave-plate.

The polarizer, quarter wave-plate isolator was replaced with a fiber coupled, polarization independent isolator (Of-link, PIISO-1650-S-L-03-FA-FA) to reduce weight in the sensor head and simplify alignment. The fiber coupled isolator typically uses a combination of birefringent beam displacers, faraday rotators and half-wave plates to remove the back-reflected light.

To allow for exponential decay of the cavity resonance with a continuous wave laser, the light needs to be manually ‘chopped’. Mechanical choppers (limited to ~100 kHz) do not chop fast enough to extinguish the beam after resonance occurs (>1 MHz) and would require complicated timing with the acquisition system. Instead, an Acousto Optic Modulator (AOM) is used to switch the beam ‘on’ and ‘off’. When an RF acoustic wave is applied to a crystal, the compressions and rarefactions created by the sound waves cause a periodic change in index of

refraction. The changes in refraction index effectively create a grating through which a beam can be diffracted. Maximum diffraction of the beam occurs when it enters the crystal at the Bragg angle, θ_B defined as

$$\theta_B = \lambda \frac{F}{2V} \quad (4.1)$$

where λ is the laser wavelength, F is the acoustic frequency and V is the acoustic velocity which is typically given by the AOM manufacturer. The diffracted beam exiting the AOM beam is aligned through the sensor optical cavity so that when no there is no RF signal, the beam leaving the crystal is no longer aligned into the optical cavity (Figure 4.5).

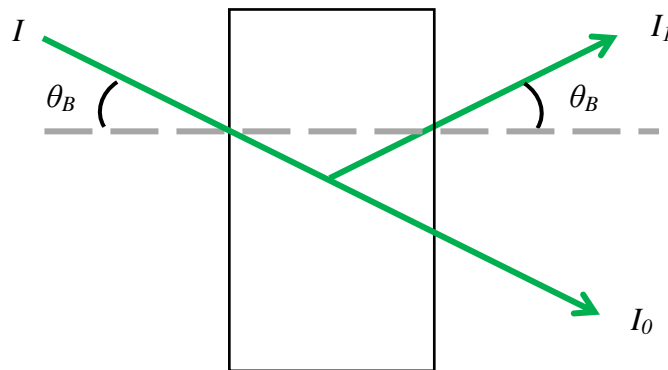


Figure 4.5: Diffraction of beam in AOM occurs when incoming beam, I , enters the crystal at the Bragg angle, θ_B . The diffracted beam, I_1 , will exit the crystal at the same angle, θ_B . I_1 is aligned through the optical cavity, when no RF signal is supplied the beam I_0 leaving the AOM will not enter the optical cavity.

When resonance occurs between the laser beam and the optical cavity, an increase in power is be detected in the output of the cavity and the RF signal to the AOM is turned off, removing the beam from the optical cavity and the resonance decays. This system allows the laser to be switched on and off very quickly; the rise time of the AOM is typically on the order of ns. The first two versions of the sensor used a free space AOM (IntraAction, ACM-402AA23), in Phase-III the AOM was switched to a fiber coupled device (Gooch & Housego, T-M040-

0.5C8J-3-F2S). Fiber coupled AOM's are configured so the incoming beam is always aligned to the Bragg angle, simplifying alignment and reducing optics that could become miss-aligned.

Two steering mirrors (Thorlabs, protected silver) between the collimator lens and the optical cavity are used to align the beam through the optical cavity. Finally, an off-axis parabolic mirror (Thorlabs, protected silver) is used to collect, steer and focus the light exiting the optical cavity into the detector, helping to reduce the overall foot print.

4.2 Data Acquisition and Analysis

The sensor control and analysis is performed through one central acquisition system. A signal is sent to the laser current controller to scan the laser wavelength. A TTL (0, 3.3 V) signal to the AOM driver controls the RF signal sent to the AOM. The high signal, 3.3 V, powers the AOM, directing the laser through the optical cavity. As laser wavelength is scanned, resonance will occur at intervals of the FSR and an increase in power leaving the cavity is detected. A threshold (trigger) detector voltage is set by the user such that when a signal greater than the trigger is detected, the TTL to the AOM driver is switched to 0 V, turning off the RF signal to the AOM and preventing more light from entering the optical cavity. The light built up in the optical cavity will then decay, as a function of the absorption in the optical cavity. The AOM TTL remains at 0V for a pre-set amount of time, nominally 8-10x the decay time (τ) of the cavity after which the TTL returns to 3.3 V and the system waits until the next cavity resonance. This scheme is demonstrated graphically in Figure 4.6.

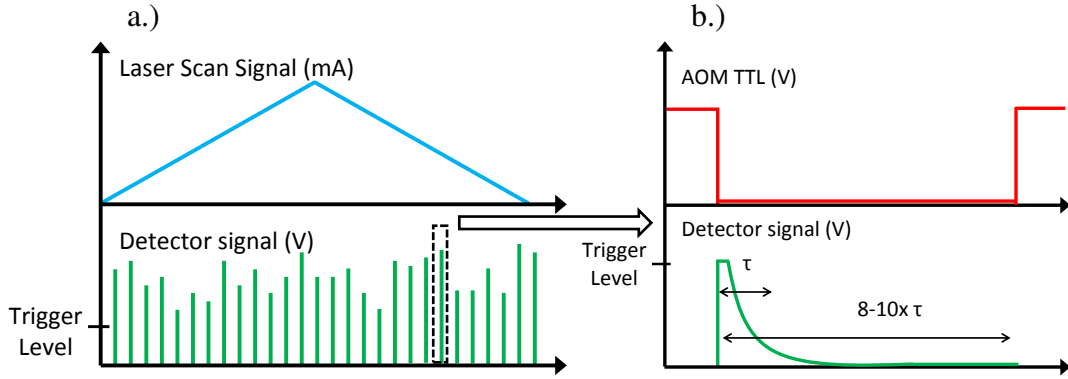


Figure 4.6: Graphical representation of signal inputs (green – detector) and outputs (blue – laser scan signal, red – ATOM TTL) of the sensor. Figure 4.6(a) shows multiple cavity resonances while the laser is being scanned while Figure 4.6(b) is zoomed in on an individual ring down event.

To calculate ring-down times, a baseline signal value is calculated from the end of the signal after $\sim 8-10 \times \tau$ and subtracted from the decay. The signal is fit to an exponential

$$V = e^{-t/\tau} \quad (4.2)$$

where V is the detector signal, t is time, and τ is the ring-down time. To free up computational resources, the data was linearized

$$\log(V) = \log\left(e^{-\frac{t}{\tau}}\right) = -\frac{t}{\tau} \quad (4.3)$$

where τ can be found as the inverse of the slope of a linear fit.

The laser scan speed was typically set between 1-10 Hz. The injection efficiency of the beam into the optical cavity is a function of the laser scan speed (as well as the laser power, mirror reflectivity, cavity length and laser scan extent⁶³) and in general as you increase the scan speed of the laser, the peak intensity of the cavity resonance decreases. The maximum possible scan rate is determined by the ring down time. If the laser was scanned such that the next resonance occurs immediately after the AOM TTL is switched on, the maximum number of ringdowns possible is determined by

$$\text{max \# of } \tau = \frac{1}{8 - 10 * \tau} \quad (4.4)$$

assuming $\tau=30 \mu\text{s}$ (typical for Phase-II and Phase-III), the maximum number of ringdowns would be 3333 – 4166 τ/s . Dividing this number by the number of FSR (ringdowns) in one scan of the feature

$$\text{max laser scan speed} = \frac{\text{max \# of } \tau}{\# \text{ FSR}/\text{scan}} \quad (4.5)$$

And assuming ~50 FSR in one scan, 100 for the full triangle, and the maximum possible scan rate would be 33 – 42 Hz. The scan rate of the laser should be set considering the maximum allowed peak heights vs the capabilities of the data acquisition (DAQ) system. For Phase-III, the sensitivity of the detector increased such that scanning the laser too slow (1 Hz) caused saturation. None of the DAQ systems used with this sensor were able to approach the maximum possible scan. For Phase-I, the laser was typically scanned over 0.48 cm^{-1} at a 1 Hz rate, corresponding to maximum 172 FSRs/s and concentration rates of 0.2 Hz (5 s). The laser was scanned over $\sim 0.5 \text{ cm}^{-1}$ for Phase-II, but scan speed was increased to 4 Hz, with $\sim 400 \text{ tau/s}$ and concentration rates of 1 Hz (1s). Scan speed was further increased to 10 Hz with 600 tau/s , and 1-3 Hz (1-0.3s) concentration rates for Phase-III; scan speed was set faster than needed to obtain 600 tau/s but was chosen so that the strongest resonances could be selected through a higher trigger level.

Two National Instrument LabVIEW DAQ cards were used in sensor Phase-I, (NI PCI-6132 S, NI PCIe-6321) using a windows-based desktop computer and a custom LabVIEW code adapted from a previous HCl CRDS sensor⁴⁶. The limiting factor in Phase-I was determined to be the multi-processing nature of Microsoft Windows, so an embedded DAQ system was

developed by TCB Engineers based on the National Instruments sbRIO-9651. New LabVIEW code was also developed by TCB Engineers which utilized the FPGA and Real-Time components of LabVIEW to maximize sensor performance. In Phase-II, a commercially available carrier board was used to integrate with the sbRIO while a custom carrier board was designed by TCB Engineers for Phase-III to optimize size, weight and power (SWaP), for application in a UAV payload.

Laser wavelength is modulated by adjusting the laser temperature or current but no direct measurement of wavelength is performed for this technique. The relationship between the laser scan signal and wavelength is found using an etalon (Fabry–Pérot interferometer, a transparent media with two reflective surfaces). When the modulated laser is directed through the etalon, positive interference occurs when the laser wavelength proportional to the FSR of the etalon

$$\text{FSR} = 1/2nL \quad (4.6)$$

where n is the index of refraction of the etalon and L is the length of the etalon. This way a relationship between relative laser wavelength and input triangle signal can be determined.

Methane concentration can be calculated in real-time in the DAQ system, but typically the raw ring down measurements were saved and post-processed in Matlab to allow changes in the fit routine.

4.3 Electronics

A small volume of clean air is directed into a positive pressure enclosure near the surface of each HR mirror to prevent degradation in mirror reflectivity due to deposition of aerosol particles. All three versions of the sensor used a small micro-diaphragm pump in combination with a HEPA filter (HC01-5N-B, ETA Filters) to provide the clean air flow. Phase-I and Phase-

II used a pump from Parker (CTS Micro Diaphragm Pump) with flow rate of 0.4 slpm while Phase-III used a Sensidyne (AA120CNSN) pump with a flow rate of 1.8 slpm. In Phase-II and Phase-III an additional 4mm iris was used to isolate the space in front of the HR mirror from the ambient air. When the sensor is not actively powered and the pump is not running, the iris is covered to prevent deposition onto the mirrors.

An InGaS detector with transimpedance amplifier was used to detect the light exiting the cavity. In Phase-I & Phase-II, a Hamamatsu (G8421-03) detector was used with Analog Modules transimpedance amplifier (Model 341). Phase-III used a combined system (Analog modules, 712B-4-DC). The detector used for Phase-I and Phase-II had an extended wavelength range for detection at 1742 nm while Phase-III was optimized for 1651 nm and had a better responsivity. Both detector systems are low noise, high sensitivity, high bandwidth and neither requires active cooling.

The laser temperature is controlled by a thermo-electric cooler (TEC) mounted to the diode and was fixed to keep the laser wavelength centered on the peak of interest. Laser wavelength is modulated around the peak through a modulated current generated from the DAQ system. A triangle wave was used for the laser scan chosen to cover enough of the peak to fit accurately, as no zero baseline is present with open-path sensing. The TEC and current controllers used to modulate the laser should be low noise with bandwidth matched to the system to reduce the noise propagating into the laser wavelength. A large laboratory grade controller (Lightwave, LDC-3714C) was used for both TEC and current control for Phase-I. Smaller, OEM controllers were used for both Phase-II (Wavelength Electronics PTC5K-CH, LDD200-1P) and Phase-III (Meerstetter TEC-1091, Wavelength Electronics, FL500) that could be integrated into a combined electronics package.

4.4 Hardware

The physical construction of the sensor has changed from Phase-I to Phase-III. In Phase-I the optics were mounted to an optical breadboard (2' x 3') mounted to a moveable cart. The associated control electronics and desktop computer were attached to the lower shelf so the entire sensor could be considered mobile. This version of the sensor was successfully driven in the bed of a pickup truck (Figure 4.7), powered by an inverter connected to the vehicle battery, to test the open-path sensor capabilities while mobile. The optics and electronics were covered with cardboard boxes to protect the components and reduce sunlight effects into the detector and the height of the sensor was such that the optical path was above the cab of the vehicle.



Figure 4.7: Sensor Phase-I mounted in bed of pickup truck for preliminary mobile tests.

Phase-II and Phase-III followed a similar design, where the optics and electronics in the sensor head were mounted to custom designed and constructed plates and connected by rods to give stability. For Phase-II, the mount was made from aluminum (6061-T6) with 3 carbon fiber connecting rods, with weight of 5.3 kg and dimensions 39" x 7" x 4.7" (Figure 4.8). During mobile use, the end plates were covered with thin aluminum foil for protection and to reduce

interference from sunlight. The mount was designed to integrate with standard horizontally mounted Thule truck racks, using vibration mounts (McMaster-Carr, 8 lb capacity, 65 A Durometer) to reduce vibrational influence due to roads and vehicle. A companion electronics enclosure (Figure 4.8) was designed for rugged, outdoor use. A commercially available enclosure (Bud Industries, NBF-32326) was used to house the DAQ system, laser controllers, AOM driver, and GPS. A power distribution system was designed and built by TCB Engineers to provide clean, isolated power from a single input (10-30 V, 150 W) and draw power directly from the truck vehicle or battery. The electronics enclosure was designed to safely operate in outdoor conditions in direct sunlight up to 60 C. The overall size of the electronics package was 16"x12"x16" with a total weight of 14.5 kg. The size was dominated by the commercially available IP67 rated enclosure while the weight was dominated by the heat sinks and steel base. The total weight of the electronics alone was 2.2 kg.

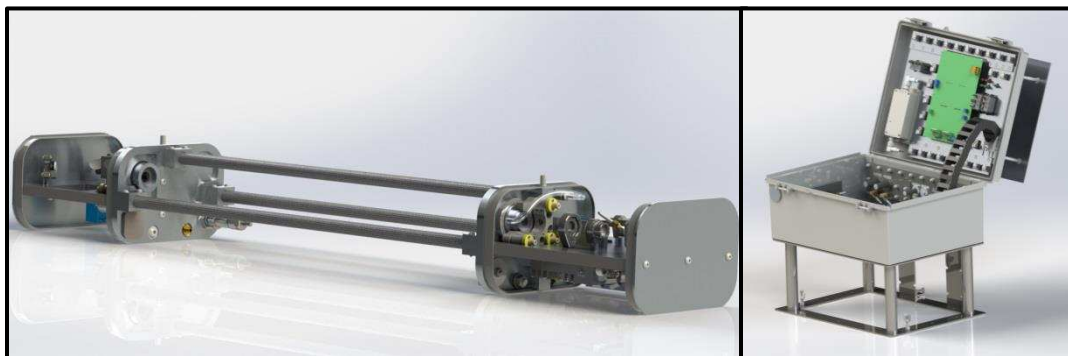


Figure 4.8: Left: Model of Phase-II optical head, dimensions 39" x 7"x4.7" and weight 5.3 kg.
Right: Model of sensor electronics with steel base.

Phase-III was professionally constructed and designed (Czero), and followed a similar design to Phase-II and was constructed out of carbon fiber to reduce the overall weight of the sensor, reduce thermal effects on the alignment and to increase the stability. The size and weight were reduced for simplicity in design as well as to improve the chances of integrating into a

small-payload UAS system. The 3-rod design was changed to a single, much larger (2") tube connecting the two optical ends of the sensor which increased the stability of the sensor while providing a conduit for tubing and wiring, and reducing airflow effects in the optical cavity. Rounded, removable plastic caps enclosed the electronics and optics (Figure 4.9). The footprint of the optical sensor was 7" x 6" x 33" with weight of 2 kg. An enclosure was designed to house the sensor electronics for harsh, outdoor use in a range of temperatures (-40 to + 60 C). To reduce the footprint and weight, a custom board was designed (TCB Engineers) to integrate the sbRIO, laser controllers, power distribution system and laser (5.5" x 3" x 11.5", 1.4 kg). The optical sensor head and electronics enclosure were designed to mount to a truck via Thule racks and a custom designed aluminum mount which used wire-rope isolators to reduce the effects of vibration. The electronics enclosure was designed to run from a variety of power sources, (10-30 V and 25 W) and was typically either powered through a battery (UAS) or through an AC-DC power converter connected to the vehicle inverter. The system was still capable of being powered through the vehicle battery, but the inverter was used as it was simpler the way the laboratory vehicle was setup.

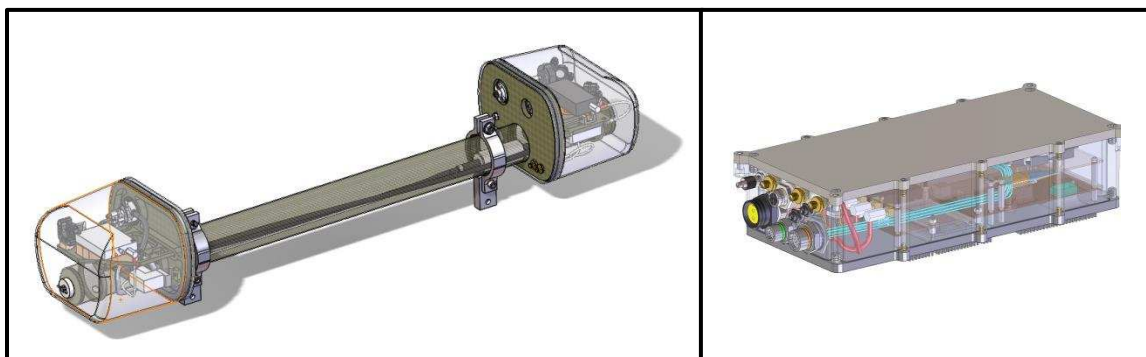


Figure 4.9: Left: Model of Phase-III sensor head, dimensions and weight 2 kg. Right: Electronics enclosure, dimensions and weight 2 kg.

CHAPTER 5:

Laboratory Results

5.1 Mirror Purge

The capability of the mirror purge scheme was assessed for the Phase-I, 1742 nm NIR sensor with several tests including the introduction of high aerosol concentrations (generated by smoking candles) into the optical cavity to simulate extreme outdoor conditions. The aerosol loading was sufficient to cause significant reductions in ring-down times, but after the aerosols dissipated the ring-down times recovered to their earlier value indicating no appreciable change in mirror reflectivity. Longer duration tests of open-path operation were performed for all three versions of the sensor in the laboratory containing nearby vacuum pumps, exhaust, and sooty combustion burners, as well as outdoors of the lab in Fort Collins, CO within 50 m of a heavily used street. No significant loss of mirror reflectivity was noted after extensive driving of Phase-II in rural Colorado or Phase-III in rural Colorado and Pennsylvania over 100's of hours of year round outdoor use.

Effects from the vibration of the pump were sometimes seen in the alignment of the sensor. If the vibrations are carried from the pump into the sensor mount, and specifically into the HR cavity mirror mounts, it can cause the mirrors to 'jitter', effectively changing the cavity length, and if close to the frequency of the laser scan, broaden the effective FSR of the cavity. This can induce noise in the mode match peaks of the sensor and reduce the magnitude of the resonance between the laser and the cavity. In Phase-I, the pump was kept far away from the optical components and this was not an issue, but for both Phase-II and Phase-III the pump was located in the detector side of the optical sensor and effects could sometimes be seen. In Phase-II, vibrations were reduced, but not eliminated, by enclosing the pump in foam insulation. In

Phase-III, a compact wire-rope vibration isolator was used to mount the pump to the sensor head (Enidine, CR1-300 D) which was sufficient to eliminate vibration noise when other components in the compact sensor did not touch the pump.

5.2 Aerosol Noise in Signal

Ring-down signals for open-path CRDS can be influenced by the optical extinction of aerosol particles in the laser beam. Pettersson et al.⁶⁴ considered the optical extinction for three different aerosol distributions corresponding to a range of clean and polluted air cases and found extinction coefficients in the range of $\sim 10^{-8}$ - 10^{-7} cm^{-1} (for 532 nm light) which are readily detected by our CRDS instrument. Pettersson also discussed how, even for a fixed size distribution, statistical variations of the number of particles within the cavity beam lead to fluctuations in the ring-down times. The fluctuations are dominated by stochastic variation in the number of large particles (~ 1 - 10 μm diameter) present in the beam volume^{50,65}.

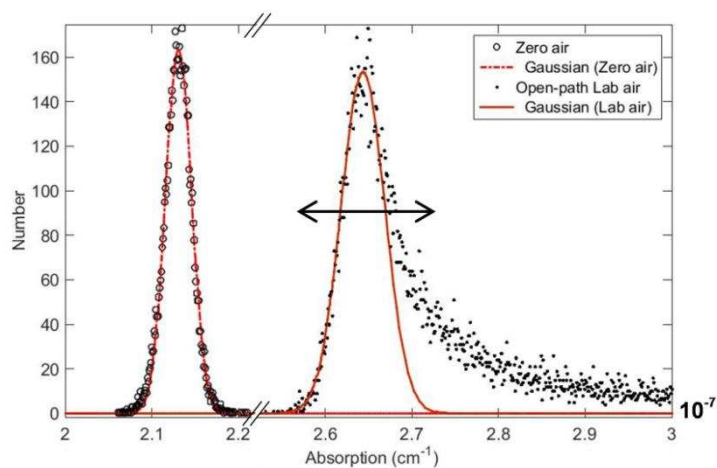


Figure 5.1: Histogram of CRDS absorption measurements for closed-cell measurement of zero air with no particles and open-path measurement of ambient laboratory air. Arrow indicates range of points within 50%, $\pm 0.7 \times 10^{-8}$ cm^{-1} filter.

Figure 5.1 demonstrates the effects of aerosol extinction through histograms of the 1742 nm (Phase-I) CRDS. It should be noted that although graphs of the methane spectra presented

here are labeled as absorption as is standard for gas spectroscopy, noise due to aerosols is due to total light extinction from absorption and scattering of the particles. Absorption measurements were obtained from single-shot ring-down acquisitions for zero-air in closed-cell configuration and open-path measurements of laboratory air. Measurements were taken by scanning the laser over a narrow region (~ 1 FSR) selected to be away from absorption line. For the zero-air case, the histogram is well described by a Gaussian whose width is indicative of the measurement spread of the laser sensor, i.e. effects of detector noise, fitting error, laser Phase noise etc. The open-path distribution can be considered as the sum of a similar Gaussian plus a high absorption tail due to temporally fluctuating aerosols in the beam. The center location of the Gaussian for the open-path case is different than for zero air, attributed to a combination of weak absorption from the spectral wings of nearby water lines as well as from small particles (diameter $< \sim 1 \mu\text{m}$) that are present with relatively stable numbers within the cavity beam. The higher absorption tail reflects the extinction due to larger particles (diameter $> \sim 1 \mu\text{m}$) that provide stronger absorption and are present with smaller fluctuating numbers inside the beam⁶⁴. Comparison of the areas in the Gaussian and tail components of the open-path histogram shows that approximately 60% of the ring-down acquisitions were influenced by the fluctuating super-micron aerosols. Open-air histograms obtained from different measurements change somewhat due to varying particle loading, but the distribution shown in Figure 5.1 is reasonably representative for several cases we have studied within our laboratory outdoor air on the roof of the same laboratory located approximately 50 m from a major urban road.

5.3 Numerical filters to remove aerosol signals

Figure 5.2 shows raw absorption (red points) for open-path CRDS of ambient air in the laboratory from a series of ring-down signals for approximately 60 s. The methane absorption

features Figure 3.2 are visible along with noise, probably due to aerosol particles as discussed above. Determining the methane concentration requires fitting the data with the synthetic spectrum given in Eqn (3.10).

The distributions of ring-down times from Figure 5.1 suggested possible strategies to filter the data to mitigate the aerosol effects. The first filtering method is based upon preserving or rejecting absorption values by first considering a series of frequency intervals, “bins”, along the laser frequency axis. Within each bin, the decision to preserve or reject each data point is based on considering a specified absorption tolerance and the “mode” of the absorption values in the given bin. Because aerosol induced fluctuations cause an increase in absorption, points that exceed the mode by more than the tolerance are rejected, while all other points in the bin are preserved for use in the final concentration spectral fit (Eqn (3.10)). To determine the mode in a given bin, a subset of the points having the lowest absorption values, for example from a subset comprised of the 50% of the lowest points is examined. The mode is then found by rounding the absorptions to 10^{-9} cm^{-1} and finding the value that occurs most frequently. The same tolerance is used for all bins and is set a priori based on the instrumental precision. For the 1742 nm sensor, a tolerance of $0.7 \times 10^{-8} \text{ cm}^{-1}$ was used, based on the half-width of the Gaussian of the open-path histogram (Figure 5.1). The preserved points match reasonably well with the Gaussian envelope and constitute ~50% of the starting number of points in each bin. The black points in Figure 5.2 show the data preserved by this frequency bin filter configuration, with the cyan curve being the spectral fit to the preserved points. In this case 42 frequency bins were used – the needed number of bins can be determined by simulation and should be matched to experimental conditions (e.g. 42 bins corresponds to ~2 FSR per bin).

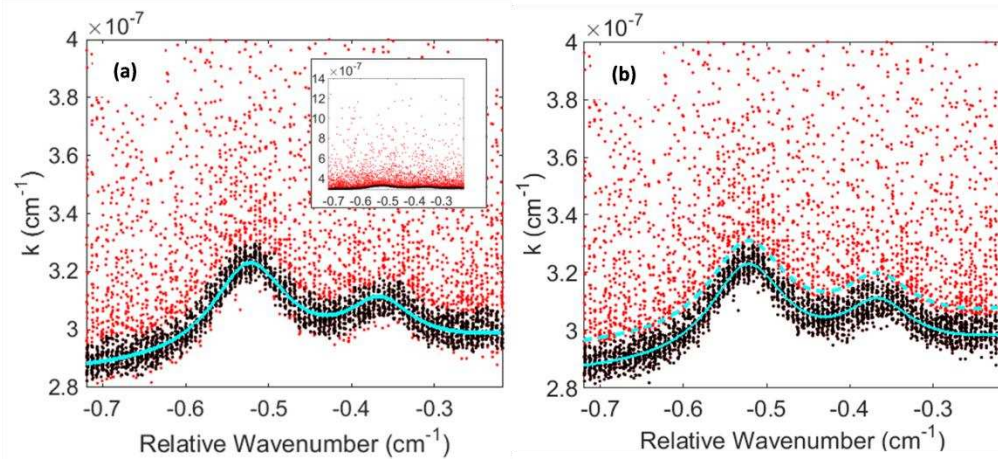


Figure 5.2: Methane absorption spectrum of ambient laboratory air measured by the open-path 1742 nm CRDS. Raw data shown with red points, data preserved by filter shown with black points, final spectral fit shown with cyan curve. Inset in Figure 5.2(a) is more zoomed out to show larger fluctuations. Application of frequency bin filter shown in Figure 5.2(a), global iterative filter in Figure 5.2(b). The first iterative fit is shown with the dashed cyan curve. Intermediate fits not shown.

A shortcoming of the frequency bin filter is that it does not consider known information about the overall spectral shape along the frequency axis. The second filter method iteratively identifies outliers and fits the spectrum in a more global manner. First, all ring-down points are fit with the synthetic spectrum. A tolerance band is again defined, similar to the frequency bin filter. Points that are larger than the fit by more than the tolerance are identified as outliers and discarded. The remaining data is re-fitted, and the method is iteratively repeated until a desired degree of convergence is reached or a maximum number of iterations has been reached. Figure 5.2(b) shows use of the global iterative filter to the same data as was used for the frequency bin filter in Figure 5.2(a). In this case the filter used a tolerance of $0.7 \times 10^{-8} \text{ cm}^{-1}$ and converged after 8 iterations where convergence was defined as standard deviation < 0.01 ppmv between the last four concentration fit values. The two filter methods were applied to 30 min of open-air laboratory data with 5 s increments resulting in consistent mean concentrations of 2.94 ± 0.15 ppmv for both the frequency bin and global iterative methods.

The filters were developed for the Phase-I, 1742 nm sensor, and the exact parameters used varied with details of the setup and region of study. Although methane absorption was stronger for the region studied at 1651 nm, aerosols were still an issue and the filter was still necessary. For ease of computing, the frequency bin method was adopted for Phase-II and Phase-III analysis, with some small adjustments to the parameters of the filter. The scan region for 1651 nm is a similar width and 42 bins was still applicable, while the stronger overall absorption necessitated an increase in the tolerance of $k=0.3 \text{ E-6 cm}^{-1}$ while rounding the data to the nearest 10^{-8} cm^{-1} . To note: The tolerance needed for the data is subject to change depending on the aerosol sample measured and it was found that for some outdoor conditions (such as mist, fog, vehicle exhaust), this tolerance needed to be wider by a factor of 2-5 while for some extreme exhaust conditions (idling behind a vehicle at a stoplight, large diesel trucks) the loading due to dust was too extreme for any aerosol filter and the data simply appears as noise with no visible CH_4 spectra.

5.4 Sensor Accuracy

Although CRDS is an absolute measurement and does not require calibration, accuracy and the suitability of the synthetic spectrum were tested for the 1742 nm sensor by supplying known concentrations of methane gas in a closed-path configuration. Ultra-pure zero-air was mixed with methane gas from a reference cylinder (250 ppmv) and passed through the cell at 0.84 atm and 296 K. Measurement results are shown in Figure 5.3 and demonstrate good agreement, within experimental uncertainty, between measured and expected concentrations. Error bars for expected concentrations are due to propagation of the 2% uncertainty in the calibration source and 4% of full scale uncertainty of the flow sensor (0-5 LPM). Errors bars on

the measured concentration are taken as the 2 s standard deviation in the measured values during the 10 min averaging time and are negligibly small on this scale.

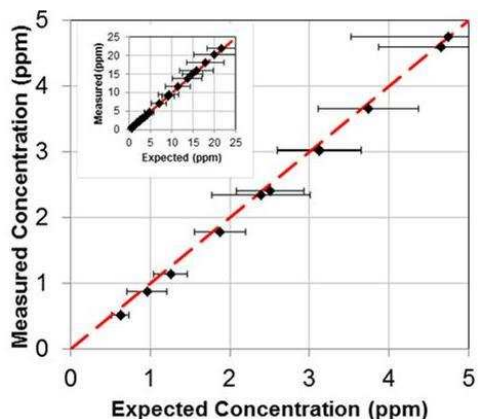


Figure 5.3: Methane concentrations recorded in closed-path configuration.

Accuracy tests were not performed for either of the 1651 nm versions of the sensor as no closed cell configuration was designed for the compact mounts, but confirmation of accuracy was determined through mobile comparisons of ambient measurements with a commercially available Picarro sensor (G2203).

5.5 Sensitivity

Allan variance studies of the absorption measurements were performed to characterize sensor precision; Allan variance is a statistical analysis used to measure the stability of a measurement. Figure 5.4 shows results for the 1742 nm sensor, using the modified method outlined by Huang and Lehmann¹⁷. The laser frequency was scanned over a narrow region selected to be representative of the absorption baseline. Results are shown for three cases: closed-path with ultra-pure zero-air, ambient air measured open-path in the lab with particles present, and the ambient case but with application of a software filter described below (frequency bin method). As expected, closed-path gives the best stability with the lowest Allan deviations with a noise equivalent absorption (NEA) of $2.4 \times 10^{-10} \text{ cm}^{-1} \text{ Hz}^{-1/2}$ which compares

favorably to other non-locked, near-infrared CRDS instruments^{45,66}. The HCl CRDS sensor that the Phase-I 1742 nm sensor was modified from, found optical sensitivity of $7.0 \times 10^{-11} \text{ cm}^{-1} \text{ Hz}^{1/2}$, much better than our closed-path, but similar sensitivity could be obtained again when operating the open-path sensor with similar scan and trigger level conditions.

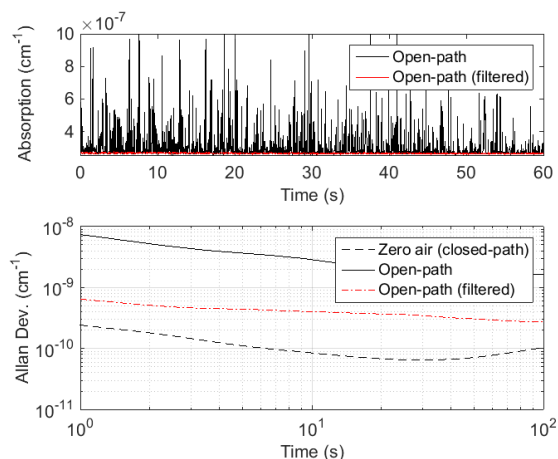


Figure 5.4: Allan variance of absorption values for closed-path (zero- air), open-path ambient air, and open-path ambient air with software filter.

Increased signal fluctuations for open-path operation without software filtering degraded the deviation by a factor of ~ 30 . A variation of the frequency bin filter provided substantial improvement, yielding Allan deviations within a factor of 3 of the zero-air case for most time durations corresponding to $NEA \sim 6.0 \times 10^{-10} \text{ cm}^{-1} \text{ Hz}^{-1/2}$. The filtered Allan deviation yields a theoretical detection limit of ~ 50 ppbv for the specific NIR lines used, assuming the same NEA for the 1651 nm peak, sensitivity would improve to ~ 2 ppbv. For Figure 5.4, the frequency bin filter uses a tolerance of $0.7 \times 10^{-8} \text{ cm}^{-1}$ and 50% of points in a bin for mode determination.

Allan variance for the 1651 nm sensors was determined through analysis of concentration rather than extrapolating sensitivity from a single measurement of absorption. Measurements of the Allan variance for a variety of conditions were calculated and reported at 1 s. Allan variance was determined for zero air, concentrations of methane gas generated by mixing a 250 ppmv

bottle of methane with zero air at different ratios, as well as room air with an open path and almost closed path. It can be seen that Allan variance results for the sensor were broadly independent of air sample, while showing a clear trend with concentration; i.e. as concentration increases, the sensitivity of the measurement decreases. For typical background concentrations of ~1.8 ppmv the sensor reports a sensitivity of ~14 ppbv at 1 s. It should be noted that room air measurements in the CSU laboratory are higher than typical background values, ~2-3 ppmv, likely due to the location of our lab in a facility with a number of engines and combustion experiments that tend to increase the indoor concentration above background levels.

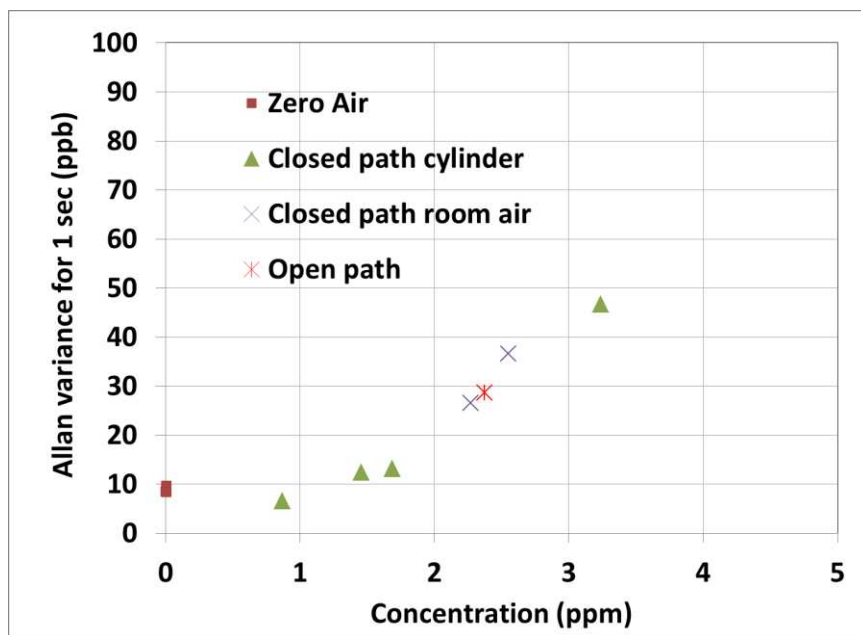


Figure 5.5: Allan variance for 1651 nm Phase-II sensor for simulated concentration, zero air, closed path cylinder air, closed path room and and open path room air data.

Open-path Allan variance studies were performed for Phase-III of the sensor, indicating an Allan variance of <10 ppbv at 1 s (Figure 5.6).

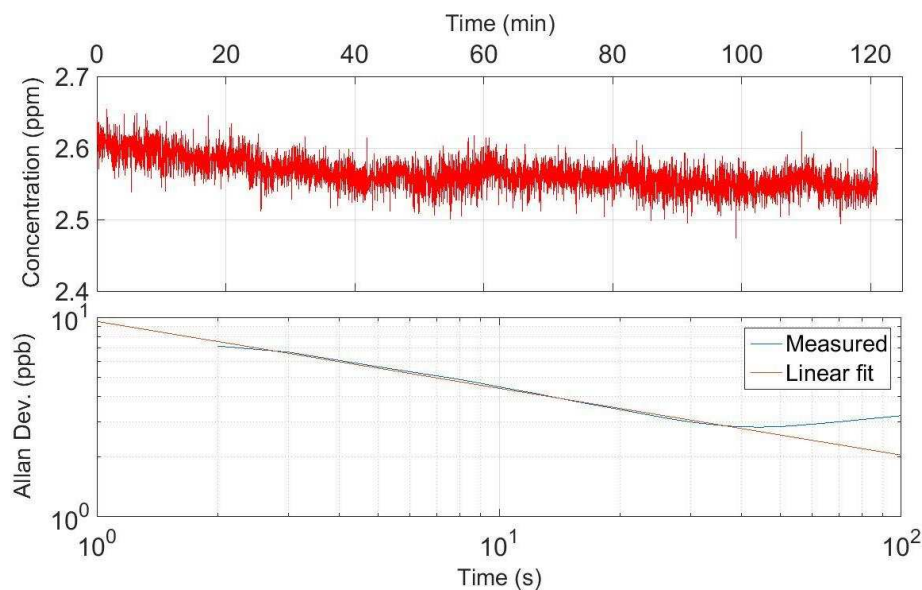


Figure 5.6: Allan Variance study for Phase-III sensor in CSU laboratory, deviation of 9.6 ppbv found for 1 s average.

5.6 Indoor Picarro comparison

Delivering known concentrations to the sensor in open-path configuration is experimentally difficult. To validate sensor readings in the open-path configuration, comparison was performed against a commercial CRDS methane sensor (Picarro model G2203⁵⁴) during a controlled release of methane gas. The setup for the experiment is shown in Figure 5.7(a). The two sensors were co-located in an old aircraft hangar (~21 m by ~23 m) at Christman Field in western Fort Collins, partially open to the outdoors. The methane was released from a gas cylinder with flow rate < 0.3 g/s positioned ~15 m from the two sensors and fans were used to blow the gas towards the sensors to simulate a uniform plume. The inlet of the commercial sensor was modified by replacing the single inlet port (6.2 mm inner diameter) with a custom eight-port inlet to more representatively sample along the 90 cm cavity of the open-path sensor. Figure 5.7(b) shows data collected by the open-path sensor and the commercial sensor using the multi-port inlet. The commercial sensor was operated at 1 Hz and adjacent averaging was used to

adjust the time response to 0.2 Hz to match the open-path sensor which filtered and fit a spectrum every 5 seconds. The global iterative filter described above was used on the open-path data, with tolerance of $0.7 \times 10^{-8} \text{ cm}^{-1}$. A linear fit between concentrations from the open-path and commercial closed-path sensors showed excellent agreement with slope of 1.005 ± 0.002 ($R^2=0.977$).

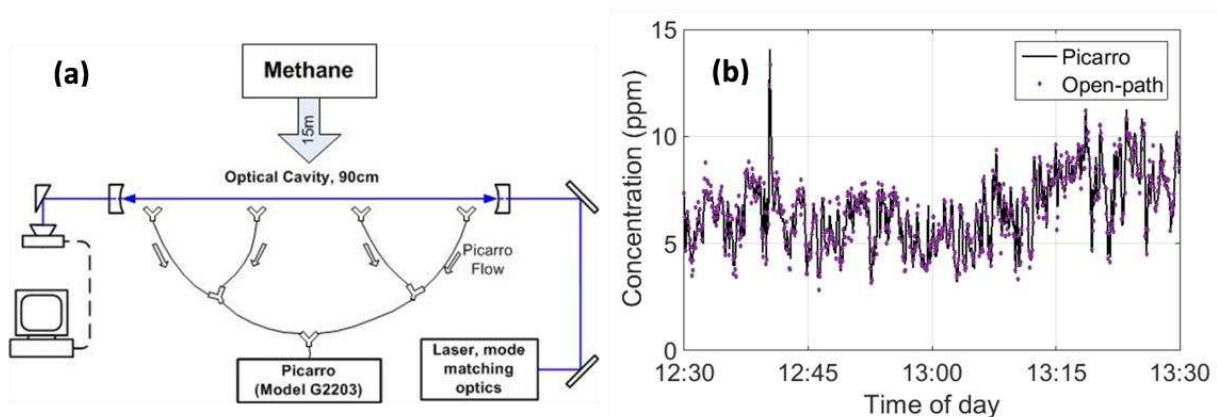


Figure 5.7: Experiment setup for methane comparison (a) between open-path instrument and commercial closed-path instrument (Picarro, G2203). Results of comparison measurements shown in (b), averaged to 5-seconds.

The small discrepancies between the open-path and commercial instrument concentrations are partly due to spatial variations in the plume that is sampled differently by the two sensors. Switching the commercial sensor to the 8-inlet multiport significantly improved agreement with the open-path sensor, as compared to initial measurements using the single point inlet. The discrepancies may also be due to limitations in the response of the commercial closed path analyzer. A similar comparison of ammonia plume measurements between open-path laser absorption (WMS) and a commercial closed-path CRDS analyzer⁶⁷ showed that the open-path analyzer tended to capture more dynamic behavior while the closed-path analyzer showed a flatter response (even when the data were averaged to give matching time steps).

CHAPTER 6:

Mobile Measurements

6.1 Platteville, CO

The Phase-II sensor and the Picarro (G2203) were co-located on the Powerhouse Ford Expedition for measurements from oil and gas field in Platteville, CO in January 2017. Platteville was chosen for its close proximity to the University (not a lot of planning was necessary to take measurements and it was simple to drive back several times) and the density of the facilities in the area as shown in Figure 6.1.

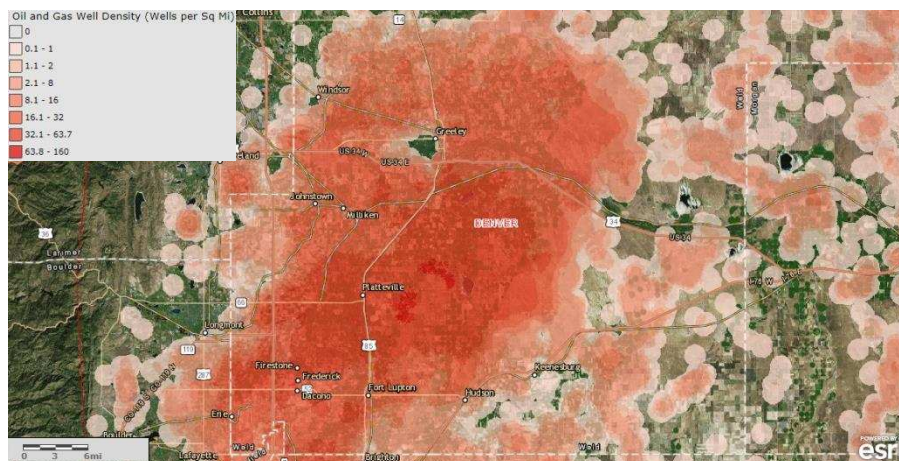


Figure 6.1: Map showing oil & gas well density for northern Colorado,

The purpose of the study was to verify the open-path sensor against the Picarro sensor during mobile measurements of oil and gas leaks. The open-path sensor was mounted to the roof of the vehicle so the open-path sensing region would be free from interference from airflow from the truck, and the sensor was powered directly by the vehicle battery. The Picarro sensor was located in the rear of the vehicle along with its custom designed battery system⁶⁸, with the inlet directed to the roof to co-locate measurements with the open-path sensor. The multi-port inlet

was again used for the Picarro to more accurately mimic the 60 cm sample cavity of the open-path sensor (Figure 6.2).

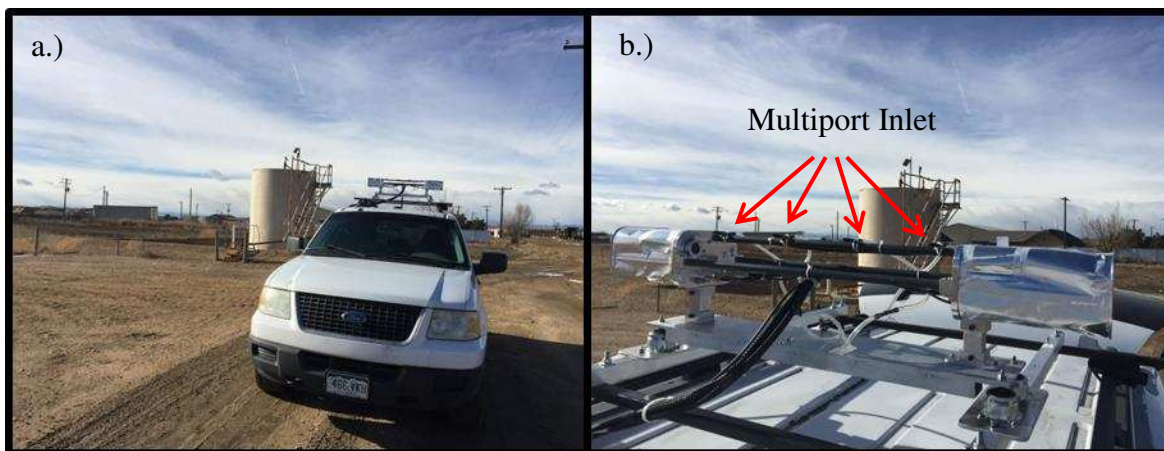


Figure 6.2: 1651nm open-path CRDS sensor (Phase-II) mounted to roof of Ford Expedition in Platteville, CO January 2017. Figure 6.2(a): Open-path sensor placement on roof of vehicle. Figure 6.2(b): Multiport inlet for Picarro along cavity of open-path CRDS sensor.

Data taken on 1/10/17 is shown in Figure 6.3 for both sensors. Data was collected while driving from Fort Collins, CO to Platteville Colorado until just after noon when the open-path sensor stopped working. This was the first test where the sensor was used outdoors in colder (< 23 C,) temperatures and the sensor alignment was found to have a large dependence on temperature. Thus, the vehicle was stopped periodically to adjust alignment while still mounted on the roof to bring back performance. It can be seen in Figure 6.3 that there were periods where the open-path and Picarro sensors had good agreement, and large sections where the open-path data was very noisy. Ingestion rate (# of ring-downs measured per second, $> 175/s$) and R^2 (> 0.9) of the spectral fit were used to filter out periods where the open-path sensor was not working well. Comparing a 1-1 of the open-path and Picarro data averaged to the same 5 s sampling rate gave slope = 0.88, $R^2 = 0.86$ and SSE = 10.74 prior to filtering the open-path data and slope = 0.89, $R^2 = 0.95$ and SSE = 3.42 after filtering (Figure 6.4).

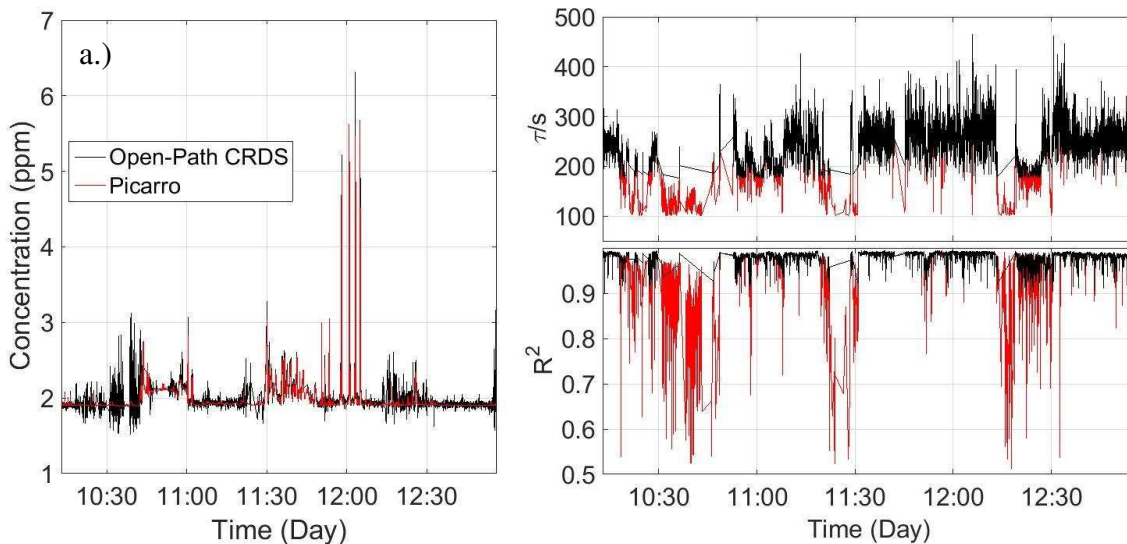


Figure 6.3: Open-path CRDS data from 1/10/17 driving from Fort Collins to Platteville, CO. Figure 6.3(a): Timeline of open-path (black) and Picarro (red) data. Figure 6.3(b): Parameters used to filter open-path data, Top: Ingestion Rate ($> 175 \tau/s$), Bottom: R^2 of spectral fit (> 0.9).

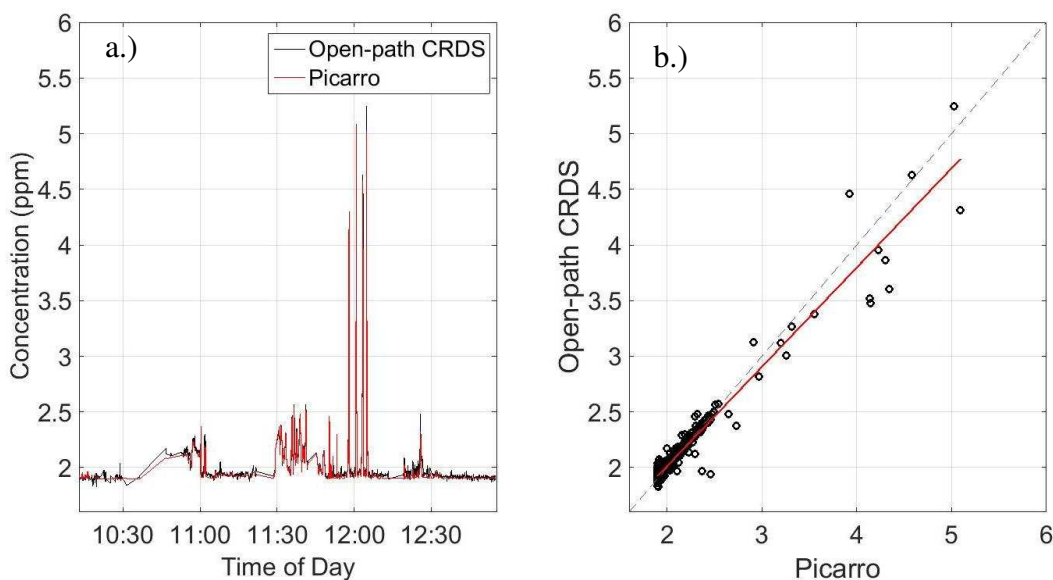


Figure 6.4: 1-1 comparison of open-path and Picarro data after open-path data was filtered, giving slope = 0.89, $R^2 = 0.95$ and SSE = 3.4.

The sensors compared similarly for data taken on 1/12/17, although ingestion rates were much lower ($\sim 100\text{-}300 \tau/s$) likely due to colder ($\sim 3 \text{ C}$) conditions. After filtering for $R^2 > 0.9$, 1-

1 comparison between the open-path and Picarro data was fairly poor until concentrations were limited (<6 ppmv) and slope = 0.8, $R^2 = 0.85$, SSE = 23.46 were found.

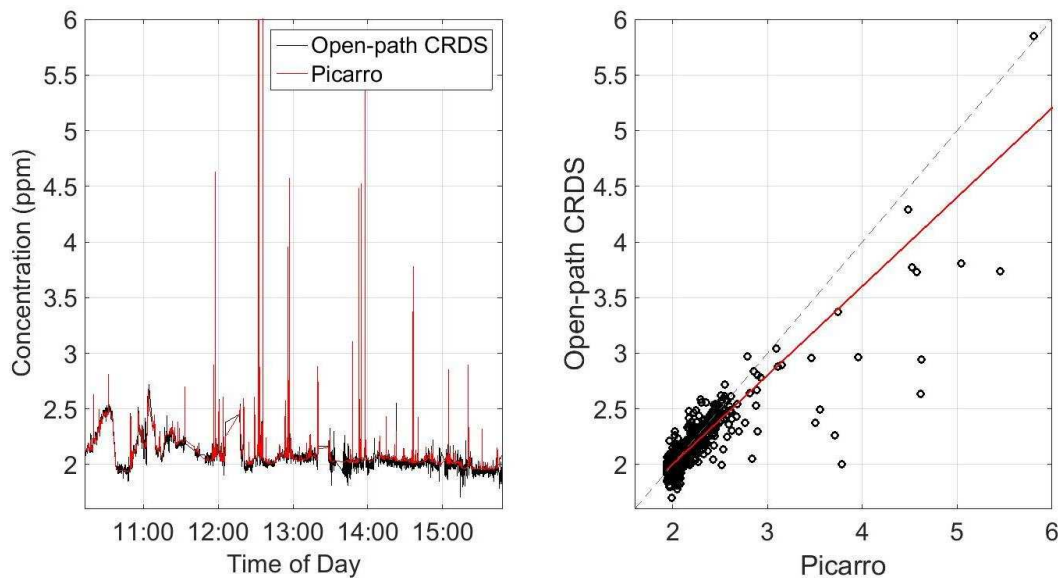


Figure 6.5: 1-1 Comparison of open-path and Picarro data for Platteville, CO on 1/12/17. Colder temperatures and higher concentrations led to worse comparison (slope = 0.8, $R^2 = 0.85$, SSE = 23.46).

Figure 6.6 shows repeated measurements of a facility in Platteville, where methane could likely be attributed on both 1/10/17 and 1/12/17. On 1/10/17, winds were fairly strong (~15 mph) from the west, producing a good signal on the road just on the east side of the facility. On 1/12/17, weaker winds were from the NE/ NNE (~6 mph), with a signal probably measured from the facility with peaks ~3 ppmv. A larger (6 ppmv) signal was measured further to the west but based on the wind conditions is most likely due to another well pad adjacent to the road. This work demonstrated that signals from small and large facilities can depend on availability of nearby roads and local wind conditions.

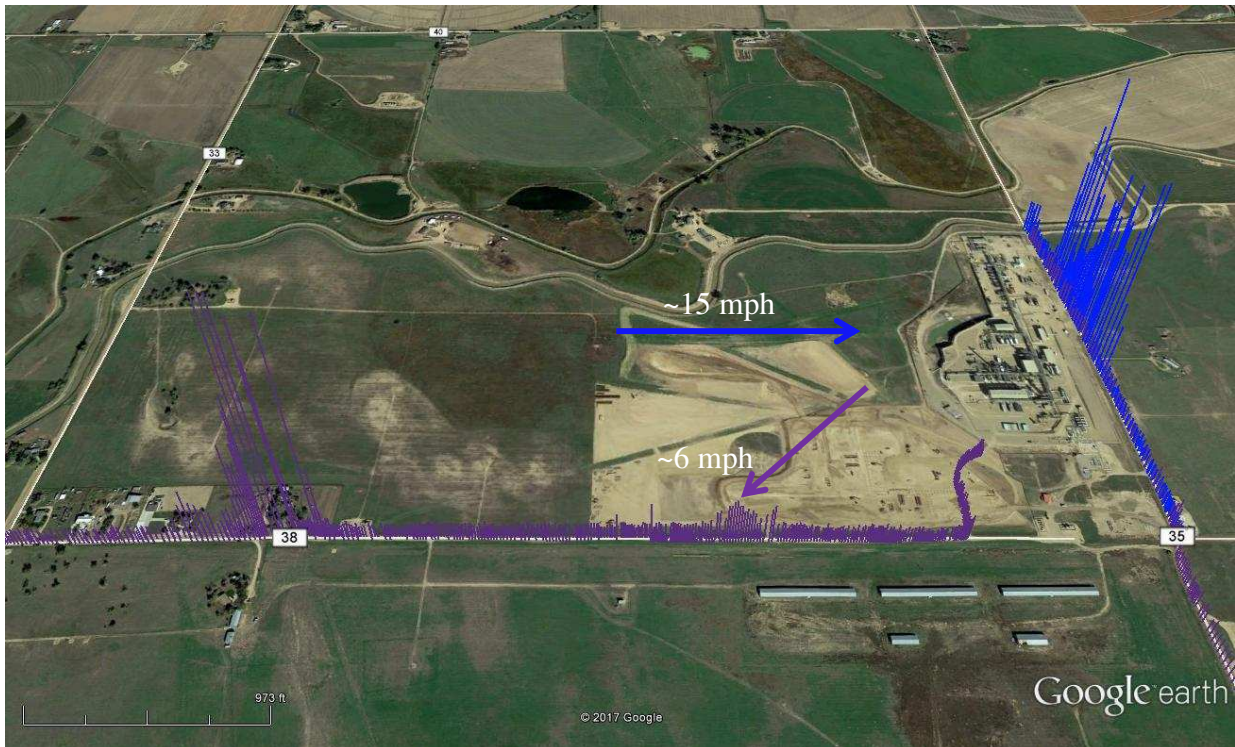


Figure 6.6: Open-path CRDS data measured on 1/10/17 (blue) and 1/12/17 (purple) of the same facility in Platteville, CO, maximum concentration $[\text{CH}_4] = 6.2 \text{ ppmv}$.

6.2 METEC

Our second 1651 nm mobile sensor, Phase-III, was again mounted to the roof of the Powerhouse Expedition to measure controlled releases of methane gas at the ARPA-E's (Advanced Research Projects Agency-Energy's) MONITOR (Methane Observation Networks with Innovative Technology to Obtain Reductions) METEC (Methane Emissions Technology Evaluation Center) site located next to the Foothills in Fort Collins Colorado. The focus of the METEC site is to simulate releases from natural gas facilities so that new technologies and measurement techniques can be evaluated. As part of CSU, and to help test the facility while it was still being setup, we were allowed to test on site on a number of days, while adjusting the leak flow rate. The leak location was the same for all of our testing, at Pad 1 in the south-east corner of the facility. For each leak rate, the vehicle was driven around the smaller and larger

loops up to 10x each to get a better idea of where the plume was, drive speeds were limited to <10 mph for safety reasons while at the site. For scale, the smaller loop is 44 m north of the release and the larger loop is 110 m north of the release.

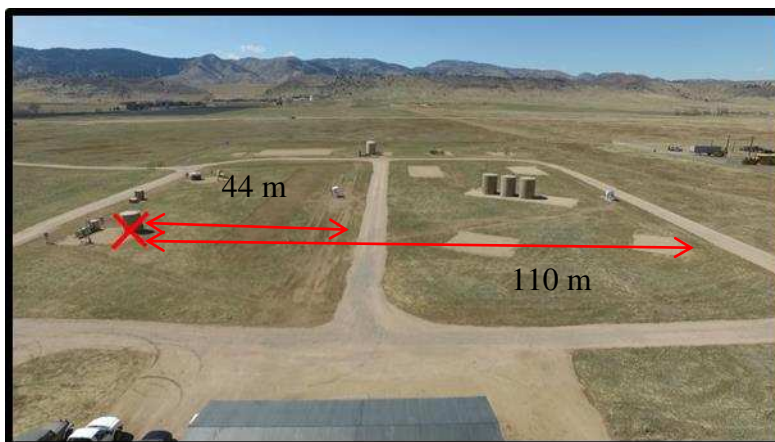


Figure 6.7: Aerial view of the METEC site with an x indicating the location of the leak release during sensor tests. The site is controlled through a trailer located on the east side of the site (bottom of the photo).

Data was taken at METEC first with just the open-path CRDS sensor on 8/30/17 at 6 flow rates (18.57, 45.03, 62.63, 78.76, 96.25 and 121.79 scfh). Raw ringdown times were collected so the data could be post processed at different concentration rates (1 Hz, 3 Hz) to investigate the effect sampling rate had on leak determination. GPS data, 1 Hz concentration measurements and local 5 min average met data obtained from the nearby CoAgMet (COLORADO Agricultural Meteorological nETwork) station, located 270 m south east of METEC, were used by collaborators at Cornell University (John Alberton's group, Civil and Environmental Engineering) to calculate leak rates. Using Bayesian inference⁶⁹, a recursive method determines a probability function density function of likely leak rates based on each pass and the estimated leak rate and its uncertainty are determined. Preliminary results are shown in **Error! Reference source not found.** for the 6 leak rates, showing agreement <20% for all but the lowest flow rate. Results for the lowest flow right might have been skewed as work was being done onsite at this

time on some of the other well pads and might have caused a falsely elevated signal. Winds were fairly calm this day, ranging from 1-4.5 mph, decreasing from a maximum during the earlier tests, and out of the south east to the east by the end of sampling.

Table 6-1: Leaks rates (Q_e) calculated by Dr. Xiaochi Zho compared to known leak rates (Q_0). This work was presented in a poster at AGU in New Orleans, LA 2017 by Dr. Xiaochi Zho

Exp. #	$Q_0 \pm 2\sigma_Q^0$ (scfh)	$Q_e \pm 2\sigma_Q^e$ (scfh)	$(Q_e - Q_0)/Q_0$ (%)
1	18.57 ± 1.79	40.16 ± 6.18	116.26
2	45.03 ± 4.71	40.32 ± 4.48	-10.5
3	62.53 ± 3.00	69.64 ± 8.41	11.37
4	78.76 ± 2.53	69.75 ± 7.28	-11.44
5	96.25 ± 2.69	93.37 ± 10.68	-2.99
6	121.79 ± 3.12	141.66 ± 20.52	16.31

For constant leak rates, the plume that is measured by a mobile sensor can change, depending on the local wind conditions, shifting in location, 2-d plume shape and the maximum concentration values measured (Figure 6.8, Figure 6.9). Instead of looking at just the individual concentration measurement values as the vehicle passes the plume, the concentration is integrated over the width of the plume to determine the total methane in units of ppmv-m, i.e. concentration integrated over the drive length after the background is subtracted. Integrated plume measurements can also be to identify differences in analyzing our data at 1 or 3 Hz rates. For this analysis, a single pass was determined as the data obtained between consecutive passes of the control trailer. A background concentration value was determined by taking the average of the first and last few measurements for each loop and subtracting from the data before integration was performed. Criteria were used to determine whether a plume actually occurred, given by two consecutive measurements where $[\text{CH}_4] > [\text{CH}_4]_{\text{background}} + 0.2$ ppmv. Latitude and

Longitude measurements were converted to meters and the distance was calculated as the hypotenuse of the distance travelled for each lat/long coordinate.

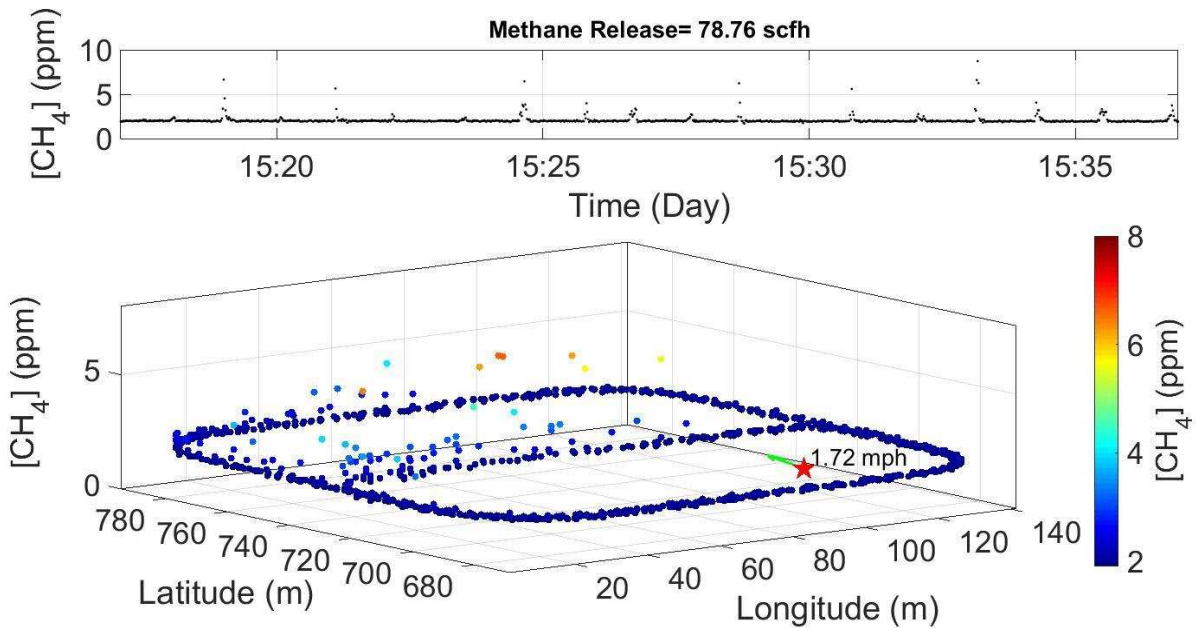


Figure 6.8: Top: Time series of 1 Hz methane concentration measured for a leak rate of 78.76 scfh. Bottom: Composite graph of all loops showing the elevated concentration (both color and height indicate methane concentration). Star in the bottom right indicates the location of the leak and the green arrow indicates the direction and magnitude of local wind.

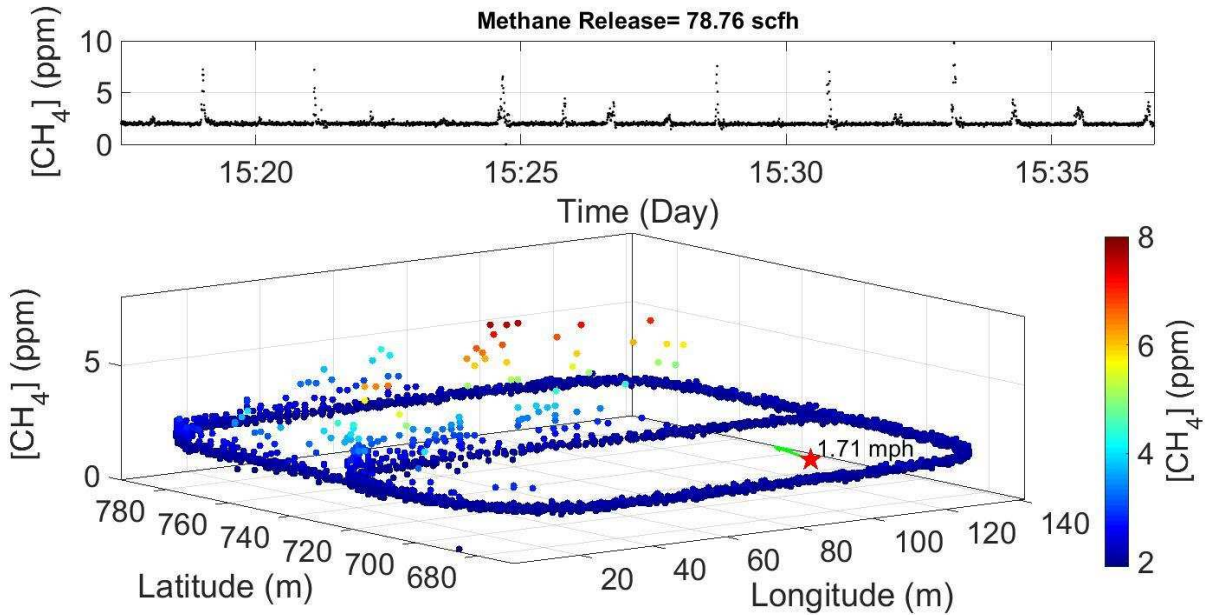


Figure 6.9: Top: Time series of 3 Hz methane concentration measured for a leak rate of 78.76 scfh. Bottom: Composite graph of all loops showing the elevated concentration (both color and height indicate methane concentration). Star in the bottom right indicates the location of the leak and the green arrow indicates the average direction and magnitude of local wind.

Comparison of 1 and 3 Hz analyzed data shows good agreement (Figure 6.10) with a $R^2 = 0.95$, while the slope = 1.3 indicates that the 3 Hz leads to higher concentration measurements. Looking at the values individually based on leak rate, it is evident that the 1 and 3 Hz analysis show the best agreement for lower flow rates, and lower concentration values, suggesting that as the leak rates increased, and the plumes become larger the measured concentration was changing more rapidly and our 1Hz analysis was inclined towards underestimation. It is also interesting to note that, as expected, when the passes are separated into the small (closer) and large (further away) loops, the small loops show higher values than the large loops, although both recorded small plumes for some passes (Figure 6.11); apart from 96.25 scfh where both large and small loops appeared to measure a range of values.

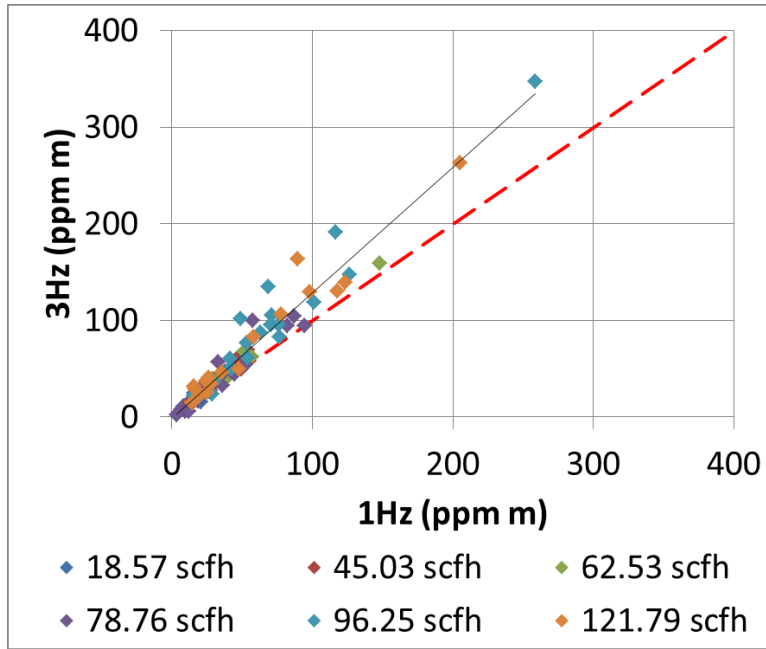


Figure 6.10: Integrated plume measurements for 8/30/17 at METEC for 6 flow rates, comparing 1 Hz and 3 HZ analysis.

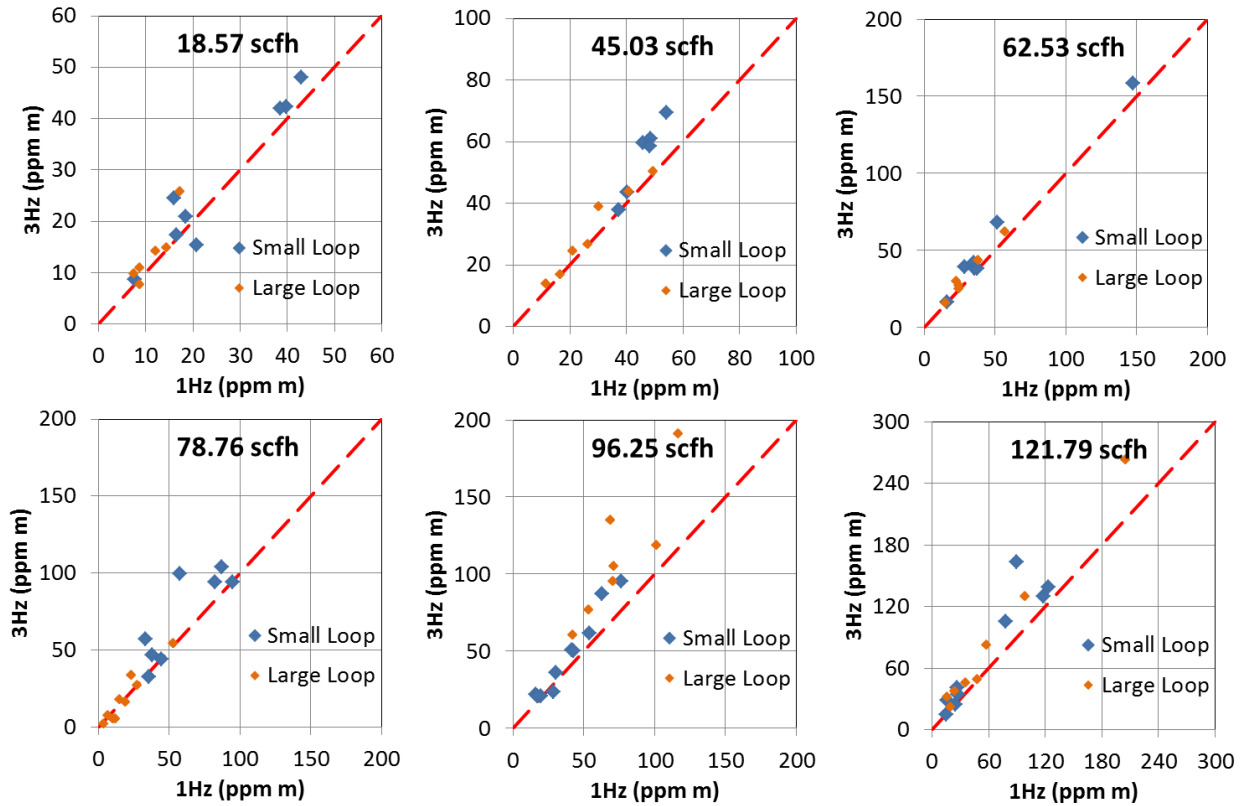


Figure 6.11: Integrated plume measurements for 8/30/17 separated out by flow rate and loop around leak site.

The slope of the data in Figure 6.10 indicated that the 3 Hz analyzed data reported on average 30% higher than 1 Hz data. The reason for this can be seen by looking at a specific case for 96 scfh, where the 3 Hz data reported 101 ppmv-m while 1 Hz reported only 48 ppmv-m. As can be seen in Figure 6.12, at 1 Hz the maximum concentration reported was ~6 ppmv while it was nearly doubled at ~11 ppmv for 3 Hz rate.

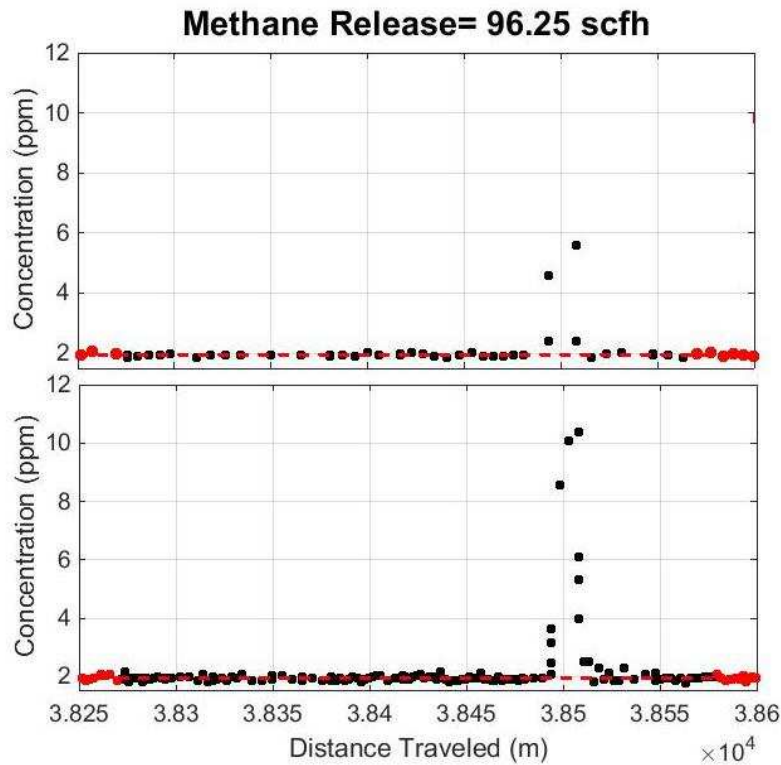


Figure 6.12: Concentration vs distance traveled for 1 Hz (top) and 3 Hz (bottom) for one pass at 96.25 scfh flow rate.

Looking at the spectra used to calculate concentration for 1 Hz, Figure 6.13 shows the data used to calculate the maximum concentration for 1 Hz in Figure 6.12. As was discussed previously, the black data points indicate those kept after the aerosol filter while the red show the ones that were rejected; the cyan curve shows the resultant fit to the data. Although the aerosol filter accurately works to remove influence due to stray particles in the beam path, it also causes

a slight under-reporting when concentration rapidly changes during a measurement period. Since the effect from aerosols is only in the direction towards an increase in absorption, when the filter is applied to data, as shown, the filter rejects scans of the methane peak from higher concentrations, resulting in an overall lower concentration, 5.6 ppmv compared to 10.3 ppmv for 3 Hz. The aerosol filter is necessary to remove influence from dust, which is expected in locations like METEC, so the solution in this case is to sample faster and use the 3 Hz data when possible.

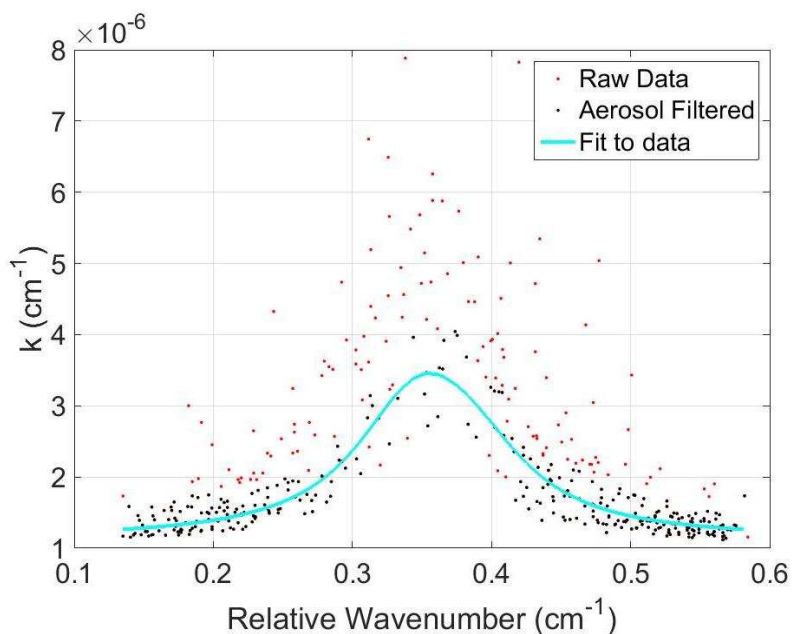


Figure 6.13: Spectra from 1Hz data for maximum concentration in Figure 6.12. Black points indicate those kept by the aerosol filter, red are rejected points. The cyan curve indicates the fit to the data.

Data was taken at METEC on 9/7/17 for much smaller leak rates of 5 and 12 scfh with more favorable wind conditions of 4 mph from the south east. From a total of 120 passes of the leak, only 25 passes were reported as a leak for 1 Hz analysis while 47 were reported for 3 Hz with only 21 overlapping leaks. Integrated plume measurements were lower (<60 ppmv-m) and agreement between 1 Hz and 3 Hz was much worse with a slope = 0.48 and $R^2 = 0.18$. This

worsening in plume detection was possibly partly due to onsite construction at one of the site locations towards the north of the site that coincided with the direction of the plume, and contributed extra dust/noise into our signal. The leak rates, both lower than the smallest measured on 8/30/17 (18 scfh), are potentially on the lower end of what the sensor is capable of measuring. More work at these low flow rates, over a number of days and wind conditions should be performed to identify the lower leak rate limit of detection for the sensor.

Additional data was taken on 9/25/17, with the Picarro (G2203) at 3 flow rates (15, 30 and 65 scfh) from the same location in the southeast corner (Figure 6.8, Figure 6.9). For this test, the single-port Picarro inlet was co-located on the roof with the open-path sensor in the standard mounting that used using in the Atmospheric Science Department. Wind speeds were 2-8 mph and from the south-east/east with temperatures ranging from 9 to 15 C. Data taken during the 15 scfh flow rate had to be discarded as ambient temperatures were very low (< 10 C) during this period and the methane sensor was unable to hold its alignment. A heater system was later designed (Ben Martinez & Simon Gaßner) and implemented into the sensor which improved sensor performance.

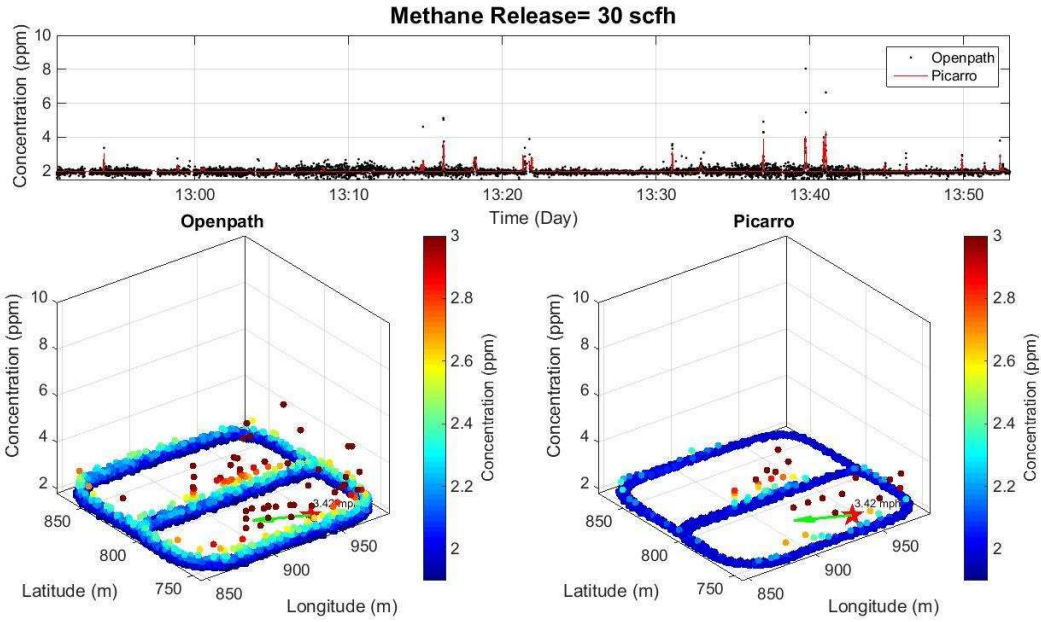


Figure 6.14: Top: Time series of 3Hz and Picarro methane concentration measured for a leak rate of 30 scfh. Bottom: Composite graph of all loops showing the elevated concentration (both color and height indicate methane concentration). Star in the bottom right indicates the location of the leak and the green arrow indicates the average direction and magnitude of local wind. 3 Hz open-path data is shown on the left, Picarro on the right.

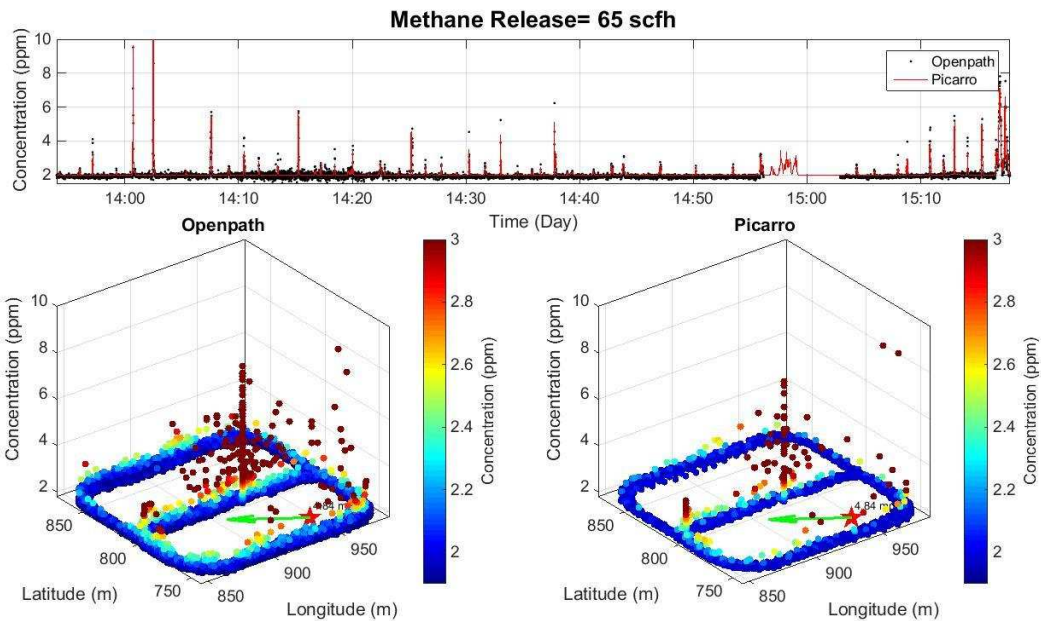


Figure 6.15: Top: Time series of 3Hz and Picarro methane concentration measured for a leak rate of 65 scfh. Bottom: Composite graph of all loops showing the elevated concentration (both color

and height indicate methane concentration. Star in the bottom right indicates the location of the leak and the green arrow indicates the average direction and magnitude of local wind. 3 Hz open-path data is shown on the left, Picarro on the right.

A 1-1 comparison between the Picarro and the open-path data (averaged to the same time scale) shows good agreement with a slope = 0.88 and $R^2 = 0.73$ over 2975 data points (Figure 6.16).

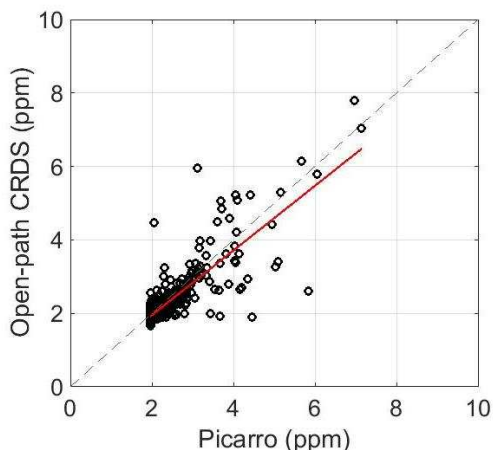


Figure 6.16: 1-1 Comparison of Picarro and open-path for testing at METEC on 9/25/17 with slope = 0.88 and $R^2 = 0.73$.

Integrated plume measurements were calculated for open-path data at 1 and 3 Hz rates and compared to Picarro data using the same methods as discussed previously. Comparison of 1 and 3 Hz integrated rates for these flow rates showed good agreement (Figure 6.17), where 3 Hz again showed slightly higher values 1 Hz. The range in integrated plume measurements was similar for both flow rates, from close to 0 to ~80 ppmv-m, apart from one measurement of 170 ppmv-m for 3 Hz analysis.

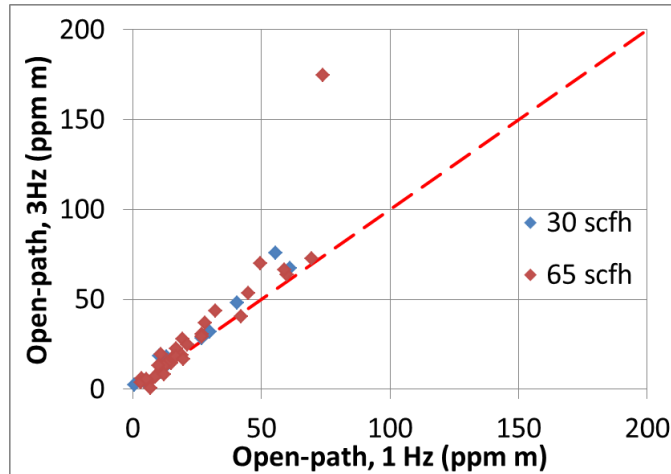


Figure 6.17: Integrated plume measurements for 9/25/17 at METEC for 2 flow rates, comparing open-path 1 Hz and 3 Hz analysis.

Comparison of the open-path and Picarro data (Figure 6.18) showed general good agreement, with larger variation between the two sensors at higher concentration values. It must be noted that the highest 3 Hz value did show agreement with the Picarro along with the next highest 3 measurements.

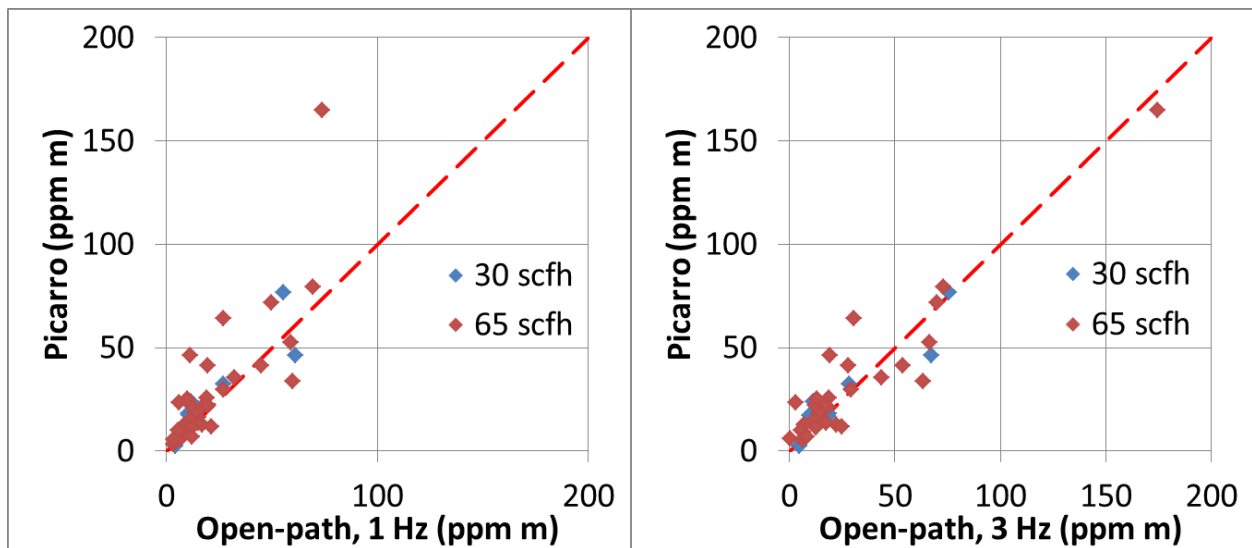


Figure 6.18: Integrated plume measurements for 9/25/17 at METEC for 2 flow rates, comparing open-path and Picarro data.

Looking more closely at the concentration traces for the large 65 scfh peak (Figure 6.19), it is obvious why the 1 Hz integrated plume measurement was so low. As previously discussed,

the 1 Hz analysis can under report concentration when the concentration is changing rapidly over the course of 1 second, for this case 1 Hz shows a largest concentration of ~9 ppmv while ~29 ppmv is reported for 3 Hz and 35 ppmv for the Picarro. Even though the Picarro has a slower sampling rate (~0.83 Hz or 1.2 s) the methods used for determining concentration are able to find the high concentration, leading to high integrated plume measurements. This is further evidence that for the open-path sensor, although sometimes the 1 Hz analysis was able to accurately measure the methane concentration, faster analysis (3 Hz or higher if possible) would be more accurate.

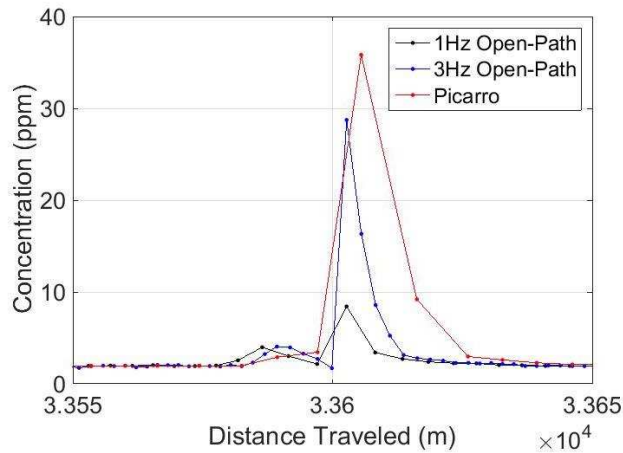


Figure 6.19: Concentration traces for the large pass of the 65 scfh leak release for 1 and 3 Hz open-path data and Picarro.

6.3 Marcellus Basin, PA

The sensor was taken to Marcellus Basin, in southwest PA, 10/27/17-11/2/17 to participate in a field study in co-operation with John Albertson's group from Cornell University. Similar to Platteville, CO, Marcellus Basin (Figure 6.20) has a high density of oil and gas facilities. The area where we focused our study, Washington County located in the south west corner of the state, has 3,986 wells in 861 mi².

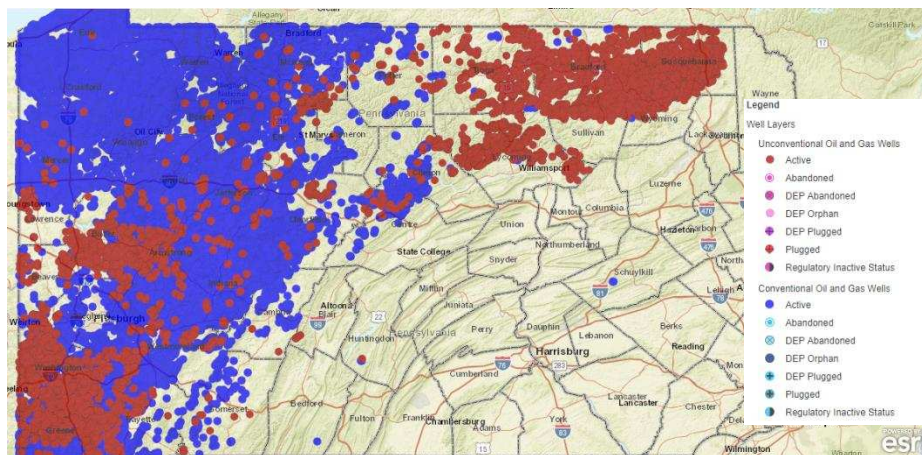


Figure 6.20: Map showing location of oil and gas wells in Pennsylvania, Washington County is located in the south-west corner of the state.

The goal of the Cornell group was to measure VOC emissions downwind of oil and gas facilities, using the open-path CRDS to identify plume locations. A real-time, relatively low cost PID (photo-ionization detection) sensor (Falco (Ion Science Ltd), 11.7 eV lamp) was used to measure total VOC concentrations while SUMMA canister data (standard methods, EPA TO-15) were taken for VOC speciation. Local wind conditions were also measured so that leak rates could be calculated, using the same methods as for the METEC site. A number of sites were pre-selected based on wind conditions and proximity to the road.

The open-path methane sensor was mounted to the roof of the vehicle using Thule racks, with the inlet for the real-time PID sensor was extended to the roof for co-location. The open-path sensor was powered by an inverter plugged into a 12 V battery located in the back of the vehicle. The vehicle was driven slowly past each site, while the methane sensor obtained real-time methane concentrations to locate the plume. Sampling rate for the methane sensor was adjusted in real time between 1 and 3 Hz, depending current conditions. After several passes of the site identified the approximate location and magnitude of the leak, the wind sensor was

installed close to the facility and the SUMMA canister was opened (< 10 s). The site was then driven for an additional > 10 passes.

Over the course of the study, data were collected for 6 days, attempting sampling at 24 locations; sampling was not possible on the other 2 days due to heavy rainfall. Only 2 sites on 10/27/17 were believed to have measureable leaks, while several canister data were taken at several others where it was believed small leaks might have been detected. Sampling proved difficult in this region and time of year due to low wind speeds, dense forests between the facilities and the roads, and large elevation difference between some sites and the roads, as well as inclement weather.

Based on the results of the 9/25/17 METEC testing, and subsequent cold testing in the fall (performed by Ben Martinez), it was determined that the sensor required additional heating to maintain alignment across a wide temperature range. Subsequently a preliminary heating system consisting of 2 high density cartridge heaters inserted into small 30 x 30 cm heat sinks with fans to circulate the air in each cap, and exterior insulation on the caps, front bulkheads and tube, was installed on the sensor prior to PA testing as temperatures near freezing were expected, as well as rain. The heating system was designed to maintain internal temperatures of 25 C. Additional plastic protection was added to the exterior of the sensor insulation to protect from water and rain blockers were added to protect from water ingress at the HR mirror irises (Figure 6.21). These blockers were made from aluminum and attached to the front carbon fiber bulkheads. It was found during testing on 10/29/17-10/30/17, that the rain blocker irises were slightly too small or miss-aligned with the HR irises so that when the sensor was driven down the road, the force of the wind was able to push the blocker enough to block the beam. Based on real-time PID measurements, it was not believed that any leaks were missed during this time.



Figure 6.21: Phase-III sensor mounted on vehicle for study in Marcellus County, PA, October 2017.

Preliminary analysis similar to that shown for data obtained on 8/30/17 at METEC, was performed on the largest leak measured on 10/27/17 (Figure 6.22, Figure 6.23) resulting in estimates of the measured leak. Additionally, SUMMA analysis along with VOC concentrations measured with the PID were used to estimate speciated VOC concentrations and leak rates. This work demonstrated that the methane sensor was adequate for this type of analysis if more time were available for additional measurements with better wind conditions or at more open facilities like those in Colorado.

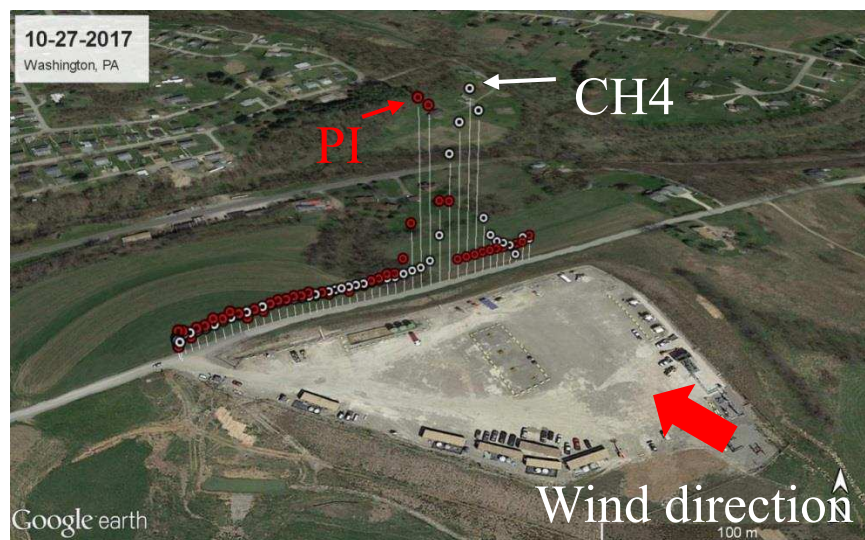


Figure 6.22: Traces of methane (CH₄) gas and VOC (PI) emissions detected using a PID on 10/27/17 in Marcellus County, PA. This work was presented in a poster at AGU in New Orleans, LA 2017 by Dr. Xiaochi Zho

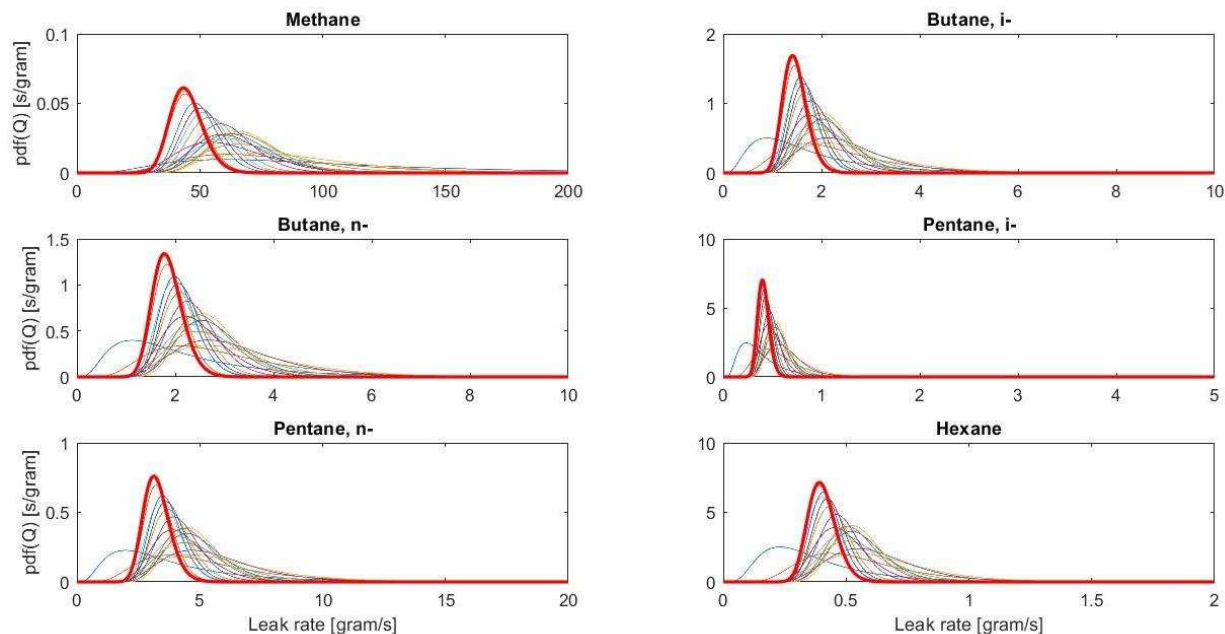


Figure 6.23: Leak rate analysis for data collected on 10/27/17 in Marcellus County, PA. This work was presented in a poster at AGU in New Orleans, LA 2017 by Dr. Xiaochi Zho

In addition to participation in the VOC study, this was a good opportunity to test the sensor for robustness during travel and gain more experience using the sensor in mobile conditions. In addition to measurements of leaks from large oil & gas facilities, we were possibly able to detect methane from a nearby landfill (Figure 6.24), agriculture (Figure 6.25), and what we believed were roadside pipe leaks (Figure 6.26). On 10/30/17 we detected an elevated 4 ppmv methane signal, not close to any oil and gas facilities, but near to the Arden Landfill. Direct wind measurements were not made at this location but local historical met data shows winds were ~15 mph and from the south during this time. Although wind data does not directly show that our measurements were due to the landfill, it is highly likely as no other sources could be seen and local wind measurements could have been slightly different than the hourly average reported for the nearby city.

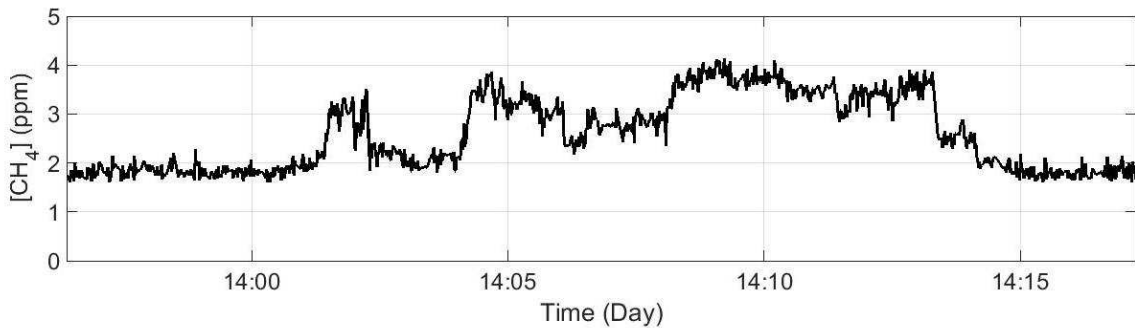
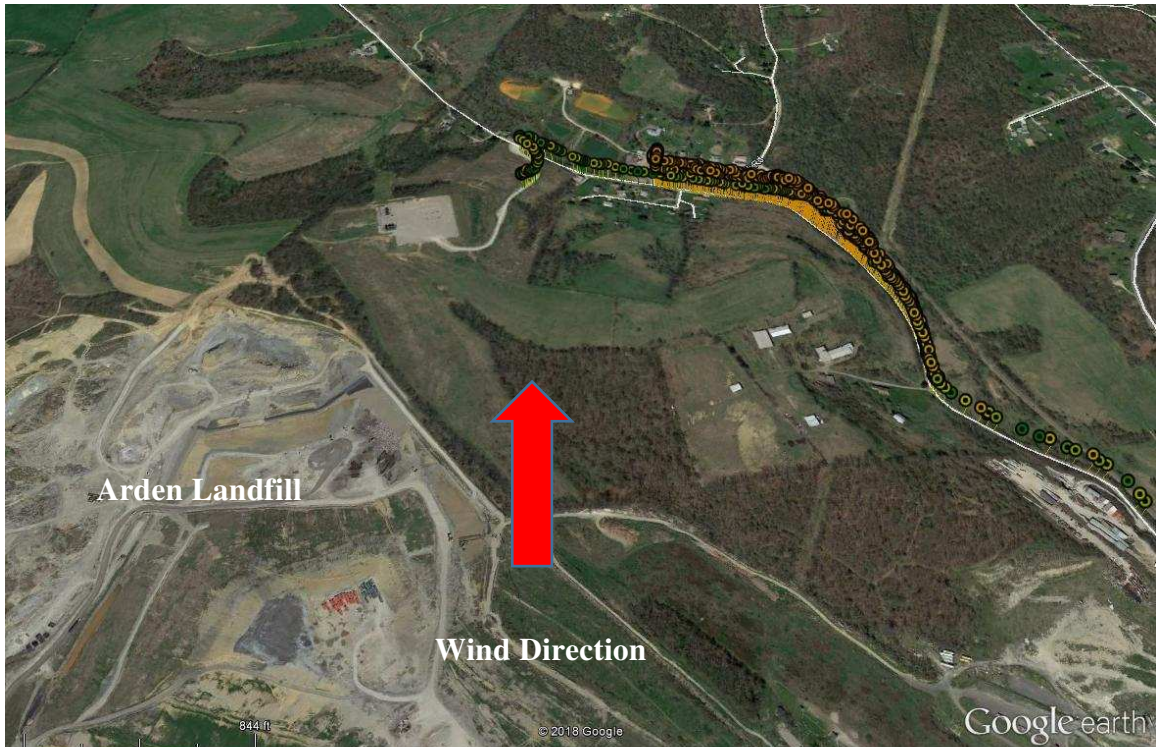


Figure 6.24: (Top) Methane data imposed on Google Earth image, collected on 10/30/17 near Arden Landfill. (Bottom) Time series of methane concentration.

Data collected at a site on 10/31/17 was interesting due to potential contamination from either agriculture or roadside pipes. An oil and gas site was located on top of a large hill next to what appear to be a free range dairy, historical wind data from the nearby city shows winds were ~25 mph from the west (Figure 6.25). Methane measured to the west of the facility showed a persistent 0.5 ppmv increase in methane over background for ~20 passes, but as the vehicle drove up the nearby road to turn around, sharp increases in methane (>5 ppmv) with continued

background increase were observed. Several exposed pipes were seen near some of the larger methane spikes in the adjacent road, but the proximity of the agricultural facility made it difficult to understand the cause of the background increase in the road to the west. Future analysis of the VOC data by the group from Cornell will help determine what the local sources might be.

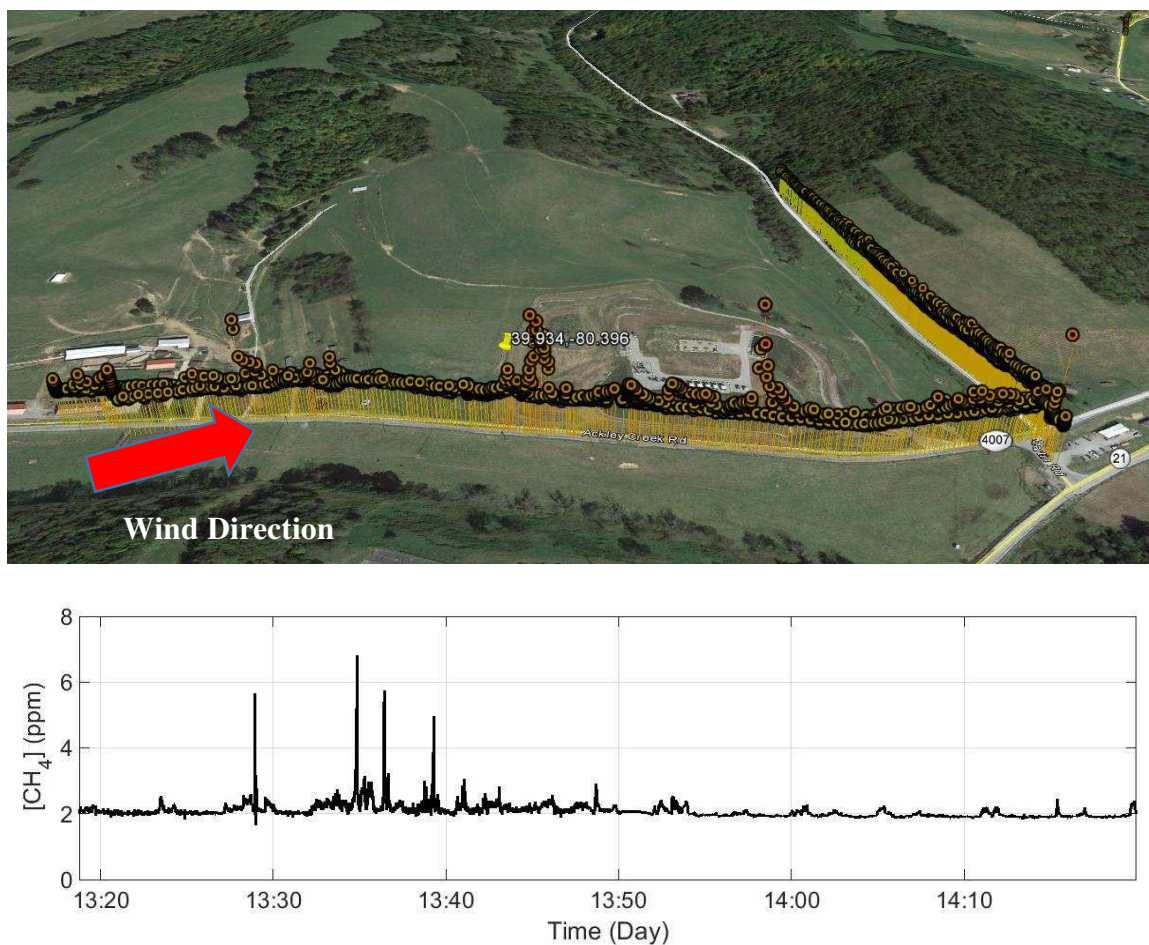


Figure 6.25: (Top) Methane data imposed on Google Earth image, collected on 10/30/17 near an oil and gas site next to what appear to be a dairy. Image was rotated slightly to better visualize the plume. (Bottom) Time series of methane concentration.

There were several instances during this study where spikes in methane were detected, similar to leaks from oil and gas (small in timescale and horizontal distance), but not downwind of a facility. One such site is shown in Figure 6.26 where large methane and VOC signals were detected. Although there was a large facility very close to the road, the methane gas was

consistently measured as we passed or parked next to what appeared to be several vertical pipes at a crossroads upwind of the facility.

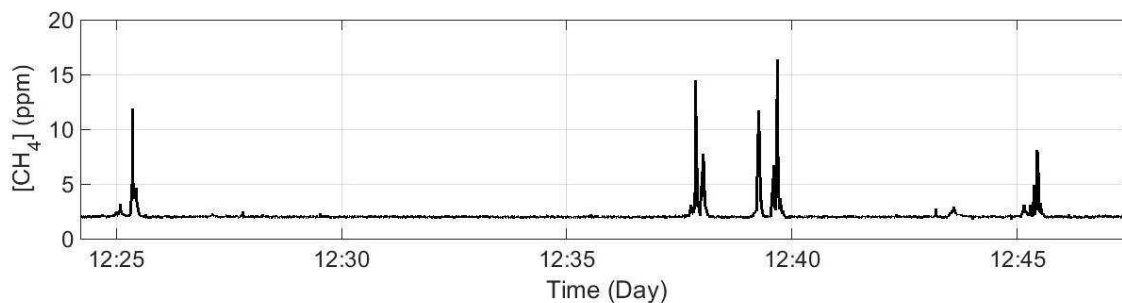


Figure 6.26: (Top) Methane data imposed on Google Earth image, collected on 10/30/17. (Bottom) Time series of methane concentration.

Figure 6.27 shows pictures of two other potential leak locations where only methane but not VOCs were detected. The photo on the left shows what appeared to be a broken pipe on the side of the road where a consistent ~3 ppmv signal was detected. For the case on the right, 6 ppmv methane signal was detected as we were driving between facility sites. The signal was

detected as we passed several times, and a larger signal up to 12 ppmv was measured as we parked next to the valve box and pipes. These results demonstrate that continual monitoring of ambient methane on a vehicle would be able to pick up additional unknown leaks that could be reported to either the homeowners (valve box on the right) or utilities company (pipe on left).



Figure 6.27: (Left): Pipe where potential leak was measured (< 3 ppmv) on 10/29/17. (Right): Valve box or pipes where potential leak (< 12 ppmv) was measured on 10/31/17.

6.4 UAS integration and flight

As discussed in section 4.4, part of the Phase-III hardware development was a reduction in size and weight for integration into a fixed-wing UAS (un-manned aerial system). Although some military or commercial grade medium size UAS's are capable of carrying 100-200 kg payloads, we did not have access to this technology. Instead, the size and weight of the sensor were decreased so the sensor could fit on a smaller UAS or as part of a larger measurement system. The Phase-II total weight (electronics and sensor) of nearly 20 kg was reduced to < 4 kg for Phase-III for the optical sensor, electronics and auxiliary cables, which was capable of integrating into a UAS. During the UAS flights, the additional heating system and insulation would need to be removed as their combined weight, and additional power requirements were too much for the UAS to carry. To account for temperature effects on sensor alignment, the sensor would need to be re-aligned at the temperature the sensor would fly and it was assumed

that over the short duration of the flights, and the limited height the aircraft would fly that additional effects of temperature on alignment would be small.

The methane sensor was integrated along with a WMS-based ammonia sensor onto a 12-foot wingspan Telemaster, a fixed-wing UAV available online for hobby plane enthusiasts and within the capabilities of CSU to construct and operate without outside assistance. The standard configuration of the plane comes with a dropbox capable of carrying up to 7 lbs (3.1 kg) of candy but the motor, propellers and landing gear were optimized by a team (Charles Rose, Meghan Reimann, Jared Ham, Collin VanTilburg, Dr. Fred Smith) at CSU to increase the carrying capacity of the plane to 7.9 kg. The Telemaster utilizes a Power 360 Brushless Outrunner Motor, 180Kv, designed for hobby airplanes weighing 6.8-11 kg and is controlled by Castle Creations Phoenix Edge HV 160 A, 50V Brushless Electronic Speed Controller. A tricycle landing gear with additional wingtip skids was installed to prevent the plane from tipping to the sides and damaging the sensors. The WMS-based ammonia sensor was developed by another PhD student in the group (Soran Shadman) for detection of ammonia gas using a QCL at 10.3 μm . The construction of the optical sensor was designed similarly to the Phase-III methane sensor out of carbon fiber to reduce the weight and increase the structural integrity of the sensor and the electronics enclosure was nearly identical to the methane. The total weight of the ammonia sensor was 3.6 kg for a total sensor payload weight for the two sensors of 7.84 kg. The weight of the aircraft was 15.69 kg for a total UAS weight of 23.53 kg.

The sensors are mounted using simple conduit hangers, underneath each wing, ~2 ft from the air craft body (Figure 6.28). Sensor positions were determined through use of simulated payloads to minimize the drag, balance center of gravity and improve chances of aircraft flight. The sensor electronics and battery were mounted inside the body of the plane with cabling strung

along the wings to the sensor. The upper altitude and distance limits are restricted by FFA regulation to stay within line of sight of plane operator. The maximum possible flight duration was 10 min, limited by the batteries (and total weight). For our flights, the plane was operated by CSU Emeritus Professor Dr. Fred Smith.

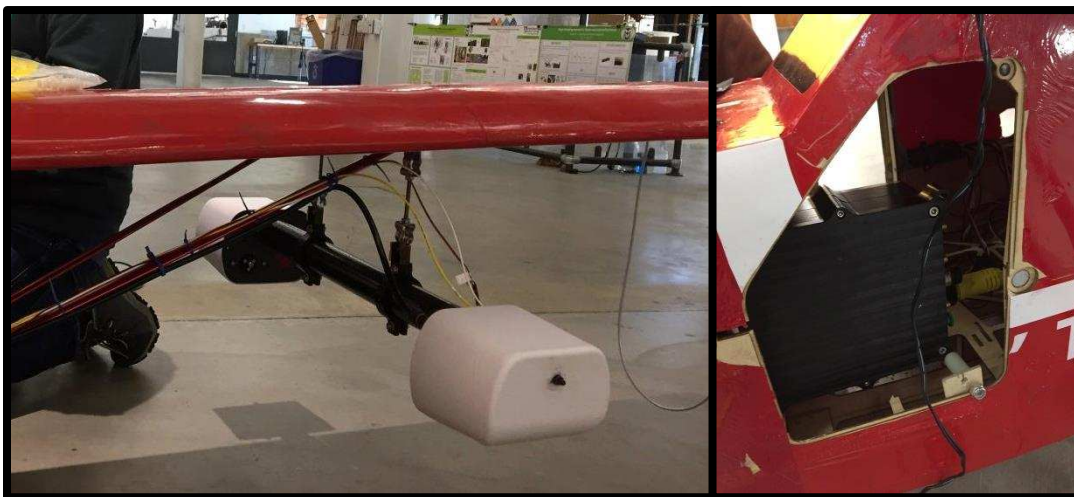


Figure 6.28: (Left) Methane sensor mounted onto 12 ft Telemaster. (Right) Sensor electronics mounted in body of plane.

For the purpose of this sensor assembly, measurements of methane and ammonia were combined to determine ammonia flux⁶⁷ downwind of confined animal operations (CAFO's) but the methane sensor could similarly be combined with an ethane or VOC sensor to identify leaks from oil and gas facilities. The aircraft has been flown multiple times with simulated sensors to ensure the plane can safely fly, but no measurements with the actual sensors have been performed yet as the final weight was slightly higher than expected and additional safety flights have been necessary.

CHAPTER 7:

Conclusions

The objective of this work was to demonstrate the capabilities of an open-path CRDS-based sensor for measurement of methane from oil and gas applications in a small, mobile package. The theory behind CRDS was discussed in Chapter 3, along with the advantages and disadvantages faced by modification to open-path configuration as is used in this work. Descriptions of the sensor construction, along with improvements made through the 3 phases of construction were discussed in Chapter 4. Results from precision and accuracy tests, (Chapter 5) and mobile measurements from several field studies in Colorado and Pennsylvania (Chapter 6) will be discussed below. Finally, recommendations for additional sensor testing/applications and areas for sensor performance improvement are discussed at the end of this chapter.

7.1 Summary

Adaptation of the sensor from closed-path to open-path and sampling in ambient pressure increases the spectral region necessary for measurement, but allows a simplification of the spectra fit to a simple Lorentzian rather than the more complex Voigt profile as discussed in Chapter 3. Thus, although the high-pressure spectral peaks made finding a ‘baseline’ signal either impossible or very difficult, the synthetic spectrum (sum of Lorentzians) allows the baseline to be a fit parameter and is not necessary to know beforehand when calculating concentration. The synthetic spectrum was shown to work well in cases where there was significant interference from other peaks (1742 nm) as well as a more ideal case where only methane needed to be considered (1651 nm). Temperature and pressure need to be understood for proper calculation of concentration but can be measured in real-time with co-located sensors.

Chapter 4 gives detailed information and descriptions about each component (optics, electronics, hardware) used in the sensor. Throughout the three phases of the sensor, we were able to show great reductions in both size and weight, moving from a large laboratory type sensor (2' x 3' x 3') utilizing individual electronic components, desktop computer, and weighing several hundred pounds, that needed considerable power source to run and had to be lifted by forklift into a pickup truck to two small packages, 7" x 6" x 33" (2 kg), and 5.5" x 3" x 11.5" (1.4 kg) that can be run from a 12V, 25W battery and easily be mounted by one person on either a vehicle or a small UAS. The improvements in size and weight came through optimization of the optics used, such as the focal length of the first lens and moving from 1" optics to ½" optics which allowed the height of the sensor to shrink along with the weight. Significant weight reductions and ease of alignment were made for the optical sensor simply by designing a custom mount for the optics and by using carbon fiber as the material, the weight could be significantly reduced while maintaining structural integrity and reducing effects on sensitive alignment due to thermal expansion.

Moving from laboratory bench-top electronic components and computer system to a custom designed sbRIO DAQ system with integrated laser control and power distribution system were the areas for the largest reduction in power draw and weight. Bench-top electronics typically are the easiest to use and allow adaptation for multiple applications, both useful in a lab development setting, but often much of the size and power draw are due to functions not necessary in a specialized sensor. Using OEM style components requires more expertise to use and integrate but are typically designed for specific tasks without extra, unnecessary weight. Similarly, a desktop-based DAQ system is the easiest for an amateur lab control system but significant improvements in sensor speed, analysis could be gained when the un-necessary 'ease

of design' components are removed from the computer (i.e. Windows-based systems). Both the design of the optical mount and custom electronics would not have been possible without contracted, professional assistance.

Some optical improvements were made for the sensor as well, moving from a free-space AOM to a fiber-coupled design which decreased alignment complexity and translates into increased ruggedness of the alignment of the sensor. The most significant improvement came from optimizing the laser wavelength from 1742 nm, which suffered from significant interference from water, to 1651 nm, which had no interference from other gaseous species and was ~30x stronger. This shift in wavelength, and increase in line strength, increased the sensitivity of the sensor and decreased what complexities did exist due to other local interferences. Many of the other components, detector, AOM driver, and laser controllers, were also changed from Phase-I to Phase-III. Several of these were simply changes from bench-top to OEM devices (laser controller, AOM driver) but the detector was exchanged for one that was optimum for the new laser wavelength.

Chapter 5 demonstrated the preliminary testing done for the prototype open-path sensor (Phase-I). The mirror purge system demonstrated that it could adequately maintain reflectivity of the cavity mirrors when exposed to high aerosol loading (smoking candle) or through 100's of hours of outdoor use. In addition to potential mirror contamination, aerosols were found to cause significant noise in the spectra signal for line strengths similar to ours. The aerosol signal presents as a higher absorption 'tail' on the Gaussian envelope typically due to sensor uncertainty. A numerical filter approach was developed which was able to remove the signal due to aerosols, while preserving the spectral shape and sensor sensitivity. Some situations, such as exhaust from other vehicles while idling, cannot be removed by the filter, but this will be a small

portion of mobile sampling. The accuracy of the high-pressure Lorentzian synthetic spectrum was tested by measuring known methane concentrations delivered to the sensor in a closed-path configuration. CRDS is an optically calibration-free technique, so this check identified whether the high-pressure assumption and fit were suitable. For concentrations, 0-20 ppmv, the sensor, and synthetic spectrum, demonstrated that agreement within experimental uncertainty.

Sensitivity tests were performed, following typical Allan Variance techniques, on each iteration of the sensor as various components were changed and added to ensure sensitivity was maintained. Initial open-path studies (Phase-I) demonstrated that noise from aerosols degraded the sensitivity by up to 30x, use of the aerosol filter was able to increase sensitivity to within ~3 of zero air values, for a sensitivity of ~50 ppbv in 1 s. Studies for Phase-II sensor demonstrated a relationship between concentration and sensitivity, demonstrating ~12 ppbv in 1 s for background values of 1.8 ppmv, but 30 ppbv in 1 s for our open-path lab measurements where concentration was slightly elevated (2.5ppmv). Improvements to the sensor optics, showed an increase in sensitivity for Phase-III with results <10 ppbv in 1 s.

A comparison study between the Phase-I prototype sensor and a commercial available CRDS methane sensor (Picarro, G2203) in an indoor environment demonstrated that the open-path sensor was capable of measuring variable methane plumes, and demonstrated a more stable measurement than the closed-path sensor due to the open-path average.

Multiple studies of controlled releases and of leaks from oil & gas facilities demonstrated that the methane sensor was able to work as a mobile, outdoor sensor. Preliminary comparison between the Phase-II open-path sensor and the Picarro demonstrated that the open-path sensor could identify small (~3 ppmv) and large (~15 ppmv) plumes due to methane leaks. Ideas for filtering 'bad' open-path data (due to exhaust, etc) were developed and showed good agreement

(slope > 0.8, $R^2 > 0.8$) between the open-path and Picarro sensors over several hours of continuous measurement.

Measurement of methane plumes from controlled leaks at a simulated O&G site demonstrated that the sensor could be used to quantify leaks from 18-121 scfh, where the analysis was provided by a collaborator. Integrated plume measurements demonstrated that the aerosol filter can underestimate actual methane concentrations for high or rapidly changing concentrations, and higher rate of analysis (3 Hz compared to 1 Hz) provides more accurate estimates. This was confirmed by comparison of the open-path and Picarro sensors where faster analysis of the open-path sensor demonstrated better agreement for high concentrations.

Mobile measurements taken in the Marcellus basin in PA, demonstrated that the open-path sensor, along with local wind measurements, could be used to quantify leaks from nearby facilities. The study also demonstrated the ability of the open-path sensor to detect leaks due to agriculture sources, waste-treatment facilities and potentially roadside pipes. The sensor also demonstrated its ability to maintain alignment for aircraft travel, inclement weather (rain), and continuous use. Testing of the sensor in cold weather demonstrated that large shifts in temperature still affect sensor alignment and continuing work is being done on this front.

Finally, the small size and weight of the sensor were shown capable of mounting into a small UAS, along with an ammonia sensor of similar size, for mobile airborne measurements.

7.2 Future Work

7.2.1 Methane Field Studies

The results discussed in this work showed that for measurements taken on 8/30/17 we were able to reliably measure leaks of 18 scfh, while results from 9/7/17 showed almost no measurements for 5 and 12 scfh. Extended controlled release studies at METEC could be performed, especially at lower flow rates to probe the lower limits of leak detection possible with the sensor. It would be interesting to do more of these low flow rates at a range of wind conditions to identify whether the sensor is capable of picking up low signals.

The Phase-III sensor demonstrated in PA that it is capable of measuring leaks from real oil and gas facilities, although some sites proved difficult to measure, and it would be interesting to attempt more measurements of oil and gas facilities. Measurements could be made in Platteville, CO, where oil and gas facilities are plentiful and located close to nearby roads. As with the controlled release studies, measurements of this kind need to be performed for a range of wind conditions. It would also be interesting to measure a leak at a range of distances away from the source to probe how well the sensor can measure close vs far away from the source.

It would of course be interesting to participate in further collaborative studies like the one in PA where other trace gasses could be measured (VOC's, ethane) to determine the source of the gas and separate agriculture, waste facilities and oil and gas. Further work with the Cornell group to understand the limits of leak rate quantification could be performed.

Finally, it was demonstrated that the sensor was capable of integrating into an un-manned aerial system (UAS), although we did not have any opportunities to fly the sensor yet. Flights with the current system should be performed to understand how well the sensor works in an aerial environment and whether there are any additional issues (wind flow, temperature, EMI

from the plane), which need to be accounted for. Initial flight tests should be performed at METEC for controlled releases to understand what the most effective flight patterns would be for leak rate estimation. After the preliminary tests are completed, the UAS should be flown downwind of actual oil and gas facilities to look for and quantify actual leaks. Measurements from real facilities will likely require much more coordination from the FAA and from cooperating natural gas companies.

7.2.2 Environmental Studies

Work is currently being performed in the lab by another student (Ben Martinez) to ensure that the sensor can operate for a range of temperatures (-30 C to 30 C) using a custom heating and insulation system. The same issues that cause the sensor alignment to deteriorate due to cold temperature will also cause poor alignment at high temperatures. A cooling system will need to be designed to expand the temperature range for summer use when warmer ambient temperatures and high sun intensity will cause the sensor to heat past 30 C.

Preliminary drives with the sensor demonstrate that it can operate for a range of vehicle speeds and ambient winds. It would be an interesting study to look in a more rigorous fashion the effect of wind direction on the sensor while stationary or moving, and look at the effects of the wind direction relative to the movement of travel. Variations in index of refraction of air in the open-path cavity (due to changes in temperature or pressure, from the wind currents) could cause steering of the carefully aligned cavity beam which could cause the sensor to miss-align. If significant beam steering were discovered for certain wind orientations, work could be done on the physical structure (the caps and the tube) to design a more aerodynamic sensor.

The full scale range of the sensor should be investigated through use of a closed-path cell to investigate the maximum concentration that the sensor can detect. When the current sensor is

working at optimum performance, a methane concentration of 24 ppmv leads to a minimum τ of 3 μ s at the spectral peak. With a DAQ sampling speed limited to 1 MS/s, at higher concentrations it becomes increasingly difficult to measure the peak of the sample. Theoretically, as long as there are sufficient measurements of the sides (wings) of the peak, the concentration can still be determined. This was the case for many of the high concentration values measured in the Marcellus, PA study. Although simulations show concentrations can be accurately fit for $[\text{CH}_4] > 100$ ppmv, additional measurement uncertainty might make it more difficult. By using a sample cell with known concentrations of gas, as done with Phase-I, the upper range of concentrations measurable by the sensor, and their errors, could be determined.

7.2.3 Sensor Improvements

Improvements to the DAQ system of the sensor could increase the temporal (and by proxy the spatial) resolution of the sensor. As previously discussed, the maximum sampling rate of the sensor is 1 MS/s, limited by the ADC card used for the detector input. At this time, no better alternatives exist, but if they become possible, they should be used with the sensor to increase the sampling rate of the sensor and increase the measurement range of the sensor. Additionally, at this time, the number of ringdowns per second that can be measured, and by proxy, the rate of concentration, is limited by the capabilities of the sbRIO. At the current rate of 3 Hz measurement, for vehicle speeds of 10-50 mph, this leads to a spatial resolution of 1.3-6.7 m. Some of the small leaks that were measured in this work constituted just a few seconds worth of data, faster sampling rate would improve the resolution or even capture small ones that weren't detected. As was demonstrated in analysis of controlled releases at METEC, the methods used to filter for aerosol particles can cause an underestimation of the total methane

concentration measured, and faster (3 Hz) sampling improved measurement. Further increases in sensor sampling speed would decrease the effect this underestimation has on measurement.

Although, increasing the reflectivity of the HR mirrors can improve the sensitivity of the sensor, I would not recommend doing so until improvements to the DAQ system have been implemented. Increasing the reflectivity of the sensor would cause the baseline ring-down time of the empty cavity to increase, increasing the amount of data that is necessary to acquire to accurately measure a ring-down, which is currently one of the issues causing the DAQ to slow down. Increasing the reflectivity of the mirrors decreases the power reaching the detector at the cavity output, potentially negatively influencing the sensor depending on the magnitude of the power decrease. The detector used for this work has at times been oversaturated, and would not suffer for a slight loss in power.

Finally, more precise work should be done to investigate which components in the optical setup are most affected by temperature to see if a more rugged, non-temperature controlled version of the sensor is possible or if one of the off-the shelf optical mounts is causing the issue. It will only take small, micron-size, changes to cause the sensor to come out of alignment, which will take very precise measurement techniques to determine.

BIBLIOGRAPHY

1. Fiore, A. M. *et al.* Multimodel estimates of intercontinental source-receptor relationships for ozone pollution. **114**, 1–21 (2009).
2. IPCC. *Climate Change 2014: Synthesis Report. Contribution of Working Groups I, II and III to the Fifth Assessment Report of the Intergovernmental Panel on Climate Change. Core Writing Team, R.K. Pachauri and L.A. Meyer* (2014). doi:10.1017/CBO9781107415324.004
3. France, P. C., Willem, J., Friedlingstein, P. & Munhoven, G. Carbon and Other Biogeochemical Cycles 6. (2013).
4. U.S. Environmental Protection Agency. *Inventory of U . S . Greenhouse Gas Emissions and Sinks : 1990 – 1998. Ipc* (2016). doi:EPA 430-R-13-001
5. Zimmerle, D. J. *et al.* Methane Emissions from the Natural Gas Transmission and Storage System in the United States. *Environ. Sci. Technol.* 150721080033007 (2015). doi:10.1021/acs.est.5b01669
6. Pétron, G. *et al.* Hydrocarbon emissions characterization in the Colorado Front Range: A pilot study. *J. Geophys. Res. Atmos.* **117**, (2012).
7. Smith, M. L. *et al.* Airborne Ethane Observations in the Barnett Shale: Quantification of Ethane Flux and Attribution of Methane Emissions. *Environ. Sci. Technol.* **49**, 8158–8166 (2015).
8. Karion, A. *et al.* Aircraft-Based Estimate of Total Methane Emissions from the Barnett Shale Region. *Environ. Sci. Technol.* **49**, 8124–8131 (2015).
9. Allen, D. T. *et al.* Measurements of methane emissions at natural gas productions sites in

- the United States. *Proc. Natl. Acad. Sci. U. S. A.* **110**, 17768–17773 (2013).
10. Yacovitch, T. Ground-Based Measurements of Ethane to Methane Ratios in the Barnett Shale Methane and Ethane. (2013).
 11. Gómez, C. & Green, D. R. Small unmanned airborne systems to support oil and gas pipeline monitoring and mapping. *Arab. J. Geosci.* **10**, (2017).
 12. Rella, C. W. *et al.* High accuracy measurements of dry mole fractions of carbon dioxide and methane in humid air. *Atmos. Meas. Tech.* **6**, 837–860 (2013).
 13. Crosson, E. R. A cavity ring-down analyzer for measuring atmospheric levels of methane, carbon dioxide, and water vapor. *Appl. Phys. B Lasers Opt.* **92**, 403–408 (2008).
 14. Eapi, G. R., Sabnis, M. S. & Sattler, M. L. Mobile measurement of methane and hydrogen sulfide at natural gas production site fence lines in the Texas Barnett Shale. *J Air Waste Manag Assoc* **64**, 927–944 (2014).
 15. Rella, C. W., Tsai, T. R., Botkin, C. G., Crosson, E. R. & Steele, D. Measuring emissions from oil and natural gas well pads using the mobile flux plane technique. *Environ. Sci. Technol.* **49**, 4742–8 (2015).
 16. Huang, H. & Lehmann, K. K. Noise in cavity ring-down spectroscopy caused by transverse mode coupling. *Opt. Express* **15**, 8745–8759 (2007).
 17. Huang, H. & Lehmann, K. K. Long-term stability in continuous wave cavity ringdown spectroscopy experiments. *Appl. Opt.* **49**, 1378–1387 (2010).
 18. Huang, H. & Lehmann, K. K. Effects of linear birefringence and polarization-dependent loss of supermirrors in cavity ring-down spectroscopy. *Appl. Opt.* **47**, 3817–3827 (2008).
 19. Fawcett, B. L., Parkes, a. M., Shallcross, D. E. & Orr-Ewing, a. J. Trace detection of

- methane using continuous wave cavity ring-down spectroscopy at 1.65 μm . *Phys. Chem. Chem. Phys.* **4**, 5960–5965 (2002).
20. Orr, B. J. & He, Y. Rapidly swept continuous-wave cavity-ringdown spectroscopy. *Chem. Phys. Lett.* **512**, 1–20 (2011).
 21. Yan, W. B., Chen, Y., Chen, H., Krusen, C. & Woods, P. T. Development and applications of continuous-wave cavity ring-down spectroscopy. *Int. J. Thermophys.* **29**, 1567–1577 (2008).
 22. Yver Kwok, C. E. *et al.* Methane emission estimates using chamber and tracer release experiments for a municipal waste water treatment plant. *Atmos. Meas. Tech.* **8**, 2853–2867 (2015).
 23. Collett, J. L., Ham, J. & Hecobian, A. North Front Range Oil and Gas Air Pollutant Emission and Dispersion Study. (2016).
 24. Lamb, B. K. *et al.* Development of Atmospheric Tracer Methods to Measure Methane Emissions from Natural Gas Facilities and Urban Areas. *Science (80-.)*. **29**, 1995–1995 (1995).
 25. Harriss, R. *et al.* Using Multi-Scale Measurements to Improve Methane Emission Estimates from Oil and Gas Operations in the Barnett Shale Region, Texas. *Environ. Sci. Technol.* **49**, 7524–7526 (2015).
 26. Brantley, H. L., Thoma, E. D., Squier, W. C., Guven, B. B. & Lyon, D. Assessment of Methane Emissions from Oil and Gas Production Pads using Mobile Measurements. *Environ. Sci. Technol.* **48**, 14508–15 (2014).
 27. Olivero, J. J. & Longbothum, R. L. Empirical fits to the Voigt line width: A brief review.

- J. Quant. Spectrosc. Radiat. Transf.* **17**, 233–236 (1977).
28. Whiting, E. E. An empirical approximation to the Voigt profile. **8**, 1379–1384 (1968).
 29. Brown, L. R. *et al.* Methane line parameters in the HITRAN2012 database. *J. Quant. Spectrosc. Radiat. Transf.* **130**, 201–219 (2013).
 30. Tütüncü, E., Nägele, M., Fuchs, P., Fischer, M. & Mizaikoff, B. IHWG-ICL: Methane Sensing with Substrate-Integrated Hollow Waveguides Directly Coupled to Interband Cascade Lasers. *ACS Sensors* **1**, 847–851 (2016).
 31. Ono, S. *et al.* Measurement of a doubly substituted methane isotopologue, $^{13}\text{CH}_3\text{D}$, by tunable infrared laser direct absorption spectroscopy. *Anal. Chem.* **86**, 6487–6494 (2014).
 32. Schneising, O. *et al.* Three years of greenhouse gas column-averaged dry air mole fractions retrieved from satellite – Part 2: Methane. *Atmos. Chem. Phys. Discuss.* **8**, 8273–8326 (2008).
 33. Thorpe, A. K., Frankenberg, C. & Roberts, D. A. Retrieval techniques for airborne imaging of methane concentrations using high spatial and moderate spectral resolution: Application to AVIRIS. *Atmos. Meas. Tech.* **7**, 491–506 (2014).
 34. Herriott, D. R. & Schulte, H. J. Folded Optical Delay Lines. *Appl. Opt.* **4**, 883 (1965).
 35. Webster, C. R. Measuring methane and its isotopes $^{12}\text{CH}_4$, $^{13}\text{CH}_4$, and CH_3D on the surface of Mars with in situ laser spectroscopy. *Appl. Opt.* **44**, 1226–1235 (2005).
 36. Mahaffy, P. R. *et al.* The sample analysis at mars investigation and instrument suite. *Space Sci. Rev.* **170**, 401–478 (2012).
 37. Barry, H. R., Corner, L., Hancock, G., Peverall, R. & Ritchie, G. A. D. Cavity-enhanced absorption spectroscopy of methane at $1.73\ \mu\text{m}$. *Chem. Phys. Lett.* **333**, 285–289 (2001).

38. Baer, D. S., Paul, J. B., Gupta, M. & O'Keefe, A. Sensitive absorption measurements in the near-infrared region using off-axis integrated-cavity-output spectroscopy. *Appl. Phys. B Lasers Opt.* **75**, 261–265 (2002).
39. Paul, J. B., Lapson, L. & Anderson, J. G. Ultrasensitive absorption spectroscopy with a high-finesse optical cavity and off-axis alignment. *Appl. Opt.* **40**, 4904–4910 (2001).
40. Romanini, D., Kachanov, A. a. & Stoeckel, F. Diode laser cavity ring down spectroscopy. *Chem. Phys. Lett.* **270**, 538–545 (1997).
41. Nara, H. *et al.* Effect of air composition (N₂, O₂, Ar, and H₂O) on CO₂ and CH₄ measurement by wavelength-scanned cavity ring-down spectroscopy: Calibration and measurement strategy. *Atmos. Meas. Tech.* **5**, 2689–2701 (2012).
42. Wada, R., Beames, J. M. & Orr-Ewing, A. J. Measurement of IO radical concentrations in the marine boundary layer using a cavity ring-down spectrometer. *J. Atmos. Chem.* **58**, 69–87 (2007).
43. Fuchs, H. *et al.* A sensitive and versatile detector for atmospheric NO₂ and NO_x based on blue diode laser cavity ring-down spectroscopy. *Environ. Sci. Technol.* **43**, 7831–7836 (2009).
44. O'Keefe, A. & Deacon, D. a. G. Cavity ring-down optical spectrometer for absorption measurements using pulsed laser sources. *Rev. Sci. Instrum.* **59**, 2544 (1988).
45. Dudek, J. B. *et al.* Trace moisture detection using continuous-wave cavity ring-down spectroscopy. *Anal. Chem.* **75**, 4599–4605 (2003).
46. Hagen, C. L. *et al.* Cavity ring-down spectroscopy sensor for detection of hydrogen chloride. *Atmos. Meas. Tech.* **7**, 345–357 (2014).

47. Scherer, J. J., Paul, J. B., O'Keefe, A. & Saykally, R. J. Cavity Ringdown Laser Absorption Spectroscopy: History, Development, and Application to Pulsed Molecular Beams. *Chem. Rev.* **97**, 25–51 (1997).
48. Aziz, M. S. I. & Orr-Ewing, A. J. Development and application of an optical sensor for ethene in ambient air using near infra-red cavity ring down spectroscopy and sample preconcentration. *J. Environ. Monit.* **14**, 3094–100 (2012).
49. Baynard, T. *et al.* Design and Application of a Pulsed Cavity Ring-Down Aerosol Extinction Spectrometer for Field Measurements. *Aerosol Sci. Technol.* **41**, 447–462 (2007).
50. Butler, T. J. a, Miller, J. L. & Orr-Ewing, A. J. Cavity ring-down spectroscopy measurements of single aerosol particle extinction. I. the effect of position of a particle within the laser beam on extinction. *J. Chem. Phys.* **126**, 174302 (2007).
51. Mack, L. a. *et al.* Optical closure experiments for biomass smoke aerosols. *Atmos. Chem. Phys.* **10**, 9017–9026 (2010).
52. Morville, J., Romanini, D., Kachanov, a. a. & Chenevier, M. Two schemes for trace detection using cavity ringdown spectroscopy. *Appl. Phys. B Lasers Opt.* **78**, 465–476 (2004).
53. Smith, J. D. & Atkinson, D. B. A portable pulsed cavity ring-down transmissometer for measurement of the optical extinction of the atmospheric aerosol. *Analyst* **126**, 1216–1220 (2001).
54. Picarro. CRDS Analyzer for Fast CO₂, CH₄, H₂O in Air – Model G2301-f. *Measurement* 4–5 (2010).

55. Roberts, J. M. *et al.* Measurement of HONO, HNCO, and other inorganic acids by negative-ion proton-transfer chemical-ionization mass spectrometry (NI-PT-CIMS): Application to biomass burning emissions. *Atmos. Meas. Tech.* **3**, 981–990 (2010).
56. He, Y. *et al.* Remote open-path cavity-ringdown spectroscopic sensing of trace gases in air, based on distributed passive sensors linked by km-long optical fibers. *Opt. Express* **22**, 13170 (2014).
57. Bitter, M., Ball, S. M., Povey, I. M. & Jones, R. L. A broadband cavity ringdown Spectrometer for in-situ measurements of atmospheric trace gases. *Atmos. Chem. Phys. Discuss.* **5**, 2547–2560 (2007).
58. Gordon, T. D. *et al.* Design of a Novel Open-Path Aerosol Extinction Cavity Ringdown Spectrometer. *Aerosol Sci. Technol.* **49**, 00–00 (2015).
59. Schocker, A., Kohse-Höinghaus, K. & Brockhinke, A. Quantitative determination of combustion intermediates with cavity ring-down spectroscopy: systematic study in propene flames near the soot-formation limit. *Appl. Opt.* **44**, 6660–6672 (2005).
60. Scherer, J. J., Aniolek, K. W., Cernansky, N. P. & Rakestraw, D. J. Determination of methyl radical concentrations in a methane air flame by infrared cavity ringdown laser absorption spectroscopy. *J. Chem. Phys.* **107**, 6196–6203 (1997).
61. Yalin, A. P., Laux, C. O., Kruger, C. H. & Zare, R. N. Spatial profiles of N₂⁺ concentration in an atmospheric pressure nitrogen glow discharge. *Plasma Sources Sci. Technol.* **11**, 248–253 (2002).
62. Rothman, L. S. *et al.* The HITRAN2012 molecular spectroscopic database. *J. Quant. Spectrosc. Radiat. Transf.* **130**, 4–50 (2013).

63. Morville, J., Romanini, D., Chenevier, M. & Kachanov, A. Effects of laser phase noise on the injection of a high-finesse cavity. *Appl. Opt.* **41**, 6980–6990 (2002).
64. Pettersson, A., Lovejoy, E. R., Brock, C. a., Brown, S. S. & Ravishankara, a. R. Measurement of aerosol optical extinction at 532nm with pulsed cavity ring down spectroscopy. *J. Aerosol Sci.* **35**, 995–1011 (2004).
65. Miller, J. L. & Orr-Ewing, A. J. Cavity ring-down spectroscopy measurement of single aerosol particle extinction. II. Extinction of light by an aerosol particle in an optical cavity excited by a cw laser. *J. Chem. Phys.* **126**, 174303 (2007).
66. Berden, G. & Engeln, R. *Cavity Ring-Down Spectroscopy: Techniques and Applications*. (Blackwell Publishing, 2009).
67. Sun, K. *et al.* Open-path eddy covariance measurements of ammonia fluxes from a beef cattle feedlot. *Agric. For. Meteorol.* **213**, 193–202 (2015).
68. Prenni, A. J. *et al.* Oil and gas impacts on air quality in federal lands in the Bakken region: An overview of the Bakken Air Quality Study and first results. *Atmos. Chem. Phys.* **16**, 1401–1416 (2016).
69. Albertson, J. D. *et al.* A Mobile Sensing Approach for Regional Surveillance of Fugitive Methane Emissions in Oil and Gas Production. *Environ. Sci. Technol.* **50**, 2487–2497 (2016).